

KfK 3792
Februar 1985

Pionabsorption in Flight on ^3He

S. H. Ljungfelt
Institut für Kernphysik

Kernforschungszentrum Karlsruhe

KERNFORSCHUNGSZENTRUM KARLSRUHE

Institut für Kernphysik

KfK 3792

Pionabsorption in flight on ^3He *

Sven H. Ljungfelt

Kernforschungszentrum Karlsruhe GmbH, Karlsruhe

* von der Fakultät für Physik der Universität Karlsruhe genehmigte Dissertation

Als Manuskript vervielfältigt
Für diesen Bericht behalten wir uns alle Rechte vor

Kernforschungszentrum Karlsruhe GmbH
ISSN 0303-4003

PION ABSORPTION IN FLIGHT ON ^3He

ABSTRACT

Pion absorption in flight on ^3He has been measured in a kinematically complete manner. The experiment was done in the πE1 -channel at the Swiss Institute for Nuclear Research, SIN, using π^+ - and π^- -beams of 120 and 165 MeV kinetic energy.

Two of the emitted particles were measured in coincidence and identified by their time-of-flight/pulseheight relation. The obtained two-dimensional energy representation enabled a separation of the different kinematical regions and exhibited a clear enhancement in the region of quasifree absorption, QFA.

$$\text{The Isospin Ratios } R(^3\text{He}) = \frac{\sigma(\pi^+, pp)}{\sigma(\pi^-, np)}$$

were determined for various combinations of energies and angles. Together with our previous data obtained with pions at rest, the present results provide a homogeneous set of R values from kinematically complete experiments over a wide energy range.

The measured values deviate considerably from the value expected from simple isospin considerations, not considering the orbital angular momentum of the pion. Present theoretical calculations give qualitative understanding of the energy dependence of the isospin ratio but are in gross disagreement with the measured absolute values.

Preliminary results on the differential cross sections are also given. By using partly unpublished results from other authors about the angular dependence, integrated cross sections for our data are obtained. The integrated cross section for pion absorption on a $T=0$ nucleon pair exhibit an energy dependence consistent with the deuteron cross section taking into account the number of such nucleon pairs in ^3He . The energy dependence of the integrated cross section for absorption on a $T=1$ nucleon pair is presented for the first time. This cross section was not found to vary significantly with the energy within the analysed energy range. This partial result is qualitatively consistent with the predictions of the isobar model.

PION ABSORPTION IM FLUGE AN ^3He

ABRISS

Pion-Absorption im Fluge an ^3He wurde in einem kinematisch vollständigen Experiment gemessen. Das Experiment wurde am Schweizerischen Institut für Nuklearforschung, SIN, mit π^+ und π^- Strahlen von 120 und 165 MeV kinetische Energie durchgeführt.

Zwei der emittierten Teilchen wurden in Koinzidenz gemessen und mittels der Flugzeit/Pulshöhen-Beziehung identifiziert. Die gewonnene zweidimensionale Energieverteilung ermöglicht eine Trennung der verschiedenen kinematischen Bereiche. Eine solche Darstellung weist eine deutliche Häufung im Bereich der quasifreien Absorption, QFA, auf.

$$\text{Das Isospin-Verhältnis } R(^3\text{He}) = \frac{\sigma(\pi^+, pp)}{\sigma(\pi^-, np)}$$

wurde bestimmt für verschiedene Kombinationen von Pionen-Energien und Winkeln. Die Ergebnisse liefern zusammen mit unseren früheren Messwerten für die Absorption in Ruhe einen homogenen Satz von R-Werten über einen grossen Energie-Bereich. Die gemessenen Werten weichen beträchtlich von dem Wert, der aufgrund reiner Isospinbetrachtungen ohne Berücksichtigung des Pion-Bahndrehimpulses erwartet wird, ab. Gegenwärtige theoretische Berechnungen ergeben ein qualitatives Verständnis der Energieabhängigkeit des Isospin-Verhältnisses, obwohl noch grosse quantitative Unterschiede bestehen.

In der Arbeit werden auch vorläufige Ergebnisse über absolute differentielle Wirkungsquerschnitte angegeben. Unter Verwendung von teilweise unveröffentlichten Ergebnissen anderer Autoren über die Winkelabhängigkeit wurden daraus integrierte Wirkungsquerschnitte berechnet. Dabei zeigt sich, dass der Wirkungsquerschnitt für Pionabsorption an ein $T=0$ Nukleonpaar eine Energieabhängigkeit aufweist, die mit derjenigen des Deuterons unter Berücksichtigung der Anzahl np-Paare mit $T=0$ in ^3He übereinstimmt. Die Energieabhängigkeit für ein $T=1$ Nukleonpaar wird erstmals dargestellt. Der Absorptionsquerschnitt zeigt keine wesentliche Energieabhängigkeit im untersuchten Bereich. Dieses Teilergebnis stimmt qualitativ mit den Vorhersagen des Isobar-Modells überein.

TABLE OF CONTENTS

	- page -
1. INTRODUCTION	3
2. THEORETICAL SURVEY	5
2.1. PREREQUISITES	5
2.2. SELECTION RULES	6
2.3. ISOSPIN SYMMETRY CONSIDERATIONS	7
2.4. MODELS OF TWO-BODY ABSORPTION MECHANISM	13
3. THE EXPERIMENT	17
3.1. THE SIN MESON FACTORY FACILITY	17
3.1.1. General Layout	17
3.1.2. The π E1 Area	17
3.2. THE EXPERIMENT	21
3.2.1. The Liquid Target Dewar	21
3.2.2. The Beam Telescope	23
3.2.3. The Determination Of The Absolute Pion Rate	30
3.2.4. The Time-Of-Flight (TOF) Counter	31
3.2.4.1. General survey	31
3.2.4.2. Construction	35
3.2.5. The Charged Particle Detector	37
3.2.5.1. General layout	37
3.2.5.2. The E-counter	38
3.2.5.3. The MWP-chambers	39
3.2.6. The Experimental Set-Up	40
3.3. THE ELECTRONICS	43
3.3.1. General Purpose	43
3.3.2. The Telescope Logic	46
3.3.3. The E-Counter Electronics	48
3.3.4. The Chamber-Acquisition-System, CAS	51
3.3.5. The TOF-Counter Logic & The Central Coincidence	53
3.3.6. The Scalers	56
3.3.7. The Fast-Clear Facility	57
3.3.8. The Computer Link And The Dead Time Logic	58
3.3.9. Adaptation For TOF- Versus TOF- Coincidences	61
3.3.10. The Cosmic Ray Logic	62

3.4. THE ON-LINE DATA ACQUISITION SYSTEM	64
3.4.1. The On-Line Program	64
3.4.2. Sample Of On-Line Histograms	65
4. ADJUSTMENT AND CALIBRATION OF EQUIPMENT	69
4.1. TEST EVENTS	69
4.2. PROPERTIES OF THE TOF-COUNTER	71
4.3. CALIBRATION WITH COSMIC RAY MUONS	72
4.3.1. Calibration Of LED's	72
4.3.2. Alignement In Time Of A Counter Collumn	75
5. OFF-LINE DATA EVALUATION	77
5.1. SURVEY OF ANALYZED DATA	77
5.2. GENERAL LAYOUT OF THE EVALUATION	77
5.2.1. Particle Separation In the E-counter	78
5.2.2. Calculation Of The Energy In The Target	78
5.2.3. Calibration of The Pulse Height Spectra	79
5.2.4. Time Walk Corrections	80
5.2.5. Calibration Of The TOF-Spectra	80
5.2.6. Acceptance	83
6. RESULTS & CONCLUSIONS	85
6.1. THE ISOSPIN RATIO, R	85
6.2. DIFFERENTIAL CROSS SECTIONS	90
6.3. DISCUSSIONS & CONCLUSIONS	97
APPENDICES	
A. DESCRIPTION OF ELECTRONIC UNITS	99
B. PREPARATORY TEST OF THE TOF-COUNTER WITH COSMIC RAY MUONS	102
REFERENCES	

CHAPTER 1:INTRODUCTION

In 1935 Yukawa assumed that the nuclear interaction was governed by a potential $V(r) = V_0 \cdot e^{-\mu r} / r$. Analogous to the electromagnetic interaction which is mediated by the massless photon this interaction can be thought to be mediated by a particle of mass μ . With the known range of the nuclear force of about 1fm this corresponds to a mass of $\sim 200\text{MeV}$. In 1947 the *pion* was detected and found to have a mass in the predicted range. Since then we have seen the advent of the *Quantum Chromodynamics, QCD*, according to which the smallest nuclear constituents are *quarks* and the force between these is mediated by *gluons*. These entities, however, are not to be found free, but are confined in the strong-interacting particles, the *hadrons*, of which the pion is the lightest. Hence, according to the Yukawa-theory the pion can be said to mediate the long-range component of the strong interaction. QCD has not yet reached a stage where it can predict observables of hadronic-hadronic interactions. We have, therefore, to resort to a less fundamental theory.

A specific feature of the interaction between π -mesons and nuclei is the fact that pions as bosons can be absorbed. Pion absorption on a free nucleon is not possible because of momentum conservation. For a nucleon bound in a nucleus this process in principle does not violate either conservation of momentum or energy. However, the nucleon must possess a momentum before the absorption of about $500\text{MeV}/c$. This is extremely unlikely and can not account for the observed absorption rate.

Absorption on a single nucleon being unlikely, one usually assumes that pion absorption takes place on two nucleons, the residual nucleus acting as spectator. This is the so called 2N-model. Absorption by clusters of three or more nucleons is thought to be less important on the grounds that the probability of finding more than two nucleons very close together is much smaller than the corresponding probability for two nucleons. Actual absorption proceeding according to the 2N-model is called *quasifree absorption, QFA*.

The only bound 2N system found in nature is the deuteron which consists of a nucleon pair in a $T=0$ 3S_1 state. Considerable effort has been devoted to understanding the absorption on such a pair. The analogue process, in which the pion is absorbed by two nucleons in a $T=1$ 1S_0 state has received much

less attention. However, for complete microscopic understanding of pion absorption it is necessary to investigate pion absorption on nuclei heavier than the deuteron in which nucleon pairs with other quantum numbers are present.

The use of a light system is important in order to minimize the likelihood that the detected nucleons undergo secondary reactions obscuring the signature of the elementary absorption process. The simplest way to test the 2N-model is to add one extra nucleon to the NN-system. Of the two possibilities offered, ^3H and ^3He , tritium is disliked because of its radioactivity. As the nucleons in ^3He can be assumed to be in the relative s-shell [97], the angular momentum arguments are simple. In addition coincidence measurement of two of the three emitted particles offers the possibility to determine the final state in a kinematically complete manner without prohibitive effort. This permits a separation of the quasifree two-nucleon absorption (QFA) from other processes.

Such an experiment has recently been performed by our group using negative pions at rest and covering the whole kinematically allowed region. The results show a very strong preference for collinear events [3,44]:

- ☞ *About two third of all absorption processes occur as quasifree absorption on np- or pp- pairs with a ratio of $R=8.0 \pm 1.5$.*
- ☞ *The remaining third shows energy sharing among all three nucleons and is located in the final-state interaction regions, i.e. one nucleon has maximum momentum and the other two nucleons both have directions opposite to the aforementioned and zero relative momentum.*

The value of R mirrors the ratio of cross sections for absorption on $T=0$ and $T=1$ NN pairs and is larger than theoretical predictions for ^3He [78].

This work presents experiments performed with pions in flight at the Swiss Institute for Nuclear Research, SIN. π^+ - and π^- -beams of 80, 120 and 165MeV kinetic energy were used. A review of selection rules for different intermediate states, a calculation of the isospin ratio according to simple symmetry arguments and a discussion of the absorption mechanism is given in chapter 2. The experiment is described in chapter 3. In chapter 4 the calibration of the equipment is treated. The off-line evaluation is described in chapter 5. Finally, in chapter 6 the results are presented, discussed and conclusions drawn.

CHAPTER 2: THEORETICAL SURVEY

2.1 PREREQUISITES

Pions play an important role in atomic nuclei. The short range attractive force between nucleons, which is responsible for the existence of atomic nuclei, is dominated by the exchange of virtual pions. In the energy regime of the pion factories, the interaction of real pions with nuclei is governed by a single resonance. This is the Δ resonance, the first excited state of the nucleon. Since all states of a nucleon have the same baryon number, $B=1$, we call them isobaric states or simply isobars. The Δ isobar is characterized by the spin-isospin quantum number $(3/2, 3/2)$, by the mass $M_{\Delta} = 1232 \text{ MeV}$ and by the decay width $\Gamma_{\Delta} = 115 \text{ MeV}$. The main interactions of a pion with nuclei are scattering and absorption, which both in their energy dependence show the influence of the Δ resonance. The absorption process is assumed to go predominantly through a Δ as "doorway", i.e. the pion forms a delta with a nucleon and this Δ is consecutively de-excited in collisions with other nucleons in the nucleus.

It is usual to describe an interacting πN system by $L_{(2 \times \text{isospin})(2 \times \text{spin})}$ where L is the orbital angular momentum of the system. In this language the symbols N' and Δ represent P_{11} and P_{33} interacting πN systems. In the so called isobar model of pion absorption one of these isobars is formed in the intermediate state.

We will often make use of the word off-shell or off-mass-shell to describe the state of a particle. A particle is off-shell when its invariant mass is not equal to the mass of the free particle. A bound particle is off-shell corresponding to the binding energy in the nucleus.

We begin this chapter with an exposition of model independent features of absorption on a nucleon pair. In the first section we use the selection rules to find out when a formation of a Δ and N' is allowed in the intermediate state. The following section is dedicated to the Clebsch Gordon coefficients by means of which the measurable cross sections can be decomposed into cross sections for the different isospin channels. The last section treats recent theoretical approaches to the two-nucleon absorption mechanism.

2.2 SELECTION RULES

We consider pion absorption on a nucleon pair and assume the formation of either a Δ or a N' isobar in the intermediate state. The quantum numbers of concern to us are ℓ_π , L , S , J , T , τ and P . Here, \vec{L} is the relative orbital angular momentum between two baryons and \vec{S} and \vec{J} are the spin and the total angular momentum of the two-baryon system (NN, ΔN and $N'N$). The isospin of the baryon pair is denoted by T whereas we designate the isospin of the intermediate isobar by τ . P is the parity. For the total system the angular momentum, the isospin and the parity are conserved at any stage of the process. In addition the two-baryon system has to obey the generalized Pauli principle. The selection rules for the total system are listed in table 2.1.:

Selection rule	Initial state $\pi + NN$	Intermediate state ΔN or $N'N$	Final state NN	Fixed Quantum numbers
Isospin conservation	$\vec{T}_\pi + \vec{T}_{i(initial)}$	$= \vec{\tau} + \vec{T}_N = \vec{T}'$	$= \vec{T}_{f(final)}$	$t_\pi=1, t_N=1/2$
Parity conservation	$(-1)^{\ell_\pi+1+L}$	$= (-1)^{L'}$	$= (-1)^{L'}$	$\tau=1/2$ or $3/2$
Generalized Pauli Principle	$(-1)^{L+S+\tau}$	$= (-1)^{L'+S'+T'}$	$= (-1)^{L'+S'+T'}$	$= -1$
Angular Momentum Conservation		$\vec{J}_\pi + \vec{J}_i$	$= \vec{J}'$	$= \vec{J}_f$

Table 2.1. Selection rules[†]

We will use the common notation $^{2s+1}L_J(T)$ to describe the state of a baryon-baryon system. For the incident pion, only the angular momentum and parity are of interest and it is described by j_π^P .

The nucleons in ^3He are to 90% in relative s-states ($L=0$) [97]. Hence, we consider that case only. According to the Pauli principle, the initial NN-pair can be in one of two states:

$$^3S_1(T=0) \text{ or } ^1S_0(T=1)$$

In table 2.2 the quantum numbers for permitted intermediate and final states are listed for incident pions with $j \leq 2$.

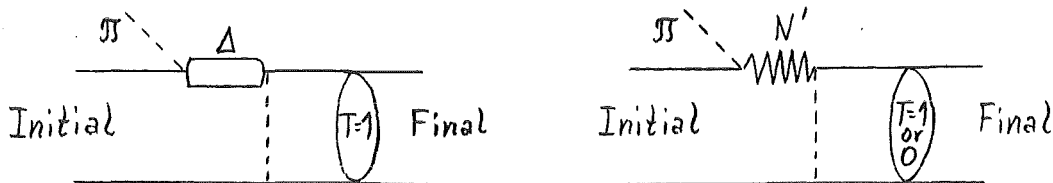


Figure 2.1. Absorption mechanism in the isobar model

[†]The primed quantum numbers refer to the ΔN or $N'N$ intermediate state.

Incident pion ($J_\pi \leq 2$)	Initial NN-pair $L=0$	Intermediate configuration		Final NN-pair $S=0$ or 1 , $T=0$ or 1
		ΔN $S=1$ or 2 , $T=1$	N'N $S=0$ or 1 , $T=0$ or 1	
0^-	$^3S_1(T=0);1^+$	$^3P_1;1^-$	$^3P_1(T=1);1^-$	$^3P_1(T=1);1^-$
	$^1S_0(T=1);0^+$	$^3P_0;0^-$	$^3P_0(T=1);0^-$	$^3P_0(T=1);0^-$
1^+	$^3S_1(T=0);1^+$	$^5D_0;0^+$	$^1S_0(T=1);0^+$	$^1S_0(T=1);0^+$
		$^5S_2, ^5D_2;2^+$	$^1D_2(T=1);2^+$	$^1D_2(T=1);2^+$
	$^1S_0(T=1);0^+$		$^3S_1, ^3D_1(T=0);1^+$	$^3D_1(T=0);1^+$
				$^3D_1(T=0);1^+$
2^-	$^3S_1(T=0);1^+$	$^3P_1;1^-$	$^3P_1(T=1);1^-$	$^3P_1(T=1);1^-$
		$^3P_2, ^3F_2;2^-$		$^3P_2(T=1);2^-$
				$^3F_2(T=1);3^-$
	$^3F_3;3^-$	$^3F_3(T=1);3^-$	$^3F_3(T=1);3^-$	
	$^1S_0(T=1);0^+$	$^3P_2, ^3F_2;2^-$		$^3P_2(T=1);2^-$
				$^3F_2(T=1);2^-$

Table 2.2. Permitted transitions

2.3 ISOSPIN SYMMETRY CONSIDERATIONS

Pion absorption on a free nucleon pair can be described by three independent cross sections. These represent the transition from an initial state of isospin T_i for the two nucleons to a final state of two nucleons with isospin T_f . Since T_i and T_f can both be 0 and 1, there exist 4 combinations. The case of $T_i = T_f = 0$, however, is not allowed because of isospin conservation in the absorption process.

We consider the nucleons to be in relative s-states ($L=0$). Since the Generalized Pauli Exclusion Principle requires $L+S+T$ to be odd, this implies that $S+T$ is odd. In table 2.3 the different absorption modes with their designated cross sections are listed for absorption on such a pair. The deuteron, the only bound NN-system, is a special case and corresponds to a 3S_1 $T=0$ state.

Nucleon pair	Initial state	Final state	Cross section designate	s- or p-wave pion	Final state
pp or nn	$T_i=1 ({}^1S_0)$	$T_f=1$	σ_{11}	s	3P_0
		$T_f=0$	σ_{10}	p	${}^3S_1, {}^3D_1$
np	$T_i=1 ({}^1S_0)$	$T_f=1$	σ_{11}	s	3P_0
		$T_f=0$	σ_{10}	p	${}^3S_1, {}^3D_1$
	$T_i=0 ({}^3S_1)$	$T_f=1$	σ_{01}	s	3P_1
				p	${}^1S_0, {}^1D_2$

Table 2.3. Cross sections for the different isospin channels.

We are interested in the probability of finding a given nucleon pair in a certain isospin state. An isospin state of a nucleon can be written

$$N = |T; T_3\rangle : p = |\frac{1}{2}; \frac{1}{2}\rangle ; n = |\frac{1}{2}; -\frac{1}{2}\rangle$$

The combination of two nucleons can be written in a representation which shows the individual states of the two nucleons, $NN=|T^1, T^2; T_3^1, T_3^2\rangle$, or in a representation showing the state of the NN-system, $NN=|T; T_3\rangle_{NN}$. Table 2.4 shows the transformation between the two representations. The transformation coefficients are the Clebsch-Gordon coefficients, $\langle T^1, T^2; T_3^1, T_3^2 | T; T_3\rangle$. The probability of finding a NN-pair in a specific isospin state is given by the square of these numbers. Thus, the probabilities of finding a np-pair in a $T=0$ or a $T=1$ state are both given by: $\frac{1}{2}$.

T_3^1	T_3^2	T	1	1	0	-1
			T_3	1	0	0
$\frac{1}{2}$	$\frac{1}{2}$	pp	1	0	0	0
$\frac{1}{2}$	$-\frac{1}{2}$	pn	0	$\frac{1}{\sqrt{2}}$	$\frac{1}{\sqrt{2}}$	0
$-\frac{1}{2}$	$\frac{1}{2}$	np	0	$\frac{1}{\sqrt{2}}$	$-\frac{1}{\sqrt{2}}$	0
$-\frac{1}{2}$	$-\frac{1}{2}$	nn	0	0	0	1

Table 2.4. Clebsch-Gordon coefficients

In a similar way we describe the state of the πNN -system

$$(\pi NN): |T^\pi, T^{NN}; T_3^\pi, T_3^{NN}\rangle$$

The following abbreviations will be used:

$$(\pi^+, pp): \pi^+ + pn \rightarrow pp; (\pi^+, pn): \pi^+ + nn \rightarrow pn$$

$$(\pi^-, nn): \pi^- + pn \rightarrow nn; (\pi^-, pn): \pi^- + pp \rightarrow pn$$

The cross-sections for the different absorption channels can now be written:

$$\sigma(\pi^-, nn) = \sigma(\pi^+, pp) = \sum_{T_i=0,1} |\langle \frac{1}{2}, \frac{1}{2}; \frac{1}{2}, -\frac{1}{2} | T_i; 0 \rangle|^2 \cdot |\langle 1, T_i; 1, 0 | 1; 1 \rangle|^2 \cdot \sigma_{T_i 1}$$

$$\sigma(\pi^-, pn) = \sigma(\pi^+, pn) = \sum_{T_f=0,1} |\langle 1, 1; -1, 1 | T_f; 0 \rangle|^2 \cdot \sigma_{1 T_f} \cdot |\langle \frac{1}{2}, \frac{1}{2}; \frac{1}{2}, -\frac{1}{2} | T_f; 0 \rangle|^2$$

With the Clebsch-Gordon coefficients [92]

$$T_i=0: \langle 1, 0; 1, 0 | 1; 1 \rangle = 1 ; T_i=1: \langle 1, 1; 1, 0 | 1; 1 \rangle = \frac{1}{\sqrt{2}}$$

$$T_f=0: \langle 1, 1; -1, 1 | 0; 0 \rangle = \frac{1}{\sqrt{3}} ; T_f=1: \langle 1, 1; -1, 1 | 1; 0 \rangle = -\frac{1}{\sqrt{2}}$$

this gives the following relations:

$$\sigma(\pi^-, nn) = \sigma(\pi^+, pp) = \frac{1}{2}\sigma_{01} + \frac{1}{4}\sigma_{11} ; \sigma(\pi^-, pn) = \sigma(\pi^+, pn) = \frac{1}{6}\sigma_{10} + \frac{1}{4}\sigma_{11} \quad (2.1)$$

The inverse reaction to pion absorption on a nucleon pair is NN single pion production, $NN \rightarrow NN\pi$. As in the case of pion absorption the cross section for pion production can be reduced to three independent cross sections. These can be extracted from pion production data by means of the relations (2.1). However, these data do not in general put any constraints on the states of the final NN-system. The final state is determined only in the special case when the emitted nucleon-pair is a deuteron. When the initial and the final state are fixed we can assume detailed balance i.e. the reaction and its inverse are governed by the same cross section, and only the difference in phase space has to be taken into account. Figure 2.2 shows the absorption cross sections obtained from pion production data [94][‡]. The σ_{01}^d -curve for absorption on a deuteron is correctly given, the other cross sections, however, include energy-dependent phase-space factors. Nevertheless we see that the σ_{01} absorption cross section is negligible for pion energies below ~ 250 MeV.

[‡]The cross sections of reference [94] includes Clebsch Gordon coefficients which have been canceled out.

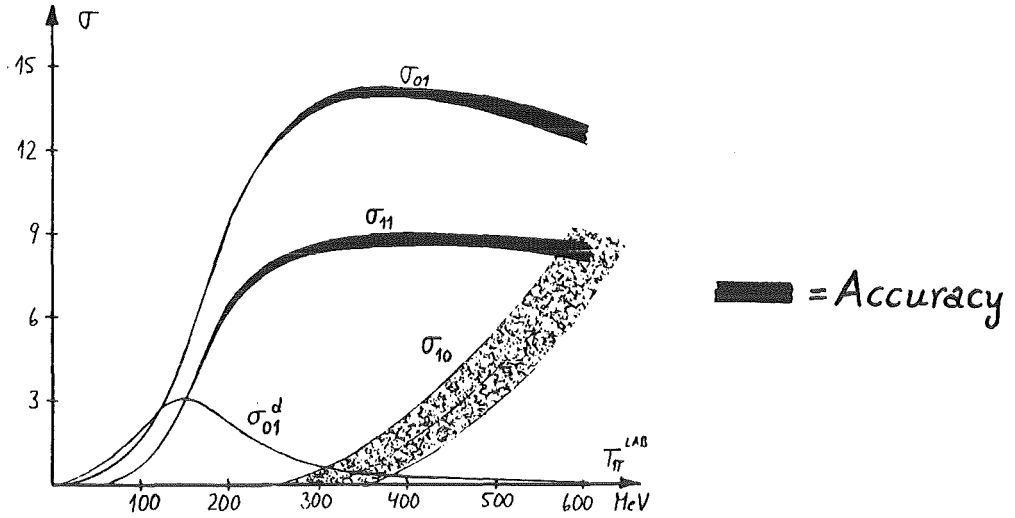


Figure 2.2. Cross sections for pion absorption on nucleon pairs obtained from pion production data, $NN \rightarrow NN\pi$, [94].

We now turn our attention to ${}^3\text{He}$. In ${}^3\text{He}$ we assume the nucleons to be in relative s-states ($L=0$). The cross sections for quasifree absorption on a np- and a pp- pair in ${}^3\text{He}$ can be written

$${}^3\text{He}[\sigma(\pi^-, nn)] = {}^3\text{He}[\sigma(\pi^+, pp)] = \sum_{T_i=0,1} N_{T_i}^{np} \cdot \left| \langle \frac{1}{2}, \frac{1}{2}; \frac{1}{2}, -\frac{1}{2} | T_i; 0 \rangle \right|^2 \cdot \left| \langle 1, T_i; 1, 0 | 1; 1 \rangle \right|^2 \cdot \sigma_{T_i,1}$$

$${}^3\text{He}[\sigma(\pi^-, pn)] = N_1^{pp} \cdot \sum_{T_i=0,1} \left| \langle 1, 1; -1, 1 | T_i; 0 \rangle \right|^2 \cdot \sigma_{1T_i} \cdot \left| \langle \frac{1}{2}, \frac{1}{2}; \frac{1}{2}, -\frac{1}{2} | T_i; 0 \rangle \right|^2$$

where $N_{T_i}^{NN}$ is the number of possible nucleon pairs with given charge and isospin in the ${}^3\text{He}$ nucleus. For isospin $T_i=0$ the spin S_i must be one. This gives us a three-fold degeneracy for $T_i=0$ versus no degeneracy for $T_i=1$. With two np-pairs accessible in ${}^3\text{He}$ we have

$$N_0^{np} = \frac{3}{2}, \quad N_1^{np} = \frac{1}{2} \quad \text{and} \quad N_1^{pp} = 1 \quad (2.2)$$

The cross sections are now

$${}^3\text{He}[\sigma(\pi^-, nn)] = {}^3\text{He}[\sigma(\pi^+, pp)] = \frac{3}{4}\sigma_{01} + \frac{1}{8}\sigma_{11} \quad (2.3)$$

$${}^3\text{He}[\sigma(\pi^-, pn)] = \frac{1}{6}\sigma_{10} + \frac{1}{4}\sigma_{11} \quad (2.4)$$

It is common to measure the ratio of quasi-free absorption on a np- to a pp-pair:

$$R(^3\text{He}) = \frac{{}^3\text{He}[\sigma(\pi^-, nn)]}{{}^3\text{He}[\sigma(\pi^-, pn)]} = \frac{{}^3\text{He}[\sigma(\pi^+, pp)]}{{}^3\text{He}[\sigma(\pi^-, pn)]} = \frac{\frac{3}{2}\sigma_{01} + \frac{1}{4}\sigma_{11}}{\frac{1}{3}\sigma_{10} + \frac{1}{2}\sigma_{11}} \quad (2.5)$$

A pion can couple to a nucleon giving an isospin $\frac{3}{2}$ or $\frac{1}{2}$. If one assumes dominance of a ΔN formation in the absorption process the final state must have $T=1$ since a $\Delta(T=\frac{3}{2}, S=\frac{3}{2})$ can not couple to a nucleon $N(T=\frac{1}{2}, S=\frac{1}{2})$ giving $T=0$. In this case $\sigma_{10}=0$ and the ratio R can be written

$$R = 3r + \frac{1}{2} \quad \text{where } r = \frac{\sigma_{01}}{\sigma_{11}} \quad (2.6)$$

is the isospin ratio. According to table 2.3 this last relation also applies to the case of absorption of an s-wave pion since in that case also a final state with $T=0$ is unattainable.

We can couple the isospins of the three particles (the pion and the two nucleons) in two different ways to obtain a total isospin T_f :

- ☞ by first coupling the isospin of the pion to one nucleon giving an isospin τ and then adding the isospin of the second nucleon. This corresponds to the isobar model.
- ☞ by first coupling the isospins of the nucleons giving an isospin T_i and then adding the isospin of the pion.

The transformation between the two possible representations of the total system is given by the isospin coupling coefficients $\langle T^\pi, (T^1 T^2) T_i; T_f | (T^\pi T^1) \tau, T^2; T_f \rangle$, [22,27]. Hence, by means of these coefficients the three cross sections mentioned earlier, $\sigma_{T_i T_f}$, can be expressed in terms of the cross section for forming a specific isobar $\sigma_{N'}$ and σ_Δ :

$$\sigma_{T_i T_f} = \sum_{\tau=\frac{1}{2}}^{\frac{3}{2}} |\langle 1, (\frac{1}{2} \frac{1}{2}) T_i; T_f | (1 \frac{1}{2}) \tau, \frac{1}{2}; T_f \rangle|^2 \cdot \sigma_\tau; \quad \sigma_\tau = \begin{cases} \sigma_{N'} & , \tau = \frac{1}{2} \\ \sigma_\Delta & , \tau = \frac{3}{2} \end{cases} \quad (2.7)$$

The isospin coupling coefficients can be expressed in terms of the more common Wigner-6j symbols [22,27]:

$$\langle 1, (\frac{1}{2} \frac{1}{2}) T_i; T_f | (1 \frac{1}{2}) \tau, \frac{1}{2}; T_f \rangle = (-1)^{T_f} \cdot \sqrt{(2T_i+1)(2\tau+1)} \cdot \begin{Bmatrix} 1 & \frac{1}{2} & \tau \\ \frac{1}{2} & T_f & T_i \end{Bmatrix} \quad (2.8)$$

The 6j symbols needed are listed below [27]:

$$\left\{ \begin{matrix} 1 & \frac{1}{2} & \frac{1}{2} \\ \frac{1}{2} & 1 & 1 \end{matrix} \right\} = -\frac{1}{3} \quad \left\{ \begin{matrix} 1 & \frac{1}{2} & \frac{1}{2} \\ \frac{1}{2} & 1 & 0 \end{matrix} \right\} = \frac{1}{\sqrt{6}} \quad \left\{ \begin{matrix} 1 & \frac{1}{2} & \frac{1}{2} \\ \frac{1}{2} & 0 & 1 \end{matrix} \right\} = \frac{1}{\sqrt{6}}$$

$$\left\{ \begin{matrix} 1 & \frac{1}{2} & \frac{3}{2} \\ \frac{1}{2} & 1 & 1 \end{matrix} \right\} = -\frac{1}{6} \quad \left\{ \begin{matrix} 1 & \frac{1}{2} & \frac{3}{2} \\ \frac{1}{2} & 1 & 0 \end{matrix} \right\} = -\frac{1}{\sqrt{6}} \quad \left\{ \begin{matrix} 1 & \frac{1}{2} & \frac{3}{2} \\ \frac{1}{2} & 0 & 1 \end{matrix} \right\} = 0$$

We now have:

$$\sigma_{11} = \frac{1}{3}(2 \cdot \sigma_{N'} + \sigma_{\Delta}) \quad (2.9a)$$

$$\sigma_{01} = \frac{1}{3}(\sigma_{N'} + 2 \cdot \sigma_{\Delta}) \quad (2.9b)$$

$$\sigma_{10} = \sigma_{N'} \quad (2.9c)$$

We can express R in terms of the cross section for forming a specific isobar

$$R = \frac{4\sigma_{N'} + \frac{13}{2}\sigma_{\Delta}}{4\sigma_{N'} + \sigma_{\Delta}} \quad (2.10)$$

Thus, if only isospin is considered, and one isobar is assumed dominant, R can be calculated by means of the isospin coupling coefficients

$$R(N') = 1 \quad ; \quad R(\Delta) = \frac{13}{2} \quad (2.11)$$

If either only s-wave or only p-wave pions are considered these ratios are

$$R_s(N') = 2 \quad ; \quad R_s(\Delta) = \frac{13}{2} \quad (2.12)$$

and

$$R_p(N') = \frac{3}{2} \quad ; \quad R_p(\Delta) = \infty \quad (2.13)$$

respectively, where the indices denote the wave of the incident pion.

2.4 MODELS OF THE TWO-BODY ABSORPTION MECHANISM

Pion absorption on a nucleon pair in a composite nucleus has its free counterpart in pionic disintegration of the deuteron. There exist large amount of cross section data for this process, $\pi d \rightarrow pp$, as well as its inverse (see [16] for a compilation). The recent theoretical models for this process fall into two, sometimes intertwining, categories. The earliest approach, as suggested by Mandelstam 25 years ago, is the lowest order perturbation method [52-59]. More recently another approach using coupled channels differential [60-62] or integral equations [63-71] has received much attention. The perturbative approach is more instructive and will be treated first. Figure 2.3 shows the first and second-order Feynman graphs in the model of the Regensburg-Michigan collaboration [52-57].

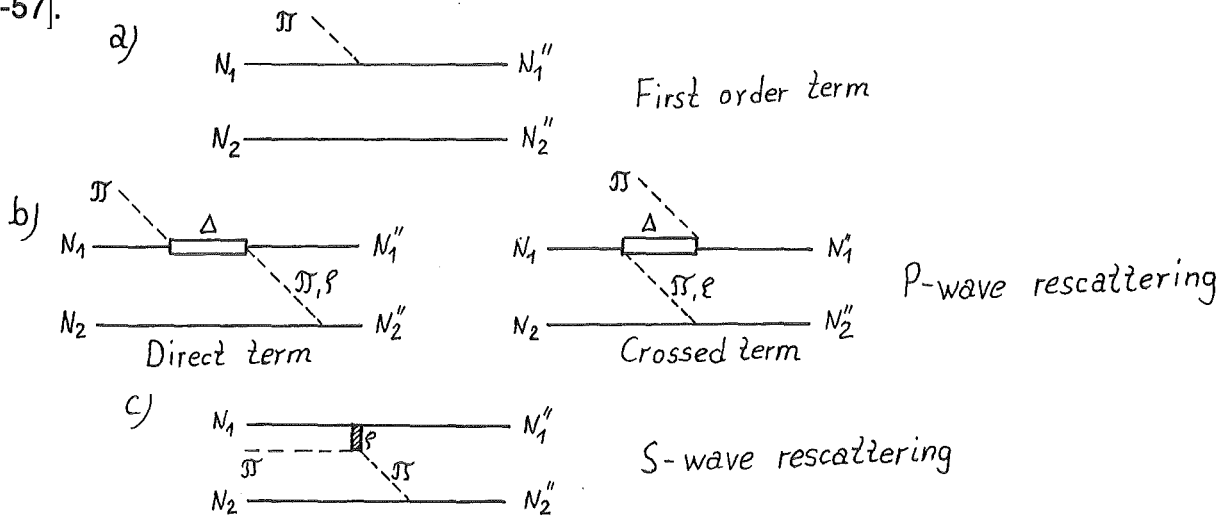


Figure 2.3. First and second order Feynman diagrams

The first order contribution, the *impulse approximation* where the pion gets absorbed on a single off-shell nucleon in the nucleus has been shown [52] to greatly underestimate the measured cross section. Second-order or *rescattering contributions* are favoured by the kinematics of the reaction which involve a large momentum and energy transfer between the nucleons. In this mechanism the pion scatters off on one nucleon, propagates off-mass-shell and is absorbed by the second nucleon (figure 2.3b). This effect is found to give a large contribution to the cross section and enables reasonable agreement with experiment to be obtained. At intermediate energies p-wave pion rescattering through an intermediate Δ formation dominates the total cross section. This resonant effect is manifested by a broad peak in the cross section. Near threshold the absorption process is dominated by s-wave rescattering. In this model the main contribution to s-wave πN scattering is due to ρ meson exchange as depicted in figure 2.3c.

In the lowest order perturbation theory model, the description of the pion rescattering is based on the use of phenomenological $\pi\pi NN$ Hamiltonian. The on-shell properties of this Hamiltonian are adjusted to reproduce free πN

scattering data. For absorption, the off-shell continuation of πN scattering enters and a phenomenological cut-off factor at the rescattering vertex has to be applied. Hence, one problem with this model is the large sensitivity to the range of the πNN -form factor. However, the inclusion of the exchange of a heavy vector meson, the ρ meson, leads to the use of form factors of far shorter range than is the case if only one pion exchange (OPE) contributions are included.

In the isobar model the absorption process on two nucleons involves two consecutive steps [60-63]:

- ☞ First, the pion forms an isobar with nucleon "1".
- ☞ Second, the isobar is de-excited in a two-body collision with nucleon "2".

The predominant process at intermediate energies, the formation of a Δ as doorway is depicted in figure 2.4.

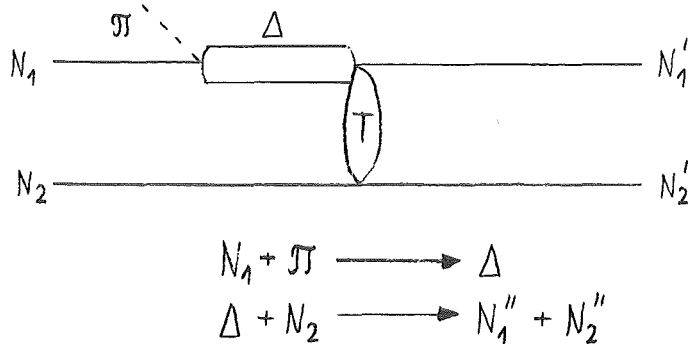


Figure 2.4. The formation of a Δ in the intermediate state.

Since the $\pi N \Delta$ vertex and the properties of the Δ are supposedly known from πN scattering, the new dynamics for pion absorption is contained in the $\Delta N \rightarrow NN$ transition matrix T . This T matrix is adjusted by comparison with NN scattering data. The so determined T matrix is not restricted to the lowest order rescattering terms but includes multiple rescattering diagrams to all orders. An approach using coupled two-body differential equations has been advocated by the Helsinki group [60-62]. The required amplitude $NN \rightarrow NN\pi$ is linked to that of $NN \rightarrow N\Delta$, including approximate treatment of the width of the Δ . One then solves for a system of coupled amplitudes for the NN - NN , NN - $N\Delta$, $N\Delta$ - $N\Delta$ with input so chosen as to reproduce NN observables. The solution then provides the ΔN - NN amplitude.

Within the past several years $\pi d \leftrightarrow pp$ experiments have been extended to include measurements with polarized proton beams i.e. measurements of the reaction $\vec{p}p \rightarrow \pi d$. Such measurements more severely constrain the models by providing additional information concerning the reaction dynamics. Recently calculations in the lowest order perturbation framework [56,57] and calculations by the Helsinki group [61] has been performed. An interesting feature of the comparison with the experimental data is the importance of higher partial waves. Near the resonance region the 1D_2 final NN state appear to be the most important followed by the 3F_3 state [61]. It is also found that the coupled channel

method is able to reproduce the experimental data to a better extent than the perturbative approach. This is taken as an indication that multiple rescattering effects are not negligible [56].

The most general approaches [63-71] are to use three-body coupled integral equations. They are mostly of generalized Faddeev-type with separable interactions. The amplitude, T , satisfies two- and three-particle unitarity.

Silbar and Piasezky [81] have used such a model [63] to calculate the differential cross sections for absorption on nucleon pairs in different isospin states. The isospin ratio R in ${}^3\text{He}$ according to eq.(2.2) has been calculated. No influence of the third nucleon is considered and only OPE interactions are taken into account. A ΔN and a $N'N$ configuration in the intermediate state are included in the calculation. They have used πN scattering data to obtain the form of the OPE interaction. Comparison with NN elastic scattering phase parameters have been made in order to test and adjust their model further. They predict a large suppression of the absorption on a 1S_0 ($T=1$) compared to a 3S_1 ($T=0$). We postpone the presentation of their results to chapter 6 where it is compared with our results.

Other three-body approaches have similar but not identical types of equations as Silbar et al. The main difference lies in the treatment of the short-range part of the baryon-baryon interaction, i.e. heavy boson exchange, which were neglected by Silbar et al. For example in Lee et al. [70,71] the short-range part is parameterized as a separable interaction and fitted to the high energy NN-scattering data. They have constructed a phenomenological Hamiltonian for pions, nucleons and Δ isobars. This Hamiltonian contains a $\pi N\Delta$ vertex and NN- $N\Delta$ two-body interactions. These interactions are strictly phenomenological, of separable form, and chosen such as to account for πN scattering up to 300MeV and for the NN phaseshifts and inelasticities up to 800MeV. Thus, Lee et al does not try to explain the physics of the πNN in terms of more fundamental "processes" but merely seeks a set of interactions that correctly describes it and can be used as input in many-body calculations. However, they have neglected nonresonant P11 interactions which play an important role at low energies. Also this channel may be of importance if the otherwise dominant Δ formation is suppressed. They have tested their model on the deuteron, comparing total and differential absorption cross sections and elastic scattering, with good agreement [70]. To further test their model they predict the isospin ratio in ${}^3\text{He}$ [79]. In accordance with Silbar et al. they predict a much larger isospin ratio than what would be expected from simple isospin considerations of last sections. In chapter 6 their calculations together with recent experimental data will be compared with our results.

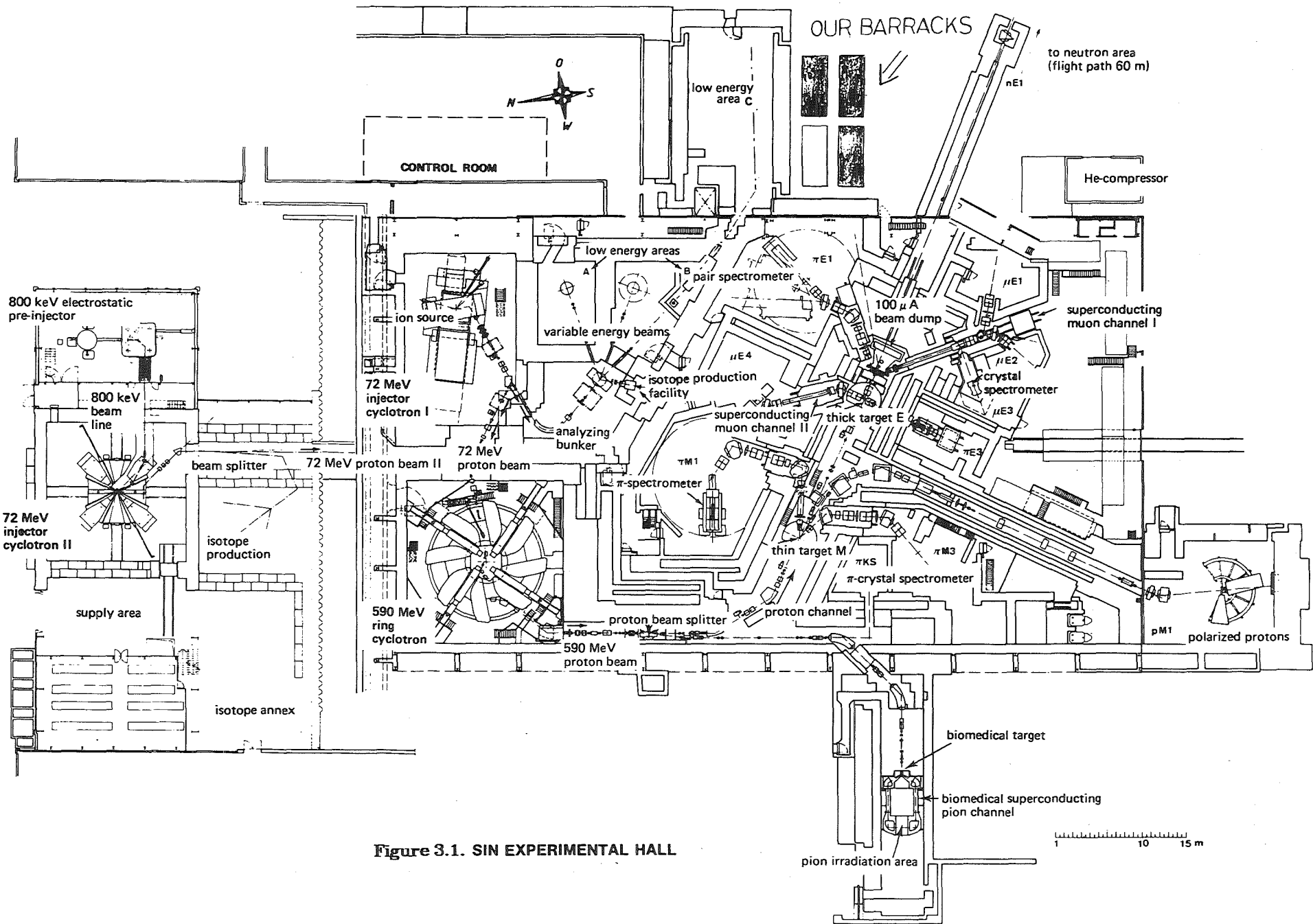


Figure 3.1. SIN EXPERIMENTAL HALL

CHAPTER 3: THE EXPERIMENT

3.1 THE SIN MESON FACTORY FACILITY

3.1.1 GENERAL LAYOUT

The experiment was performed at the Swiss Institute for Nuclear Research, SIN. The accelerator system consists of two separate machines, a sector focused injector cyclotron producing 72MeV protons (up to $170\mu\text{A}$) which are injected into the main ring accelerator. The cyclotron frequency is 50.7MHz. After about 250 revolutions in this isochroneous cyclotron a proton beam of about 590MeV is extracted and transported to the production targets M and E. Figure 3.1 shows the experimental hall of SIN.

The thin target M (5mm) produces 2 secondary pion beams and one proton beam for the experimental areas πM1 , πM3 and PM1 whereas the thick target E (120mm) supplies the areas πE1 , πE3 and $\mu\text{E1}-\mu\text{E4}$ with pion and muon beams respectively. All secondary beams are available simultaneously; the only coupling is in the momentum and polarity (opposite) of the πE1 -beam and the pions injected into the long superconducting μ -channel ($\mu\text{E1-3}$).

Our experiments have been performed in the πE1 -area. The electronics, power supplies and the on-line computer for data acquisition, a PDP11/40, are located in barracks outside of the experimental hall. The connection between the counters in the πE1 -area and the electronics in the barrack is provided by 35m cables corresponding to a time delay of about 170ns.

3.1.2. THE πE1 -AREA

This is an experimental area for an intense pion beam with an available momentum range from 125 to 450MeV/c (corresponding to a pion energy range from 50 to 350MeV). The πE1 -channel consists of 3 dipole magnets for defining the momentum and several quadrupoles for focusing, see figure 3.2.

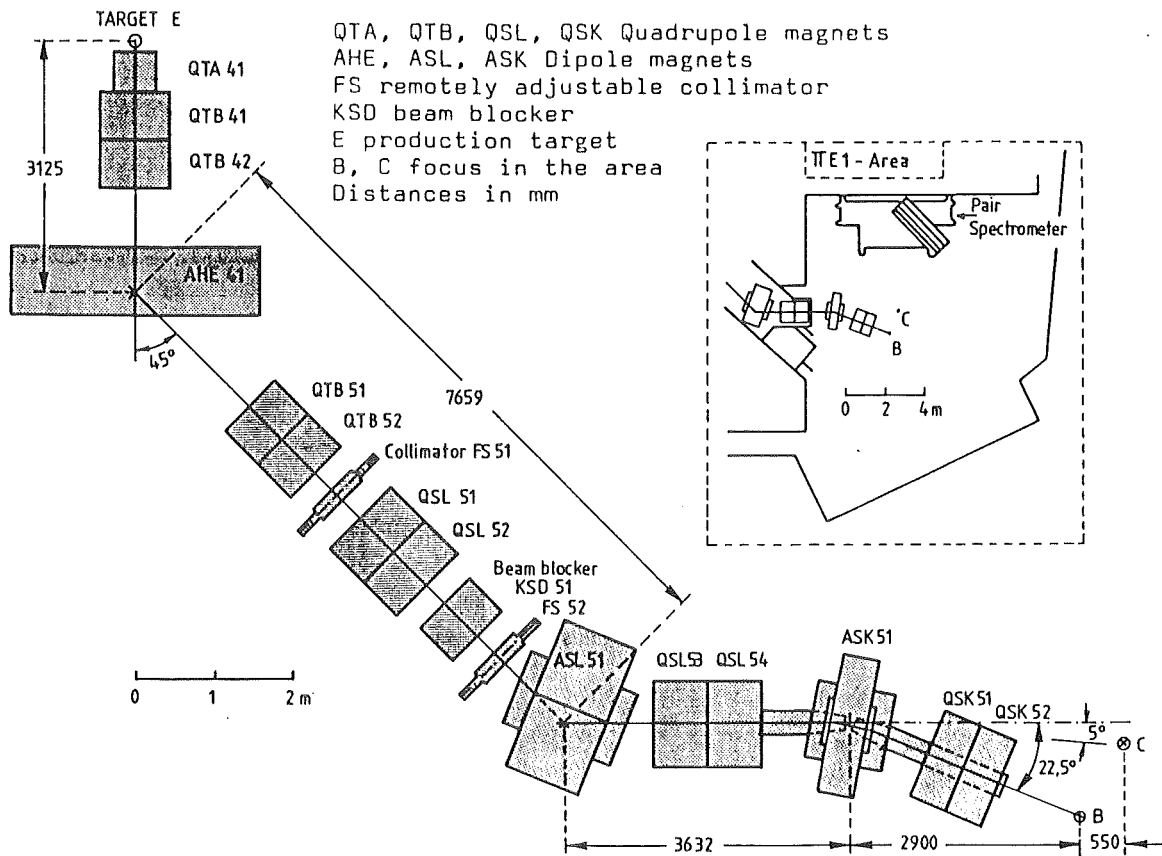


Figure 3.2. Beamline of the π E1-area

The first three quadrupole magnets and the first bending magnet (AHE41) are shared with the muon-channel. For this reason there are two modes of operating the π E1-channel:

- I "MAIN-USER" where the π E1-channel has priority.
- II "PARASITIC-USER" where the muon-channel has priority.

In target station E, normally a 12cm long Be-target is used for pion production. The pions are accepted at 0° by the first quadrupole triplet ($\Delta\Omega \approx 64\text{msr}$), then analyzed by the analyzing magnet AHE41 ($\frac{\Delta p}{p} \approx 14\% \text{FWHM}$) which is used to determine the central momentum of the pions. Beam envelopes of the existing beamline for the π E1-channel are shown in figure 3.3.

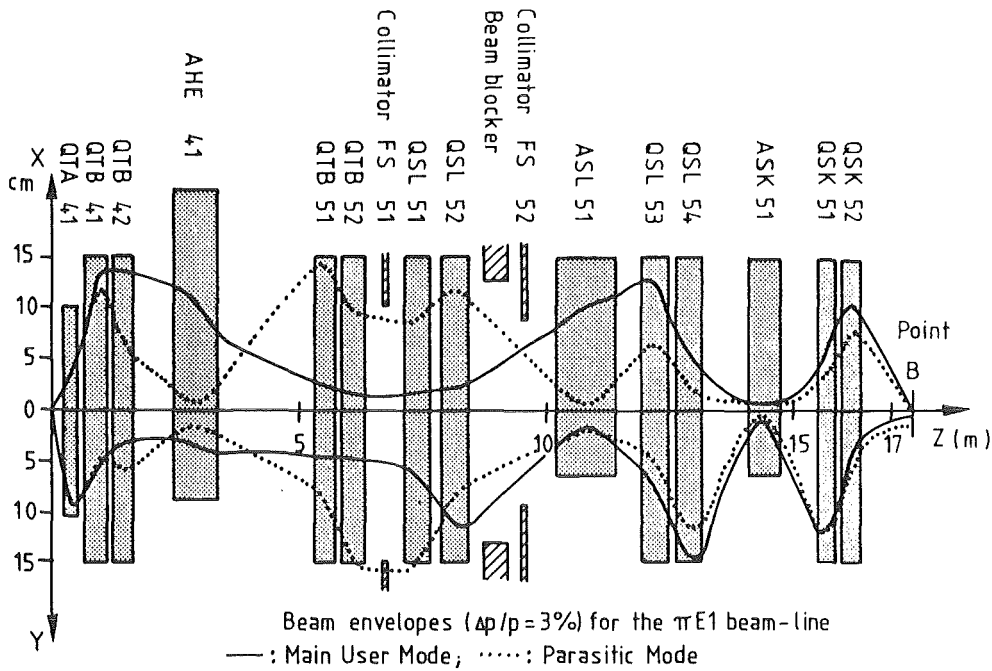
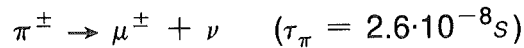


Figure 3.3.

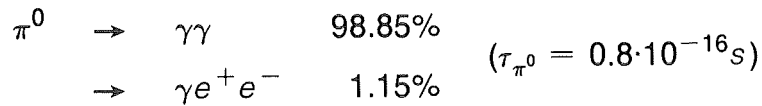
A variable collimator, FS51, is positioned in a dispersive focus of the beam-line and determines the momentum band. We are usually using a slit-setting corresponding to

$$\frac{\Delta p}{p} = 0.2 - 0.5\%$$

By choosing a magnet-setting we only select particles by charge and momentum and therefore a mixture of pions, muons and electrons will enter the target area. The muons are created through the pion decay



In the production target also neutral pions are produced which, however, immediately decay in the following channels



i.e. electrons and positrons are produced which, depending on charge and momentum, will be selected by the magnets. The contamination of the π E1-beam versus the momentum is shown in figure 3.4.

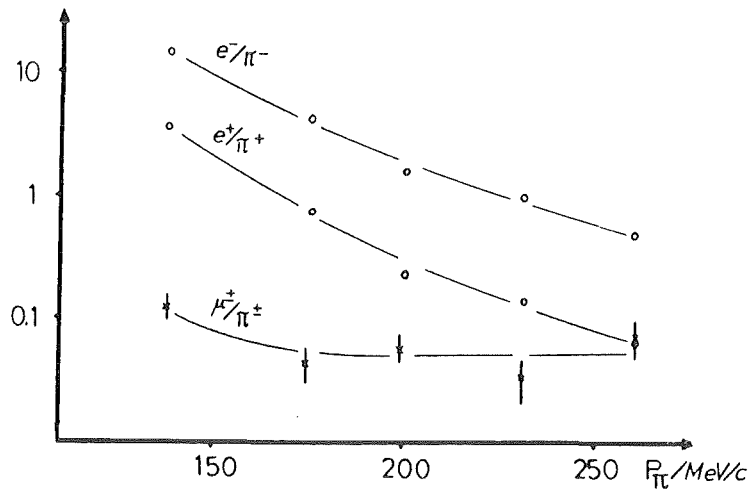


Figure 3.4. Contamination of the π E1-beam.

The large portion of electrons at low energies is a consequence of the high decay rate of the pion at low velocities.

The time structure of the beam at 220MeV/c is shown in figure 3.5. Microbursts of pions, muons and electrons enter the focal plane in the target area with 50MHz. The microbursts belonging to different particles will thereby be shifted in time to each other.

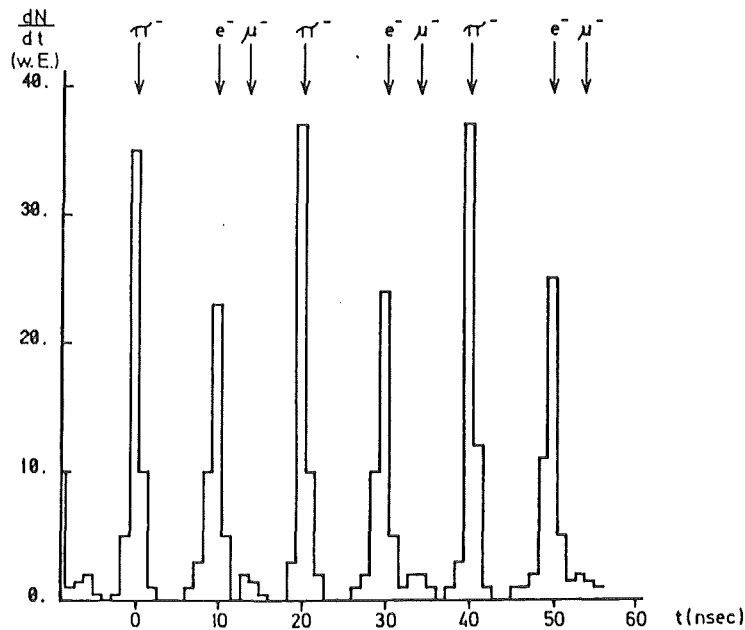


Figure 3.5. Microburst structure

Depending on the momentum the time structure is different, and the different particles are more or less separated in time. The time-of-flight for the different particles versus the momentum is shown in figure 3.6. The shaded area indicates the separation in time of the pions with respect to the next neighbouring other particle.

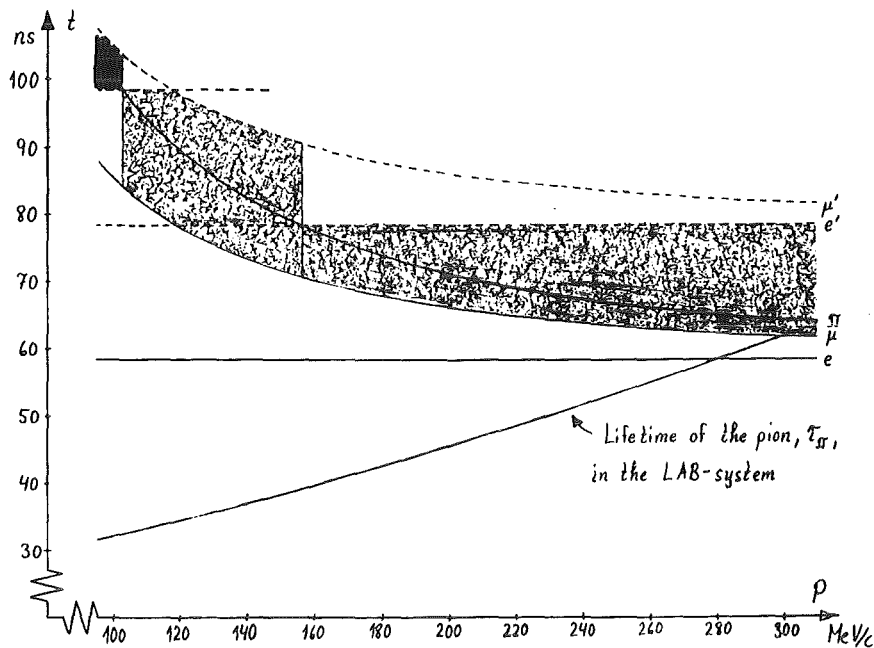


Figure 3.6. Time-of-Flight to the area for the different particles

3.2. THE EXPERIMENT

3.2.1. THE LIQUID TARGET DEWAR

For a ^3He target two principal possibilities exist: gas or liquid. Due to the low cross section for absorption in flight we decided to use a liquid target in order to achieve sufficient high counting rates for the coincidence experiment. The ^3He was cooled down to 2.8K (critical temperature 3.3K) giving a density of 69mg/cm^3 , [96]. The target cell is a rectangular copper frame [19cm(length) \times 6cm(height) \times 2.0cm(thickness)], covered with indium sealed Al foils, 18mg/cm^2 thick, on both larger sides, see figure 3.7.

This target can be turned around its vertical axis in order to minimize its thickness for protons emitted in the counter direction. The normal of the window was set to either 58° or 70° with respect to the beam direction. A pneumatic mechanism allows to lift the target assembly, so that two additional target frames can be brought into the pion beam, see figure 3.8b. To facilitate empty target measurements a dummy target was arranged below the ^3He target. It was covered on both sides with five aluminium foils of the type used for the main target in order to shorten the empty target measurement time. The second additional target is a copper plate with a pattern of holes to centre the beam.

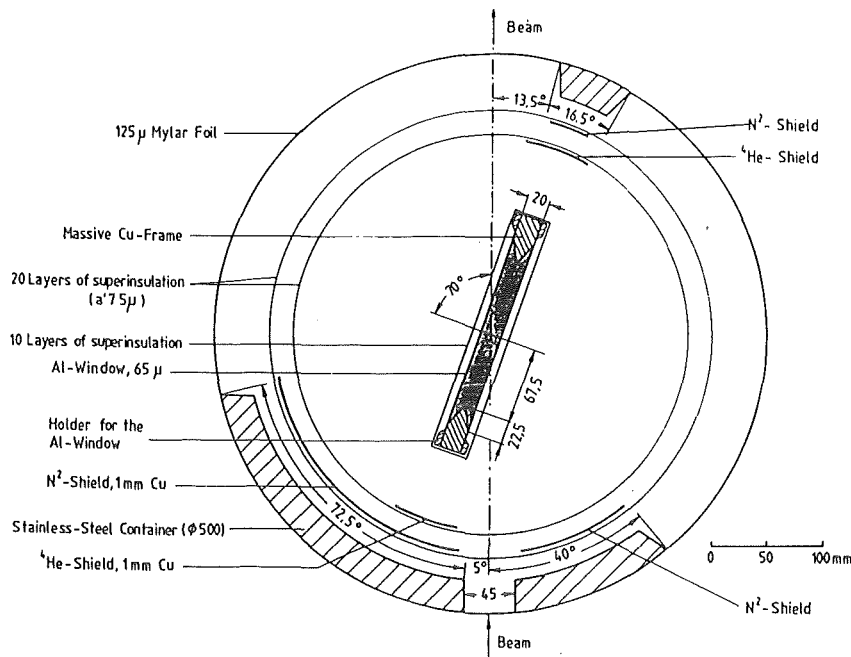


Figure 3.7a.

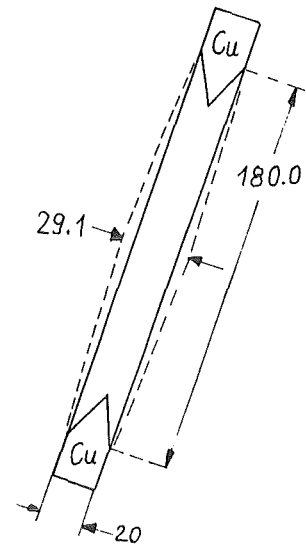


Figure 3.7b.

Cross section of scattering chamber with target cell

The closed circuit ^3He system is shown in figure 3.8a. The 150ℓ STP of ^3He available is stored in a separate tank. It is transferred to the target through an activated charcoal trap, kept at liquid nitrogen temperature, which removes impurities in ^3He . In case of a sudden warm-up, leading to an over-pressure exceeding 1.6atm, the ^3He is transferred, through a safety valve, back to the tank.

The design of the liquid target Dewar is shown schematically in figure 3.8b. The Dewar vessel is 0.5m in diameter and approximately 1.8m in height. The outer vacuum shield is made of stainless steel and consists of two halves that are bolted together with an O-ring seal. The top half has the liquid N_2 and ^4He baths mounted inside. The bottom half, see figure 3.7a, is the scattering chamber with a narrow entrance window to admit the pions, and two wide windows to allow for the escape of the reaction products. The outer heat shield is connected to the liquid nitrogen bath and thereby kept at 78K. The 38ℓ ^4He bath is in thermal contact with the innermost heat shield and with the target cells. The cool-down and removal of heat deposited by the beam is achieved by pumping on this bath. The average vapor pressure is thereby kept at 200mbar which corresponds to 2.8K. Each heat shield is covered by 10-20 layers of superinsulation resulting in a boil-off rate of only 4-5ℓ L ^4He per day. Since after the cool-down 17ℓ L ^4He remains the ^4He bath has to be refilled after 4-5 days. Like the scattering chamber the nitrogen shield and the helium shield, at the beam level, contains windows around the circumference. These apertures are 15cm high and are only covered by the 10-20 layers of superinsulation embracing the shields, see figure 3.7a.

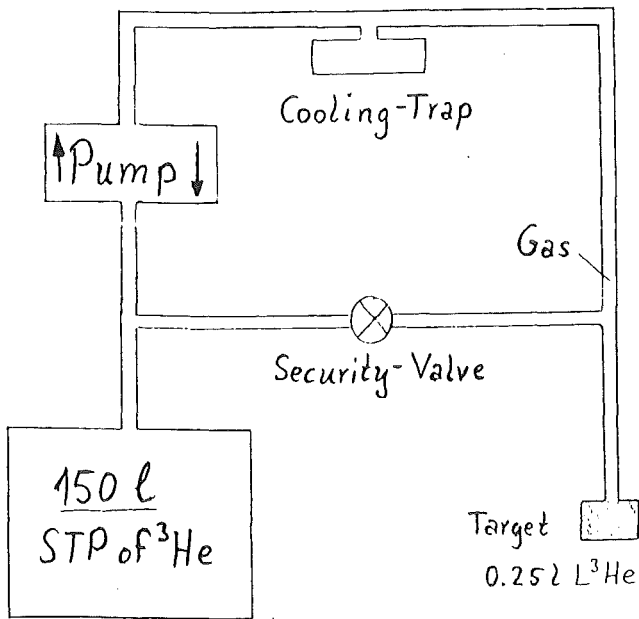


Figure 3.8a.
The ^3He system

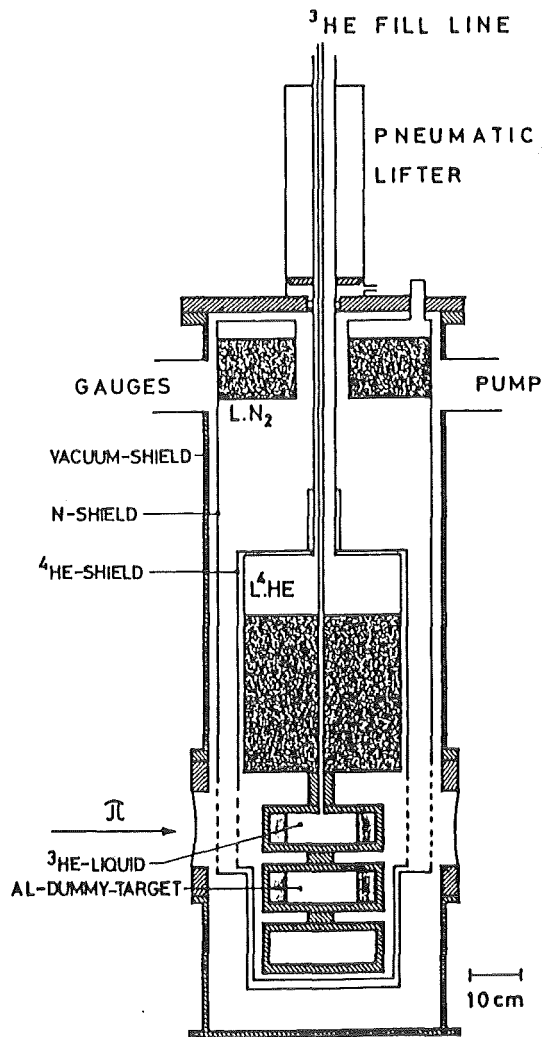


Figure 3.8b.
The liquid target dewar

During a regular experiment when the target is filled with ^3He the overpressure in the target will cause the target windows to bulge. In order to determine the thickness of the target due to this bulging a special vacuum chamber was constructed. This chamber featured two opposite glaswindows and a built-in illumination. By observing the target with a theodolite through a glasswindow the bulging of the aluminium windows was found to increase the thickness from 2.0 to 2.9cm. This results in a target volume of 0.25ℓ, see figure 3.7b.

3.2.2 THE BEAM TELESCOPE

The task of the telescope is to define the beam, monitor the beam intensity and to identify the pions. We are using two telescope counters; one large T1 (6mm thick, $16 \times 30\text{cm}^2$) near the last quadrupole and one T2 (1mm thick, $4 \times 5\text{cm}^2$) of the same size as the target, close to the entrance window of the target vessel and thereby defining the part of the beam hitting the target.

The very high beam intensity accessible in the π E1-area with a maximal flux of 10^{10} particles/s (~ 100 /burst) requires special precautions regarding the anode current in the photomultiplier. By employing the fast photomultiplier XP2230B and making use of a base with a built-in $10 \times$ preamplifier, the tubes can be operated with relatively low voltages (about 1800V) and thus the anode current reduced to a value below the critical $1\mu\text{A}$. Furthermore, to improve the time resolution and to avoid any attenuation of the analogue signals due to long cables, remote controlled fast discriminators were installed in the vicinity of the counters in the area.

Figure 3.9. shows the measured rate of a counter covering the total beam ($10 \times 10\text{cm}^2$) versus the rate of a very small counter ($0.1 \times 0.1\text{cm}^2$) for different beam intensities. Under the assumption that the beam geometry is independent of the intensity, we would expect to measure a linear relation. In fact, owing to increasing saturation and double events (two inseparable particles in one burst) in the large counter, the measured curve deviates considerable from a straight line. The experiment was, however, carried out with intensities at which the telescope is still operating in the linear range mentioned above.

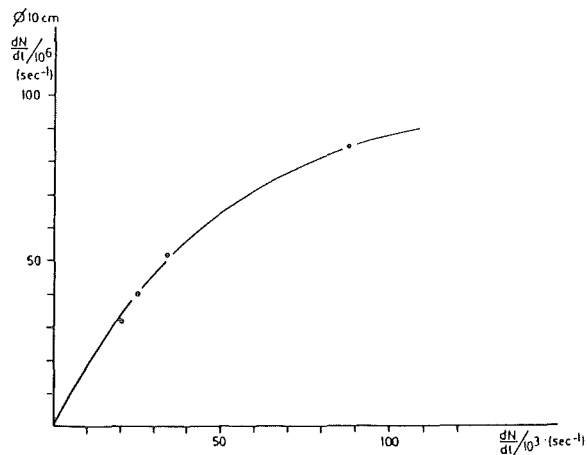


Figure 3.9. Rate of counter covering the total beam vs. a very small counter

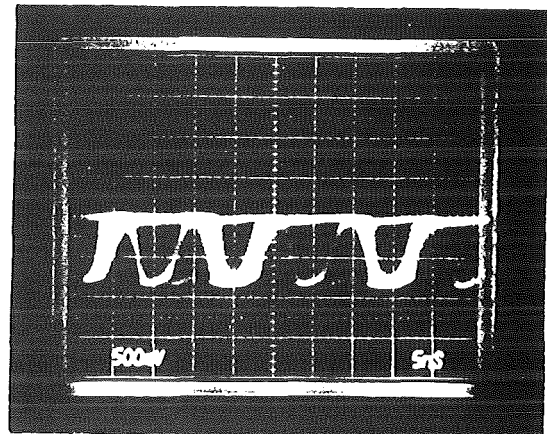
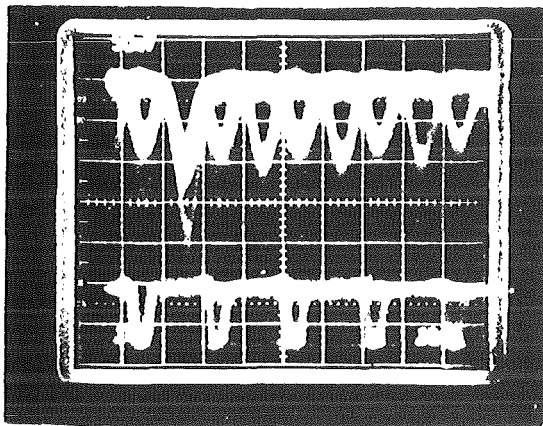


Figure 3.10. Oscilloscope photos of telescope signals

a) Analogue signal from a telescope counter. On the second channel the 50MHz RF-signal is seen.

b) Discriminator signal from a telescope counter.

The oscilloscope photos shows the analogue and the discriminator signals of a telescope counter. The oscilloscope was triggered by the 50MHz cyclotron frequency (RF). The pions are recognized by their higher pulse heights. We see that with a discriminator width of 4ns in coincidence with the RF we are able to select the pions.

3.2.3 DETERMINATION OF THE ABSOLUTE PION RATE

In order to be able to determine absolute cross sections, we need to know the absolute number of pions impinging upon the target. As we saw in the last chapter, at certain momenta, notably 150MeV/c, the telescope facility fails to separate the pions from the other particles. Only on certain occasions is the accelerator operated with a 60ns beam structure (17MHz) which allows for a separation also at such energies. Apart from that, the determination of the absolute number of pions fails when the probability of finding more than one pion in a burst is not negligible. As shown in the last section the photomultiplier is working properly up to a total flux of about 10^7 particles/s.

To solve the problem with the determination of the absolute pion rate several methods have been taken into consideration [14]:

- A *Using a differential Čerenkov counter counting only pions.*
- B *Using a telescope counter made up of many hodoscope.*
- C *Using the charge-exchange reaction (π^\pm, π^0) with known cross section.*
- D *Using the activation method.*

We have chosen the activation method (D): in this method a suitable material, of the same size as the target, positioned in front of the entrance window of the target vessel, is kept in the beam a certain time, after which it is taken out and its radioactivity measured. The so determined absolute number of pions impinging upon the target, n , is proportional to the number of particles, $n_s = \varepsilon n$, seen by the so called beam monitor which is a counter operating in the linear range. Thus, after determining the proportionality constant ε we are able to view the absolute pion flux by means of the beam monitor rate written on tape. Since ε is dependant on the momentum, polarity and beam quality we have to perform an activation measurement after every change in beamline.

For our purpose the reaction:



suits us exceptionally well since the life time is in the right order of magnitude, the cross section is well established for different pion momentum [95] and a usual plastic scintillator can be used as the material to activate and later to detect the β^+ . Since the β^+ -spectrum of the ^{11}C has the high maximum energy of 1 MeV, only a small fraction of the spectrum will lie below the threshold of the electronics so that a high detection efficiency is obtained in the β -counter ($\varepsilon_\beta > 90\%$). In addition the annihilation radiation of the positron is detected in a NaI-counter. Since the β^+ -decay leads to the ground state of the ^{11}B no other

γ -radiation occurs save the two collinear γ 's with 0.51MeV each. To make sure that only one of the γ 's and no β^+ is detected in the NaI-crystal the cover of the plastic scintillator is designed as a β -absorber. Hence, the β^+ from the ^{11}C -decay comes to a stop somewhere between the cover and the photomultiplier of the β -counter. Figure 3.11 shows the apparatus for detection of the radiation.

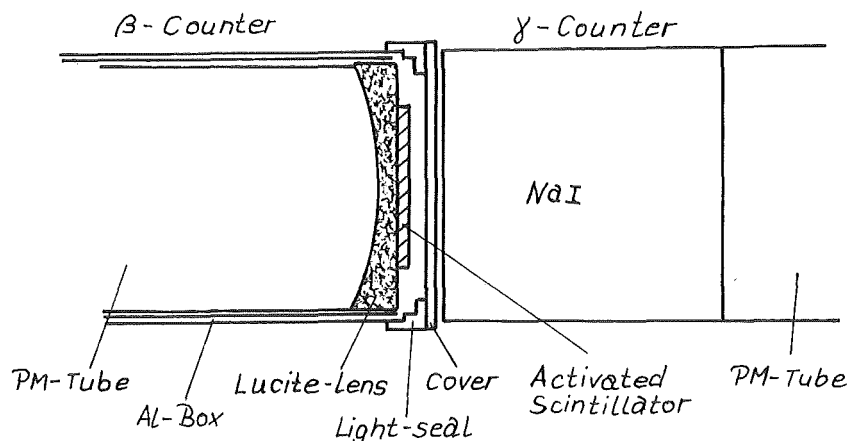


Figure 3.11. The counter set-up.

Under these circumstances, with a γ -efficiency ϵ_γ and a decay rate n , the counting rate in the γ -counter is $n_\gamma = 2\epsilon_\gamma n$. The counting rate in the β -counter is $n_\beta = \epsilon n$ and the coincidence rate is given by $n_c = 2\epsilon_\beta \epsilon_\gamma n$. Thus we have the following relation

$$n = \frac{n_\beta \times n_\gamma}{n_c} \quad (3.1)$$

i.e. we can determine the absolute intensity without knowing the efficiencies of the counters involved.

In the course of a diploma work [14] an apparatus has been developed and tested for convenient data taking. Figure 3.12 represents the electronics for the activation measurement.

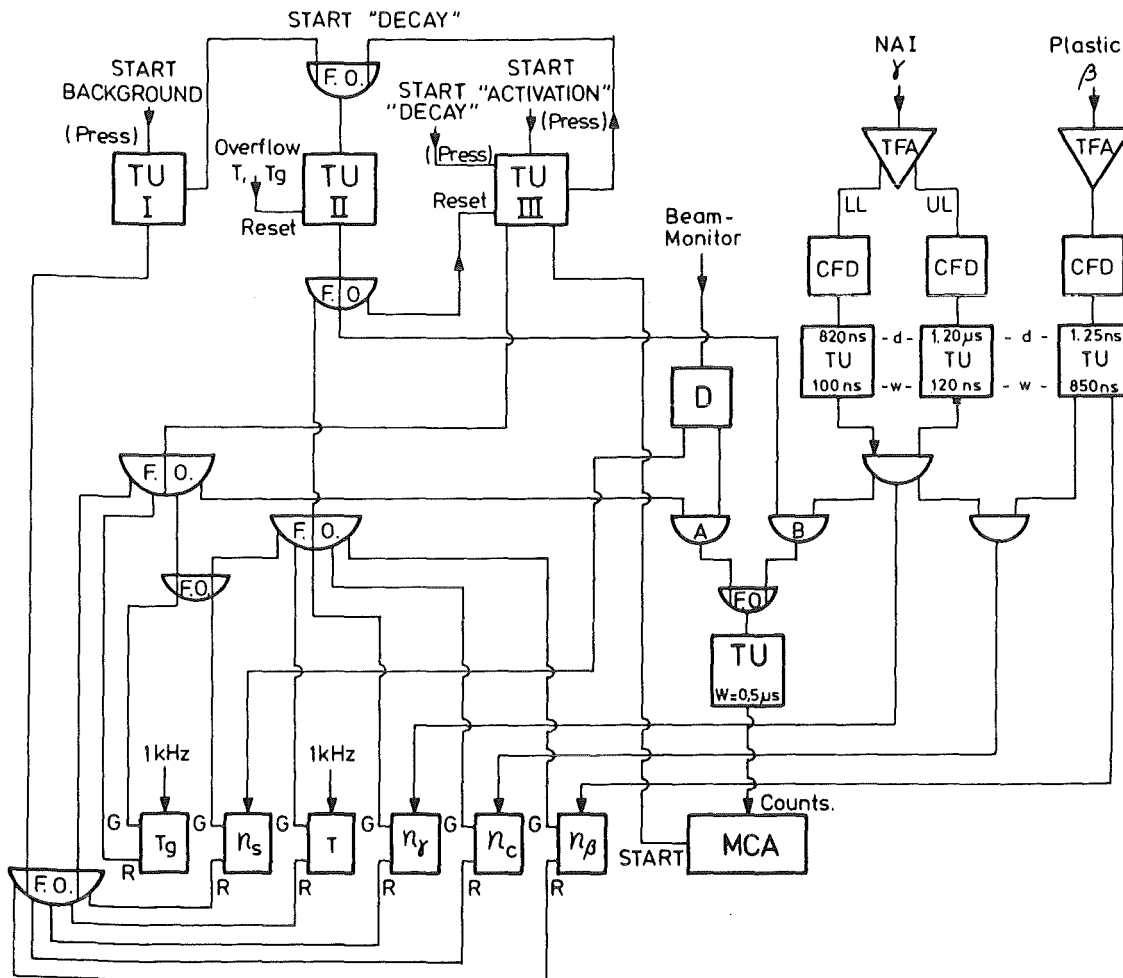


Figure 3.12. Electronics for the activation measurement

Prior to the opening of the beam blocker for activation the Timing Unit (TU) III is started, thereby

- ☞ activating the multichannel analyzer (MCA) which is working in the multiscaling mode. In this mode the number of events during a time $t=0.8s$ is collected in one channel whereupon it automatically advances to the next channel.
- ☞ via the coincidence A connect the beam monitor with the input of the MCA.
- ☞ clearing all scalers and turning on the scalers counting the beam monitor events, n_s , and total time T_g .

After the exposure the scintillator is put on the photomultiplier of the β -detector and the apparatus is adapted for measurement of the induced activity. It is achieved by resetting TU III by hand and thereby start TU II. This will cause:

- ☞ the γ -counter via the coincidence B to be connected to the input of the MCA.
- ☞ the remaining scalars to start.

The measurement of the induced activity is stopped after a total time T_g of 3000s which is equivalent to 3750 channels out of the total of 4096 channels available on the MCA.

Figure 3.13. shows a typical MCA-spectrum.

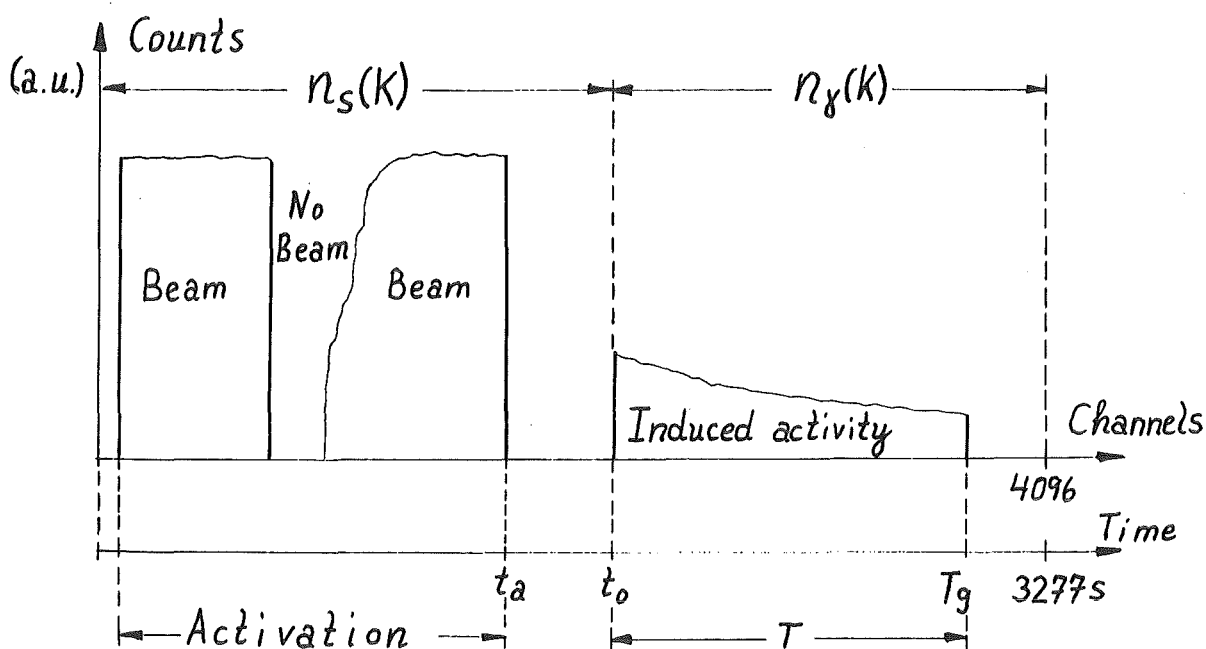


Figure 3.13. MCA-spectrum

The time needed for activation, t_a , depends linearly on the beam intensity and the thickness of the material. In figure 3.14 t_a versus the kinetic energy is drawn for π^+ and π^- using a 2 mm thick scintillator and requiring at least a decay rate of 100/s, 10 min after the activation for a nominal beam intensity of $10^6 \pi/s$.

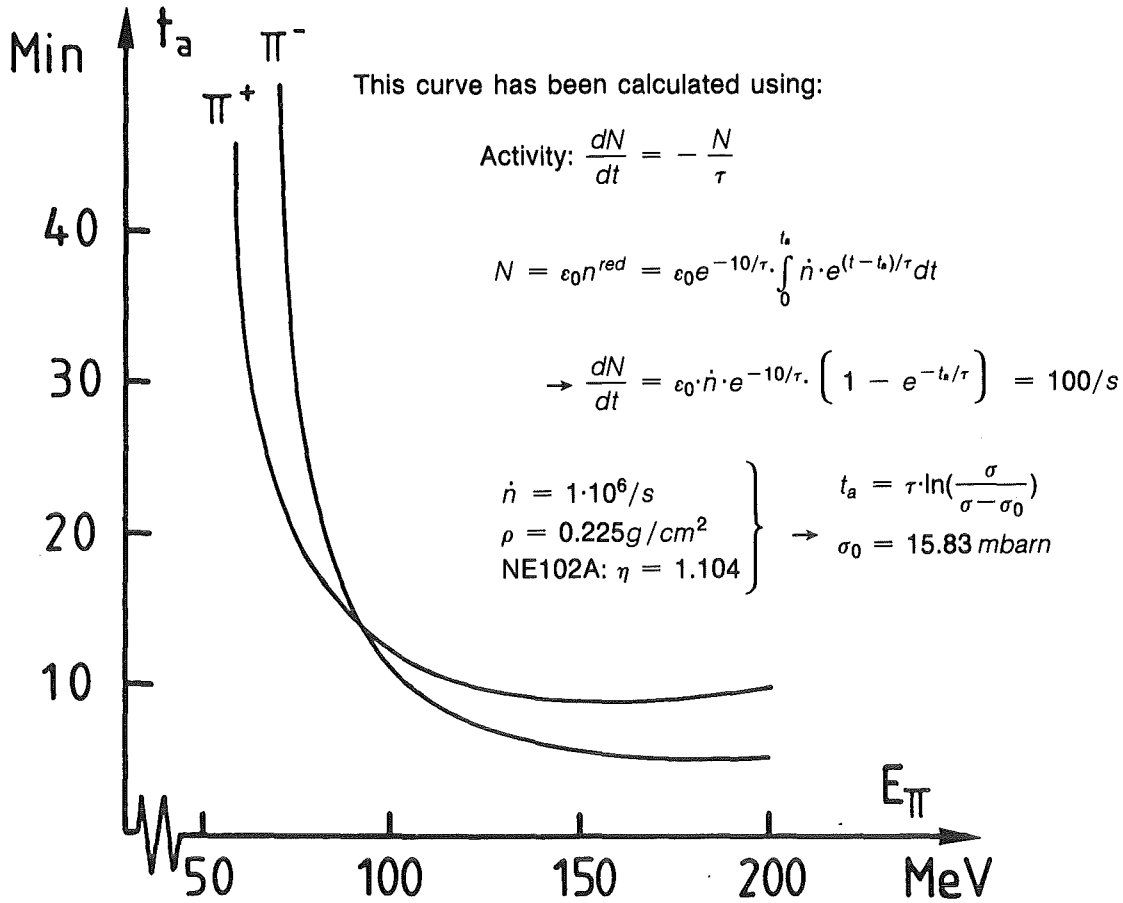


Figure 3.14. Time required to activate the probe.

The number of created ^{11}C -atoms, N , is related to the number of pions hitting the probe, n , by

$$N = \varepsilon_0 \cdot n \quad \text{where} \quad \varepsilon_0 = \frac{\rho}{C_{bw} \cdot m} \cdot \sigma \quad (3.2)$$

with C_{bw} = the percentage of carbon by weight:

$$C_{bw} = \frac{A(^{12}\text{C})}{\{A(^{12}\text{C}) + \eta A(^1\text{H})\}} \approx \frac{12}{(12 + \eta)} \quad \text{where}$$

A is the molar weight [g/Mol] and
 η is the ratio of H- to C- atoms.

ρ = the surface density [g/cm²].

m = the mass of a carbon atom [g]:
 $m = A(^{12}\text{C})/N_A = (12/6.022) \cdot 10^{-23} \text{g}$ where
 N_A = Avogadro's number.

σ = the reaction cross section

This gives

$$\varepsilon_0 = \frac{N_A \cdot \rho \cdot \sigma}{12 + \eta} \quad (3.3)$$

The ratio of the beam monitor rate to the incident pion rate is now

$$\varepsilon = \frac{n_s}{n} = \varepsilon_0 \cdot \frac{n_s}{N} \quad (3.4)$$

Since the number of existing ^{11}C -atoms at a certain time t (after the activation) is given by $N(t) = N_0 e^{-t/\tau}$, the number of decayed ^{11}C -atoms during the time T (t_0 to T_g) is

$$N(t_0) - N(T_g) = N(t_0)(1 - e^{-T/\tau}) = \int_{t_0}^{T_g} \dot{N}(t) dt \quad (3.5)$$

If we choose t_0 , the time of the start of the measurement of the induced activity, as reference time, the number of existing ^{11}C -atoms at that time is given by

$$N(t_0) = \int_{t_0}^{T_g} \dot{N}(t) dt / (1 - e^{-T/\tau}) \quad (3.6)$$

By taking into account the number of ^{11}C -atoms created but already decayed, the reduced beam monitor rate at time t_0 is

$$n_s^{red}(t_0) = \sum_{k=1}^{k=k(T)} n_s(k) \cdot \exp\left\{\left(k - \frac{1}{2}\right) \cdot t_k - t_0\right\} / \tau, \quad t_k \ll \tau \quad (3.7)$$

This number corresponds to a momentary activation at time t_0 producing a number of ^{11}C -atoms given by eq.(3.6). Thus the sought after relation is according to eq.(3.4)

$$\varepsilon = \frac{\varepsilon_0 \cdot n_s^{red}(t_0)}{N(t_0)} \quad (3.8)$$

The background of the γ -counter leads to the by far largest part of the uncertainty in the determination of $N(t_0)$. This is not solely because the share of the background for this counter is about 30 times as high as in the β -counter but also because of a dependance on the beam intensity. Since we want to keep the interruption of the regular measurement, due to the activation measurement as short as possible, the beam blocker is open during the activity measurement. The background of the γ -counter is determined from the approximately constant background rate, \dot{U}_γ^0 , with closed beam blocker and the number of beam counter events during the activity measurement, $n_s(T)$, with the ansatz

$$U_\gamma(T) = \dot{U}_\gamma^0 \cdot T + a \cdot n_s(T) \quad (3.9)$$

To determine the constant, a , prior to the activation, a background measurement with open beam blocker is made. The time spectrum of the induced activity, $n_\gamma(k)$, written on the MCA (see figure 3.13.), offers an additional check of the background.

The information on the MCA is conveyed on a magnetic tape. A program "CARBON" evaluates the data and calls upon discrepancies between the MCA-data and the scaler information.

Tests of the method have been made for low beam intensities. As beam monitor we were using T2 in coincidence with RF, called 2π , to select the pions hitting the target. The scintillator to be activated is attached to T2 and is of the same size. Thus, the ratio ϵ shall approach unity if we have been able to select the pions and everything works properly. Table 3.1. shows the ratio ϵ for various combinations of momenta and polarity.

Beam	80MeV (170MeV/c)	120MeV (220MeV/c)	170MeV (270MeV/c)
π^-	6.4	0.96	0.99
π^+	2.0	0.86	1.11

Table 3.1. Proportionality constant ϵ

At 80MeV we cannot separate the pions and ϵ is expected to be larger than unity.

3.2.4 THE TIME-OF-FLIGHT (TOF) COUNTER

3.2.4.1 GENERAL SURVEY

The task of the TOF-counter is to determine the kinetic energy and type of particle as well as the impact point on the counter surface. The counter should be suited for detection of neutrons, protons and deuterons.

Neutrons are detected by the scintillation light produced by the charged products of interactions between the incident neutrons and the nuclei of the scintillator. Of all scintillators the hydrocarbon scintillators have the highest cross sections for neutrons in our energy range (5-200MeV). They also have a very good time resolution (0.2-1ns). In our experiment we are using the common plastic scintillator NE102A from Nuclear Enterprise, see data sheet below.

Composition:	CH _{1.104} with 4.78·10 ²² C-atoms/cm ³
Density:	$\rho = 1.032\text{g/cm}^3$
Index of refraction:	n = 1.58
Wavelength of maximum emission:	$\lambda = 423\text{nm}$ (violette)
Rise-time: Decay-time:	$\left. \begin{array}{l} t_R = 0.9\text{ns} \\ t_D = 2.4\text{ns} \end{array} \right\} \rightarrow \text{FWHM} = 2.7\text{ns}$
Light attenuation length:	L = 250cm

Table 3.2. Manufacturers data-sheet on NE102A

Every neutron induced reaction process in the scintillator has a specific energy depending cross section, σ . The total cross section and the cross sections for the most important reaction channels in the hydrocarbon scintillator NE102A are shown in figure 3.15.

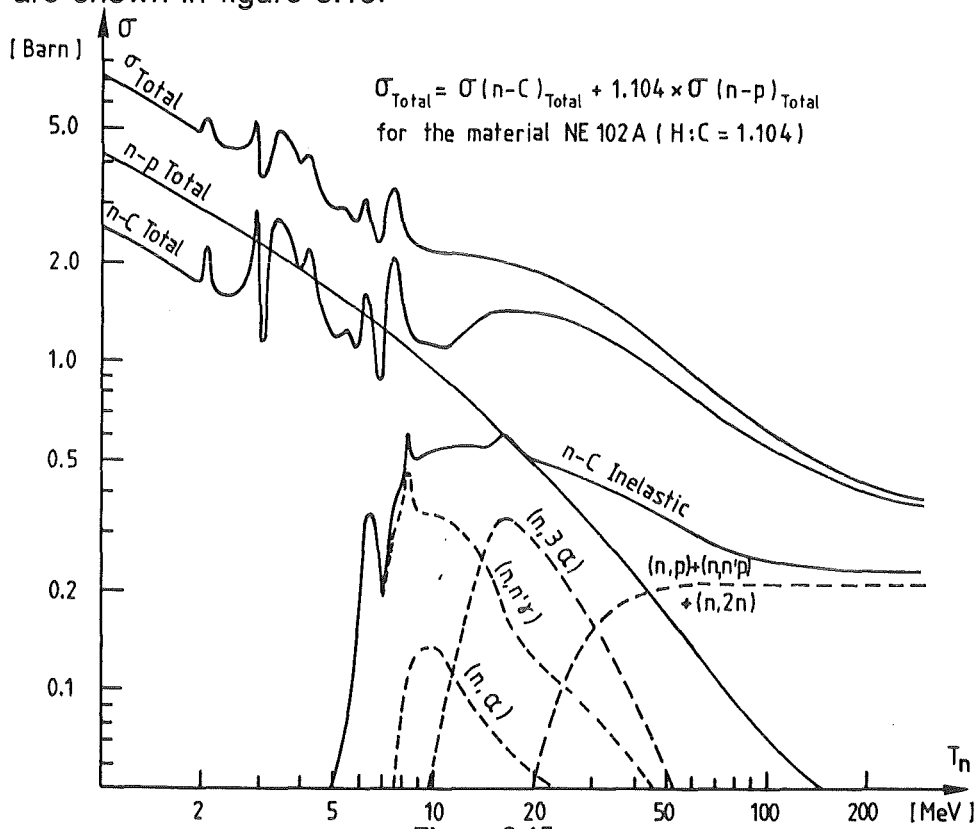


Figure 3.15. Cross sections for neutron induced reaction processes in NE102A. The data is taken from [89]

The light output and therefore the pulse height from an organic scintillation counter is known to be a linear function of the energy deposited by an electron above about 100keV. Since the light output produced in an organic scintillator by a more heavily ionizing particle such as a proton is smaller and not a linear function of the energy lost by the particle, it is necessary to calibrate the response of the scintillator as a function of the energy deposited by the particle.

Gooding & Pugh [83] used a semi-empirical formula [82] to calculate the light output, L_k , for the plastic scintillator NE102, as a function of the deposited energy, T_k , for different particles, k. Their data were in good agreement with experiments and were empirically parameterized by Kurz [84] in the following form:

$$L_k(T_k) = a_k T_k - b_k \{1.0 - \exp(-c_k T_k^{d_k})\} \quad (3.10)$$

with the inverse relation

$$T_k(L_k) = \hat{a}_k L_k + \hat{b}_k \{1.0 - \exp(-\hat{c}_k L_k^{\hat{d}_k})\} \quad (3.11)$$

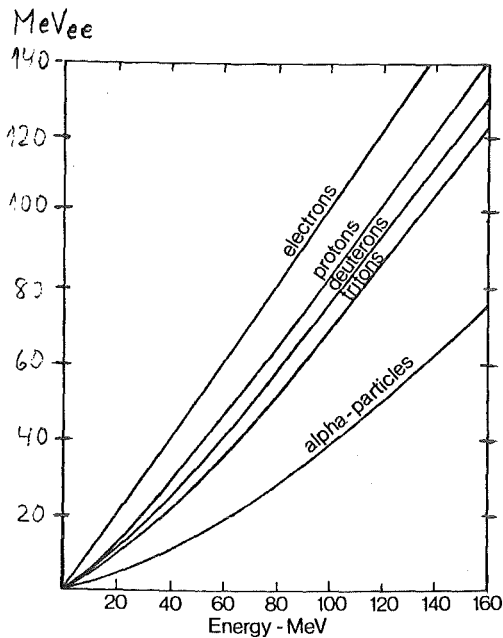
In our case L_k is given in units of the energy of an electron producing the same light output, so called electron equivalent units [MeV_{ee}]. It follows by definition that

$$L_e(T_e) = T_e$$

The light outputs, L_k , for different isotopes have the same functional form, being proportional to each other. The relation between the light outputs for a proton, a deuteron and a triton is

$$L_p : L_d : L_t = 1.0 : 0.925 : 0.872 \quad (3.12)$$

Therefore, only the coefficients for protons and for alpha particles are of interest. Figure 3.16 shows the light outputs, L_k , in NE102A as a function of the deposited energy, T_k . The parameters best fitting the experimental data for NE102A are given in table 3.3, [90].



k	a_k	b_k	c_k	d_k	\hat{a}_k	\hat{b}_k	\hat{c}_k	\hat{d}_k
proton	0.949	8.0	0.1	0.89	1.077	11.5	0.2	0.62
α	0.41	5.89	0.065	1.01	1.5	50.0	0.16	0.62

Table 3.3. Light output coefficients

Figure 3.16. The light output for various particles in NE102A

Since monoenergetic neutrons produce a broad pulse height spectrum with many small pulses the neutron detection efficiency strongly depends on the choice of threshold. At the time of the earliest efficiency calculations, notably the Kurz code (1964,[84]) and the Stanton code (1971,[85]), the cross sections for carbon break up by neutrons were not well known. The approach, therefore, was to adjust the cross sections used in the code so that the calculated efficiency fitted measured efficiency data. Because of this it was not possible to use the same code for a different type of counter (i.e. different C/H-ratio). In the Kurz code analytical expressions for the cross sections were adopted whereas in the Stanton code the propagation of the neutrons and its reaction products were traced and simulated by means of a Monte Carlo program. With more accurate cross section data available, Del Guerra (1976,[87]), it is now possible

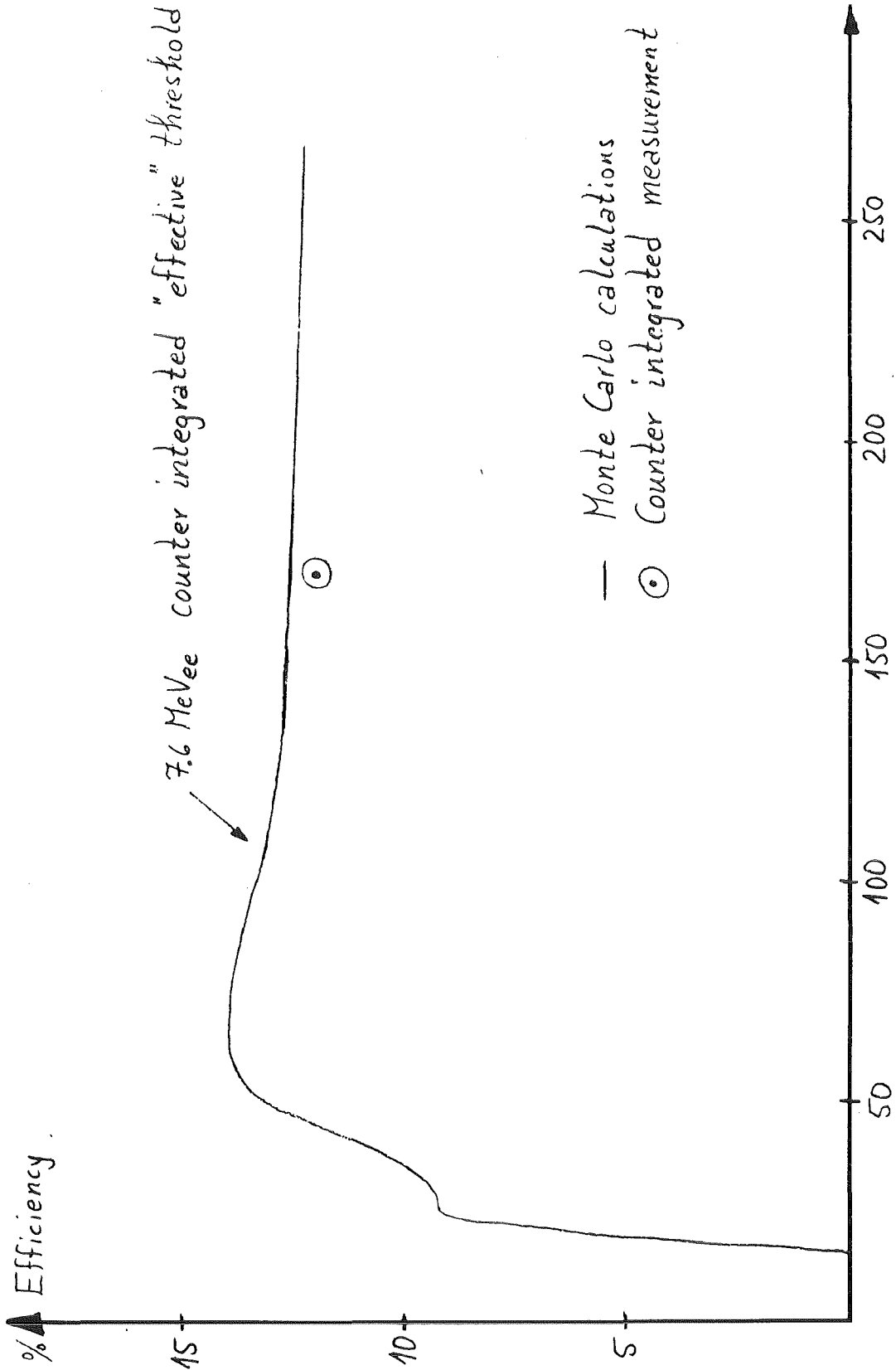


Figure 3.17. The efficiency of the new TOF-counter

to make absolute calculations of the neutron detection efficiency. The newest, most reliable, calculations done by Cecil (1979,[89]) and modified and applied by Cierjacks (1982,[90]) are complete Monte Carlo simulations using measured cross sections and better light response relations as well as incorporating relativistic kinematics and escape corrections. The upgraded Cecil code of Cierjacks also include optical separation between scintillators and effects due to different angle of incidence on the counter surface. Compared to the original Cecil code it uses up to date cross sections and improved light response relations. It has been found to agree with measurement up to 450MeV with an overall accuracy of better than 10%. The calculation does not include pion production which occurs above 350MeV and can be of importance at higher energies.

Figure 3.17. shows the efficiency for the new TOF-counter as calculated by the code of Cierjacks in comparison with a measured efficiency point. This point was measured with the associated particle method (see p.50 and [91]).

3.2.4.2 CONSTRUCTION

During our experiments we used two sets of TOF-counters which we will denote "old" and "new" according to their date of construction. The 2 old counters (N1,N2) have been used in previous experiments at CERN and SIN [1-6] and are thoroughly described elsewhere [1,3,6,]. Therefore, only the most important features will be mentioned here. The construction is shown schematically below.

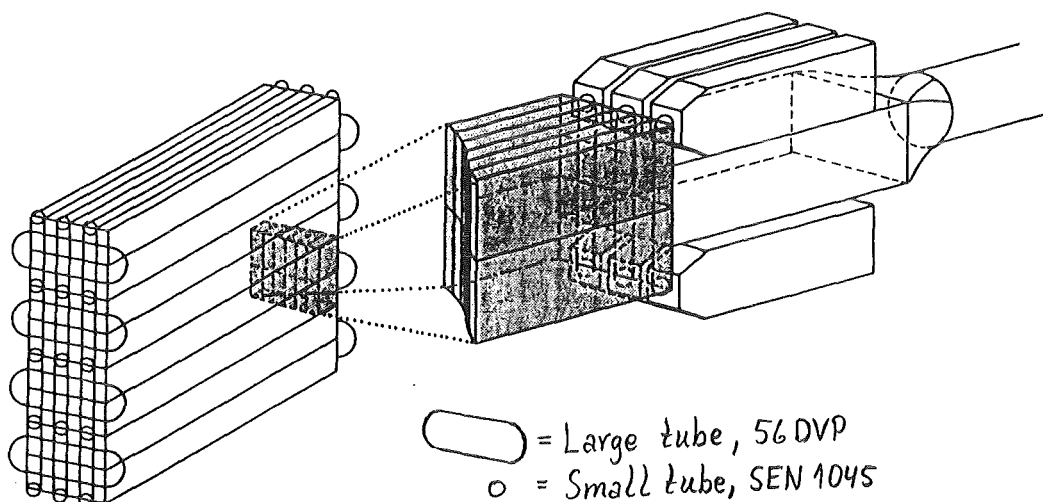


Figure 3.18. Layout of the old TOF-counters

The sensitive volume of each old TOF-counter is 2m long, 48cm high, 9cm thick. In order to determine the exact length of the neutron time-of-flight path, the counters are subdivided into eight layer of scintillator in height and six layer of scintillator in depth. In total they consist of 48 isolated rods (2m long, 6cm high, 1.5cm thick) made of NE110 plastic scintillator. A total of 30 small phototubes (4/3 inch, SEN1045) each attached to two rods (see figure 3.18.) shows the pattern of the rods that have given a signal for each event.

A pair of 2 inch 56DVP photomultipliers is optically coupled to each side of the bundle of 12 rods composing a module. The position information along the counter is taken from the time difference between these two photomultiplier signals. This time difference, the time-of-flight information taken between one side of the counter and the pion-signature signal, the pattern information from the small tubes, as well as the pulse height on both sides, are written on tape event by event. As light isolation $13\mu\text{m}$ aluminium foil and two layer of $180\mu\text{m}$ black PVC foil is wrapped around each rod.

Like the old counters, the new TOF-counter is subdivided into several bars. The main improvement is, however, that the pulse-height and time-of-flight information from each tube is available, rendering a separation into big and small tubes obsolete. The layout of the new TOF-counter is shown in figure 3.19.

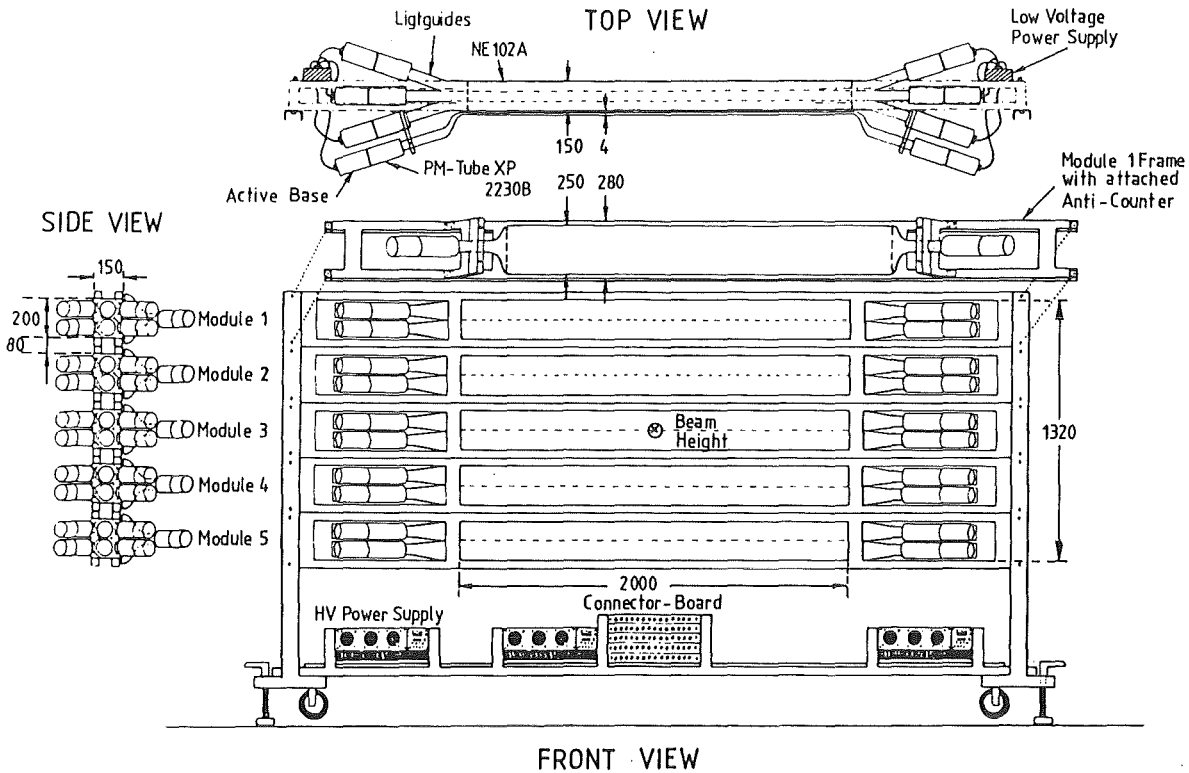


Figure 3.19. Layout of the new TOF-counter

The new counter consists primarily of 30 optically isolated NE102A plastic scintillator rods, each 2m long, 10 cm high and 5cm thick. The 30 rods are arranged in a 10×3 rod matrix to give a total counter size of $200 \times 132 \times 15 \text{cm}^3$ with an effective counter area of $200 \times 100 \text{cm}^2$ facing the incident particle beam. The total set of rods is grouped into five vertically separated modules consisting of six rods each with two layers in height and three layers in depth. While the optically separated rods are packed as closely as possible in each module, the different modules are separated by 8cm in height, in order to facilitate their mounting in a common counter rack. Two racks are available making it possible to construct two counters with an arbitrary combination of modules. A pair of

XP2230B photomultipliers is attached to each rod, i.e. altogether we have 60 big tubes providing information on pulse height and time-of-flight. We are employing bases with built-in 10X amplifier. These active bases also incorporate a pulse shaper for improved time resolution. 10 low voltage power supplies -- two for each module -- are attached to the counter rack. To cancel eventual ground problems a special ground connection was layed between the counter in the area and the subsequent electronics.

It is generally possible to distinguish charged particles from neutrons via the pulse height, time-of-flight relation. Only for the neutron events producing the highest pulses a separation from protons is not possible. Therefore mounted on the new TOF-counter, facing the target, we are employing a set of five ANTI-counters, one for each module. The ANTI-counters had to meet certain requirements:

- ☞ they had to be thin enough to have negligible efficiency for neutrons.
- ☞ they had to be thick enough to allow for approximately 100% efficiency for charged particles.

The ANTI-counters were chosen to be 210cm long, 15cm high and 4mm thick.

3.2.5 THE CHARGED PARTICLE DETECTOR

3.2.5.1 GENERAL LAYOUT

The task of this detector arm is to determine the trajectory, the kinetic energy, the mass and the reaction point in the target of the charged particle. The general layout is shown in figure 3.20.

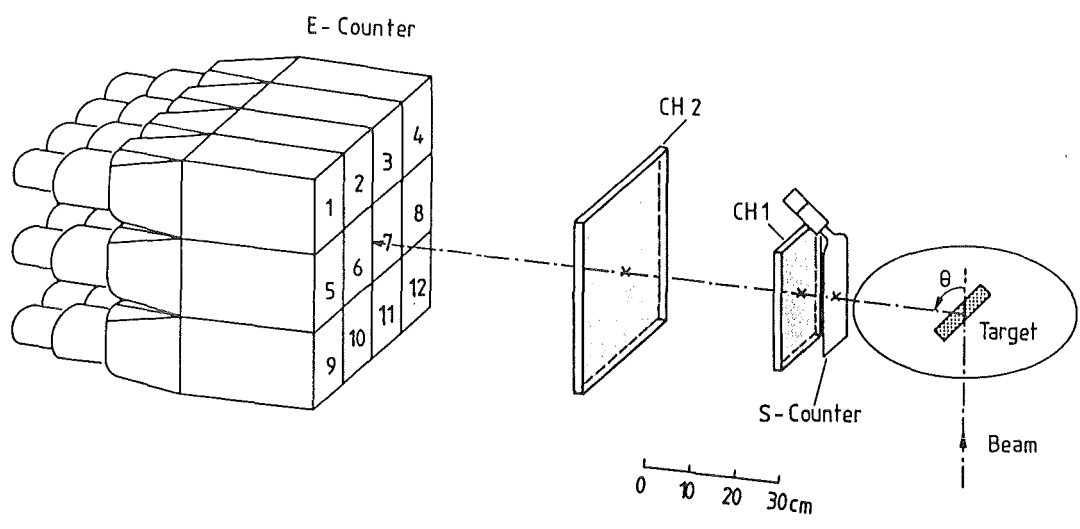


Figure 3.20. Layout of the charged particle detector arm

Starting from the target the particles first pass through the thin S-counter, (1mm, $17 \times 25 \text{cm}^2$), two multi-wire proportional (MWP) chambers with 3 planes each and finally get absorbed in the E-counter. The purpose of the S-counter is to suppress the neutrons and the particles not originating in the target. It is the S-counter which defines the solid angle. The whole system is mounted on the same support. To facilitate a change in detector position, this support can be turned around a point below the target so that the detector is always directed towards the target.

3.2.5.2 THE E-COUNTER

The E-counter consists of a 4×3 array of identical modules of the material NE102A, each with a front face of $17 \times 17 \text{cm}^2$ and a depth of 30cm, see figure 3.21.

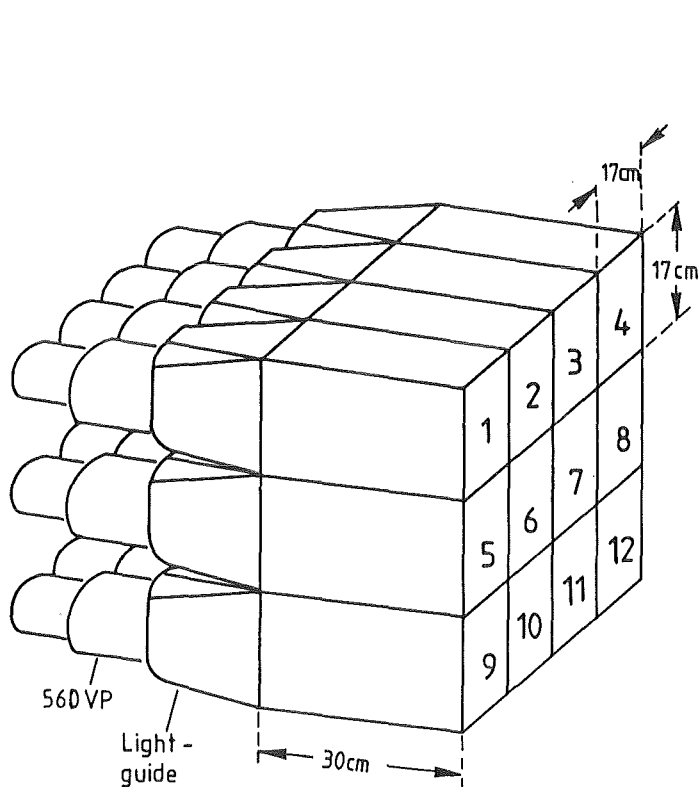


Figure 3.21.
Layout of the E-counter.

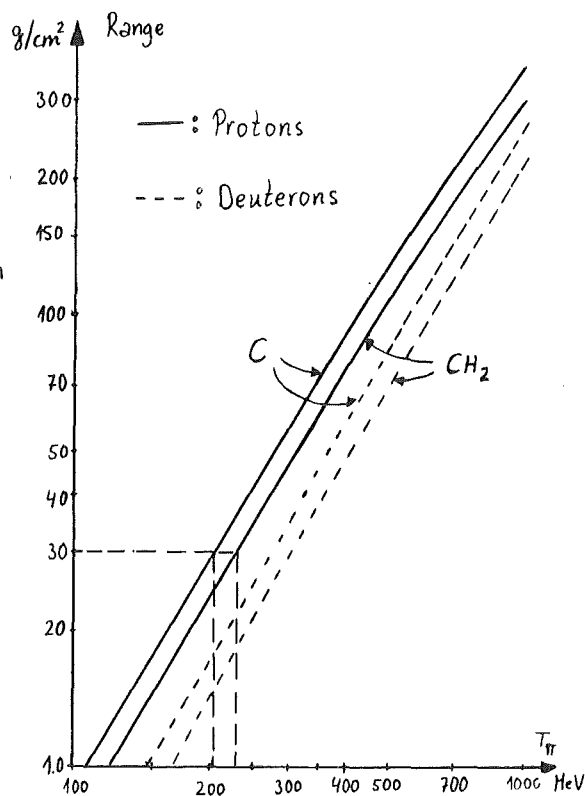


Figure 3.22.
Range of protons in matter [93].

A depth of 30cm is sufficient to stop protons of 200MeV. See figure 3.22. As light isolation $13 \mu\text{m}$ aluminium foil and on the side faces also two layer of $180 \mu\text{m}$ black PVC foil are applied. We use XP2041 photomultipliers.

3.2.5.3 THE MWP-CHAMBERS

The purpose of the chambers are to determine the trajectories of the charged particles. In the FSI region two particles pass through a chamber at the same time. To be able to unambiguously determine the trajectory points of the particles in such a case, each chamber consists of three planes. The third plane removes, for each chamber, the 2-fold ambiguity of the other two planes, see figure 3.23.

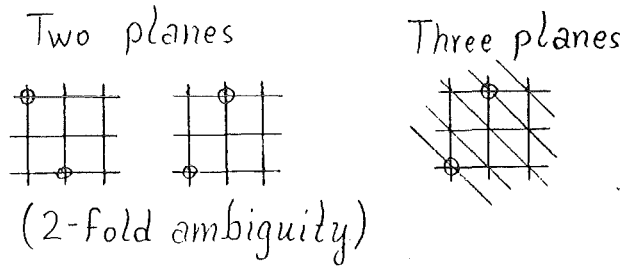


Figure 3.23. Ambiguity in one chamber

The two chambers thus determine 4 points of the two trajectories which in principle leaves another 2-fold ambiguity for the whole system. Since the trajectories have to originate in the target, this ambiguity can be resolved in nearly all practical cases. The configuration is shown in figure 3.24.

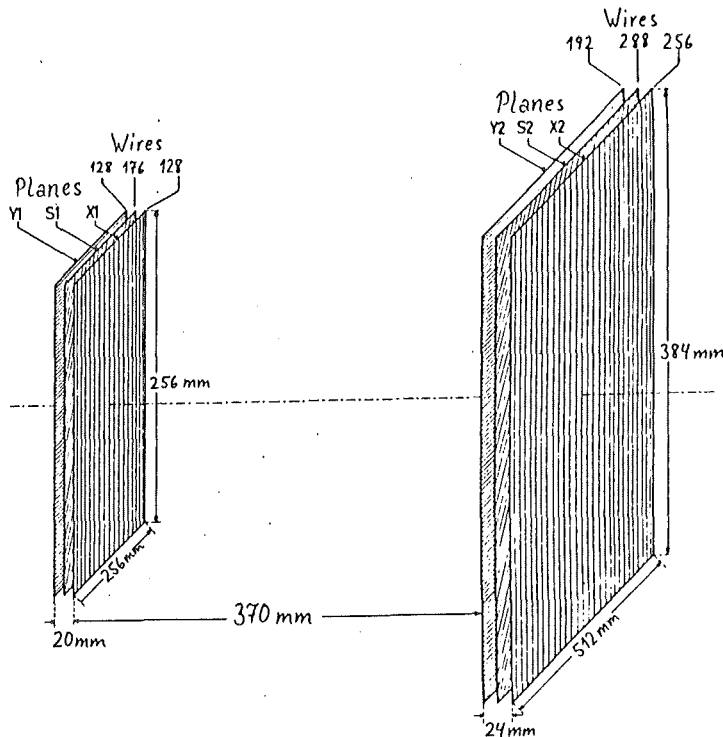


Figure 3.24. Layout of the chamber system

The number of wires of each plane is shown in figure 3.24. The wires are $20\mu\text{m}$ thick and the distance between them is 2mm. On both sides of an acquisition plane, at a distance of 6mm, is a high voltage wire net with a wire spacing of 1mm and an applied voltage of 4.1keV. The front and back surface of the chambers are covered by $50\mu\text{m}$ mylar foil. A mixture of 60% Argon, 37%

Isobuthane and 3% Methylal is used for the counter gas. The gas continuously flows through the chambers so that the whole gas volume is exchanged every 2 hours.

We use the chambers in the proportionality region, with small pulses, about $10\mu A$. The electronic cards are attached to the frame supporting the wires. Each card processes the signals from eight wires. The electronics is described in section 3.3.4.

Before every measurement the chambers are tested with a strontium- β source attached to the S-counter. Then the HV is adjusted so that all electrons reaching the E-counter are detected. Since the electrons are minimal ionizing particles we are assured that all protons and heavier particles will be detected.

3.2.6. THE EXPERIMENTAL SET-UP

The experiments presented here were performed during two periods of five weeks. During the first period of October 1982, the new TOF-counter, with all its implied changes in electronics and on-line program, was not ready to be used. We therefore had to resort to the old TOF-counter N I and N II. Figure 3.25. shows the set-up.

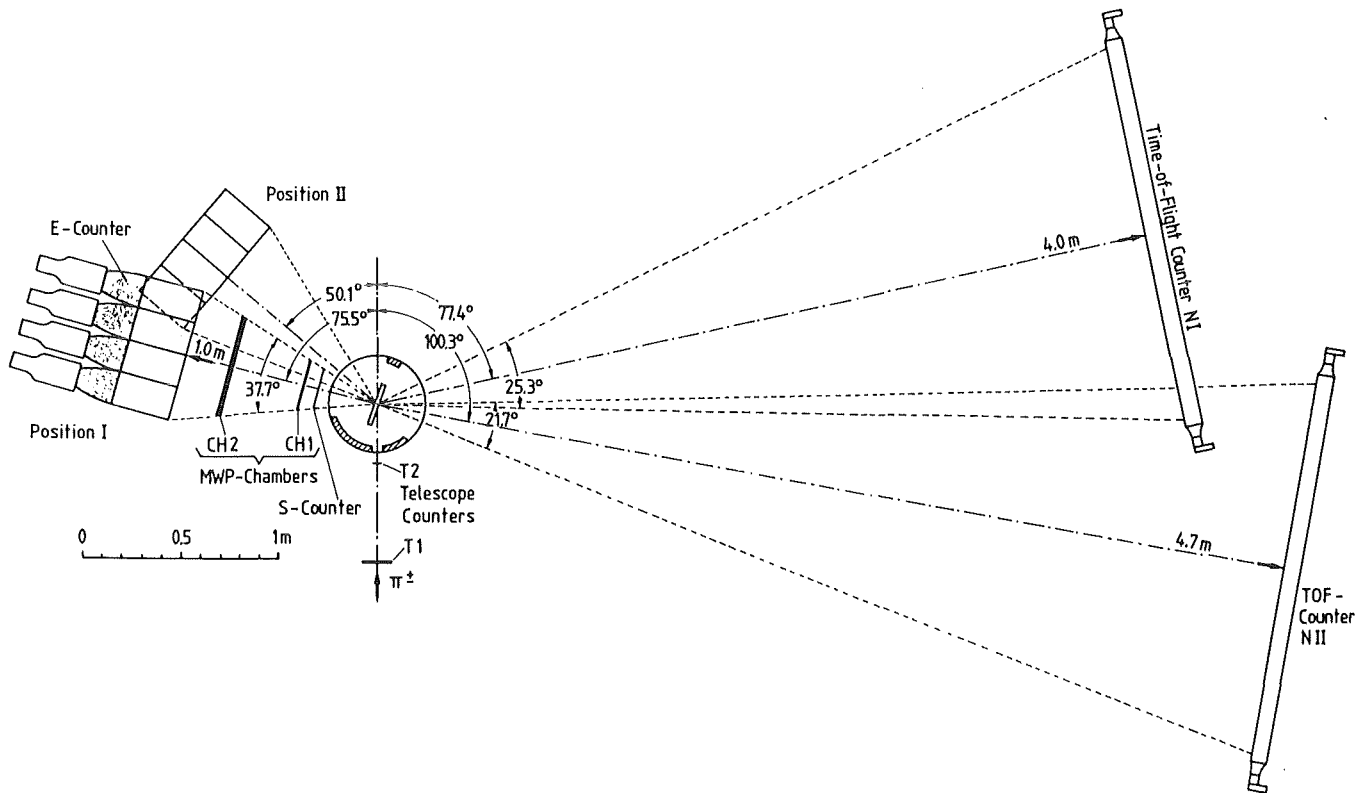


Figure 3.25. Set-ups of October 1982

Since we are mainly interested in quasifree absorption we would like to position the counters optimally for detection of such events. If we fix the angle between the incident pion and one detected nucleon, e.g. by selecting one module of the E-counter, for quasifree events the correlated nucleon has a specific angle relative to the beam direction. This angle which corresponds to the free $\pi d \rightarrow NN$ kinematics will be called the quasi-deuteron angle. Some references also call this the conjugate angle [40,79]. We will henceforth assign the fixed angle to the E-counter and talk about the corresponding quasi-deuteron angle in the TOF-counter. Figure 3.26 shows the relation between the two angles for different pion momenta.

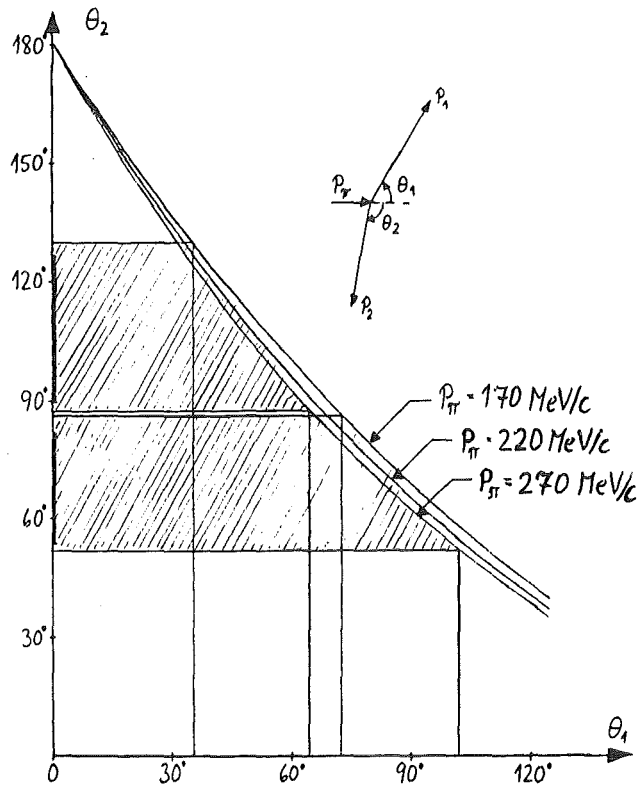
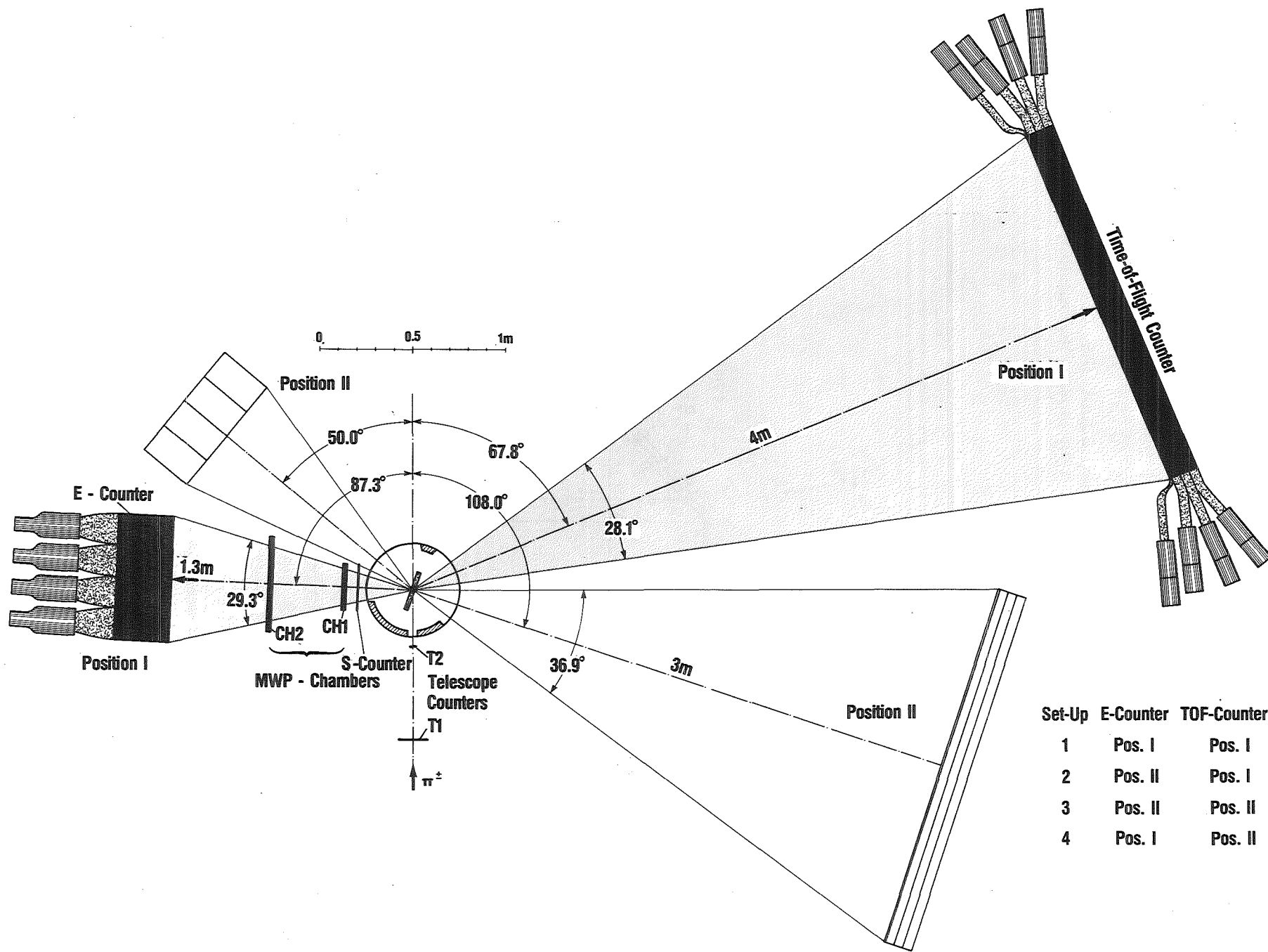


Figure 3.26. The Quasi-Deuteron Angle

Figure 3.27 shows the set-ups of June/July 1983. In figure 3.26, the quasi-deuteron angles corresponding to position I and II of the E-counter is shaded. It is seen that in set-up 1 and 3 the counters are positioned under the quasi-deuteron angles whereas in set-up 2 and 4 other angles 30° off these are covered.



Set-Up	E-Counter	TOF-Counter
1	Pos. I	Pos. I
2	Pos. II	Pos. I
3	Pos. II	Pos. II
4	Pos. I	Pos. II

Figure 3.27. The set-ups of June/July 1983

3.3 THE ELECTRONICS

3.3.1. GENERAL PURPOSE

The electronics links the counters with the computer, a PDP 11/40 for data acquisition. It selects and prepares the data. The electronic units can be divided into 2 groups with regard to the way they interact with the computer. The first group communicates directly with the computer via a data-bus, CAMAC modules. The second group merely selects events (trigger) and transforms data. These are the NIM modules.

The electronics, which to the largest part consists of fast NIM modules, is accommodated in 8 racks in a barrack outside of the π E1-area.

The main tasks of the electronics are:

- ☞ To select special events (trigger)
- ☞ To write information on these events on tape
- ☞ To write information about rates on tape
- ☞ To perform tests (§4.1& §4.2)
- ☞ To calibrate the equipment (§4.4)

Figure 3.28 shows the concept of the electronics selecting the data to be conveyed on tape.

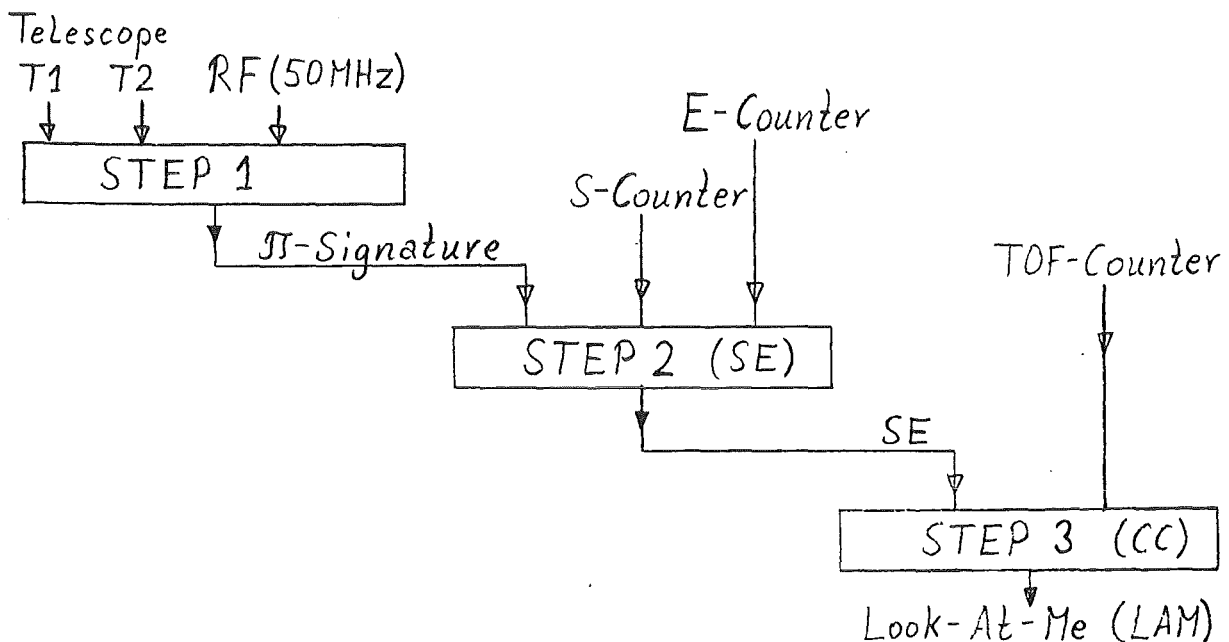


Figure 3.28. The concept of the electronics

The real events are selected in a three step procedure:

- ☞ *STEP 1: In the telescope electronics §3.3.2. the incident pions are selected by using their fixed time relation to the RF. The resulting signal will be called π -signature.*
- ☞ *STEP 2: The E- and S- counter are located closer to the target than the TOF-counter and will in general respond faster to an event. We, therefore, first require a coincidence between signals from these two counters and the π -signature. This so called SE-coincidence is treated in §3.3.5.*
- ☞ *STEP 3: In this step we take the TOF-counter into account. Each module of the TOF-counter is separately taken in coincidence with the SE-signal in the so called TOFi-coincidence (i =number of module). By occurrence of such a coincidence a look-at-me signal for the computer is issued and the data is conveyed on tape.*

To obtain good energy resolution by means of the time-of-flight measurement, the TOF-counter is located at a distance of about 4m from the target. Hence, to allow for detection of 10MeV neutrons, and speed-of-light particles, the time window in the TOFi-coincidence must be 150ns. By opening this coincidence only in cases of a detected particle in the charged particle detector arm (SE) we are able to minimize the possibility for chance coincidences.

So far we have only considered cases where one of the emitted particles is charged and can be detected in the charged particle detector arm. If we desire to measure nn-coincidences we need to make some minor modifications. This case is treated in §3.3.9.

In this experiment we are employing a set of 4 CAMAC crates which are connected through interfaces (JCC 11, Schlumberger) to the same data-bus allowing for exchange of information. These 4 crates contain analogue-to-digital converters (ADC's), time-to-digital converters (TDC's), pattern-units (PU's), scalers, In-Out units which are allowing for a bi-directional communication with the computer, and the JCF 10 (Schlumberger), the interface between the MWP-chambers and the computer.

Opposite in figure 3.29 a block diagram of the complete electronics can be seen. The symbols used together with a rudimentary description can be found in appendix A.

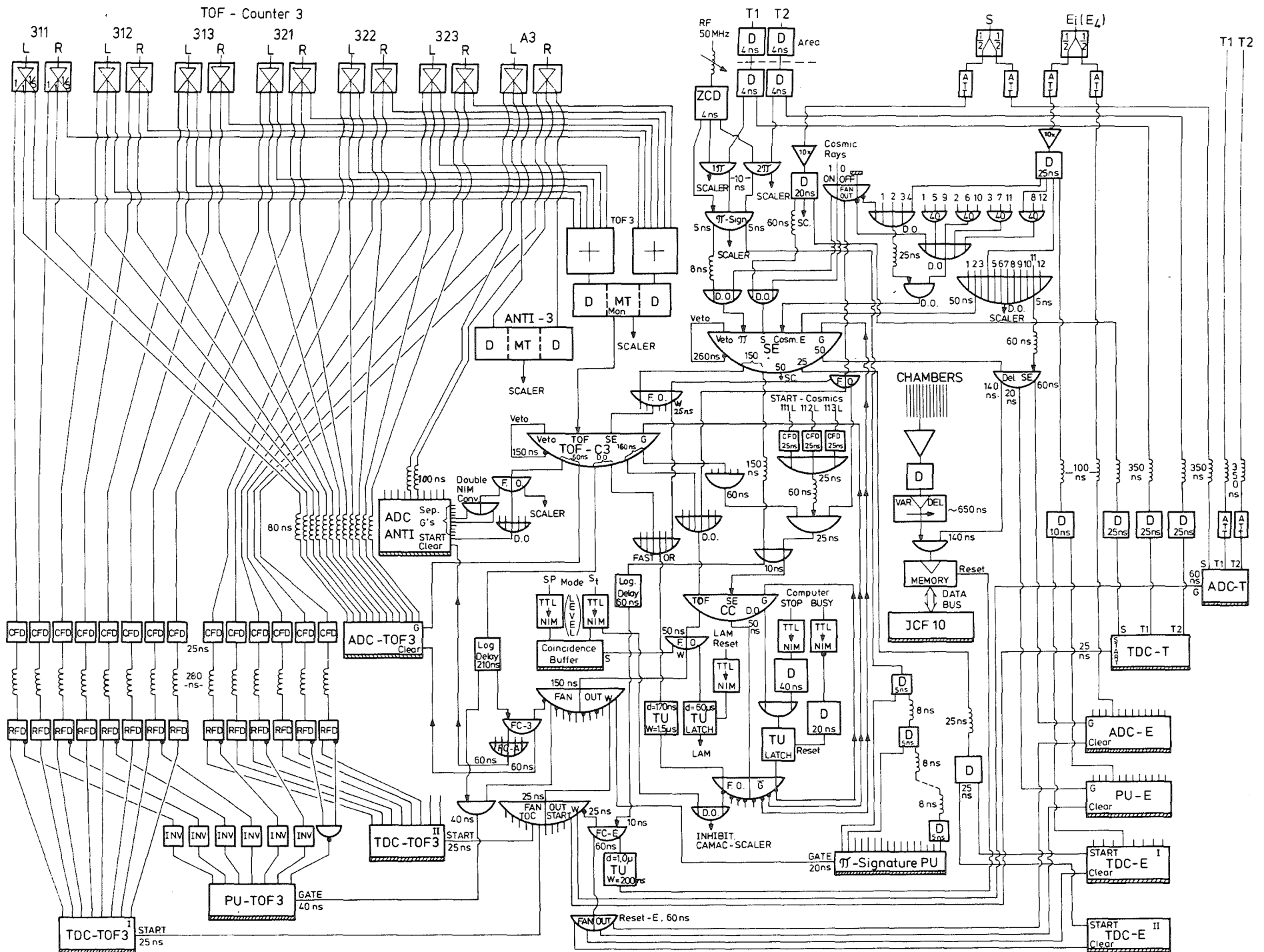


Figure 3.29. The complete electronics

3.3.2. THE TELESCOPE LOGIC

- Purpose:**
- To produce a signal whenever a pion hits the target.
 - To inspect the vicinity-in-time of this signal.
 - To measure the counting rates.

The realization is shown in the schematic diagram opposite (figure 3.30b.). The pions are selected (cf. §3.2.2.) via coincidence with the RF signal in the 1π - and 2π -coincidences. The output signals are now taken in coincidence with each other in order to define the beam and reduce the background. Since both signals exhibit time fluctuations of 4ns (relative to RF) which is mostly due to "time walk" of the discriminators (cf. appendix A), we are impressing the timing of the RF on the π -signature coincidence. Figure 3.30a shows the time relations of the different signals preceding a π -signature coincidence.

The telescope rates as well as the coincidence rates are written on the CAMAC scalars (cf. §3.3.6.). The 2π -coincidence is used as beam monitor for the determination of the absolute pion rate (cf. §3.2.3).

The π -signature signal together with the signals from the charged particle detector arm and the time-of-flight counter ultimately leads to the so called central-coincidence, CC, which causes the registration of an event. The pulse height and the time information of the telescope signals which lead to the registered event are fed into an ADC and a TDC respectively. The gate for the ADC and the TDC-start are thereby taken from the CC signal which has the timing of the RF.

The width of the CC is comparatively large due to the large differences in time-of-flight to the TOF-counter. Several pions could, therefore, have produced the event. If, in a range which could lead to ambiguity a second pion is detected it is registered by means of the π -signature PU. The gate of this unit is a 10ns wide CC signal and the inputs are the output of the π -signature coincidence inspected in intervals of 20ns. See figure 3.30b. In the off-line data evaluation events with no unambiguous assignment can thus be rejected. The bit in the PU corresponding to the π -signature coincidence leading to -- and impressing the timing on -- the CC is always present. The abundance of other bits is an indication of possible chance coincidences.

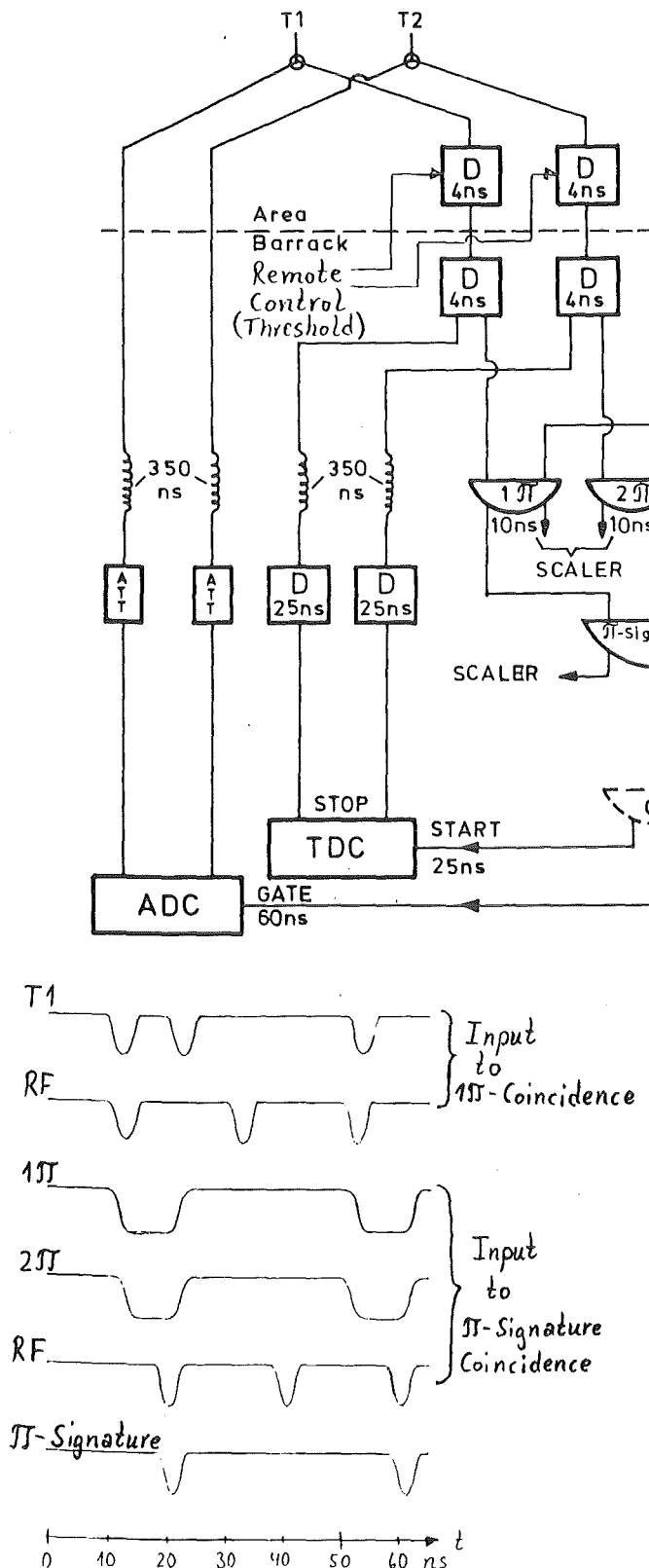


Figure 3.30a.
Time relation of signals

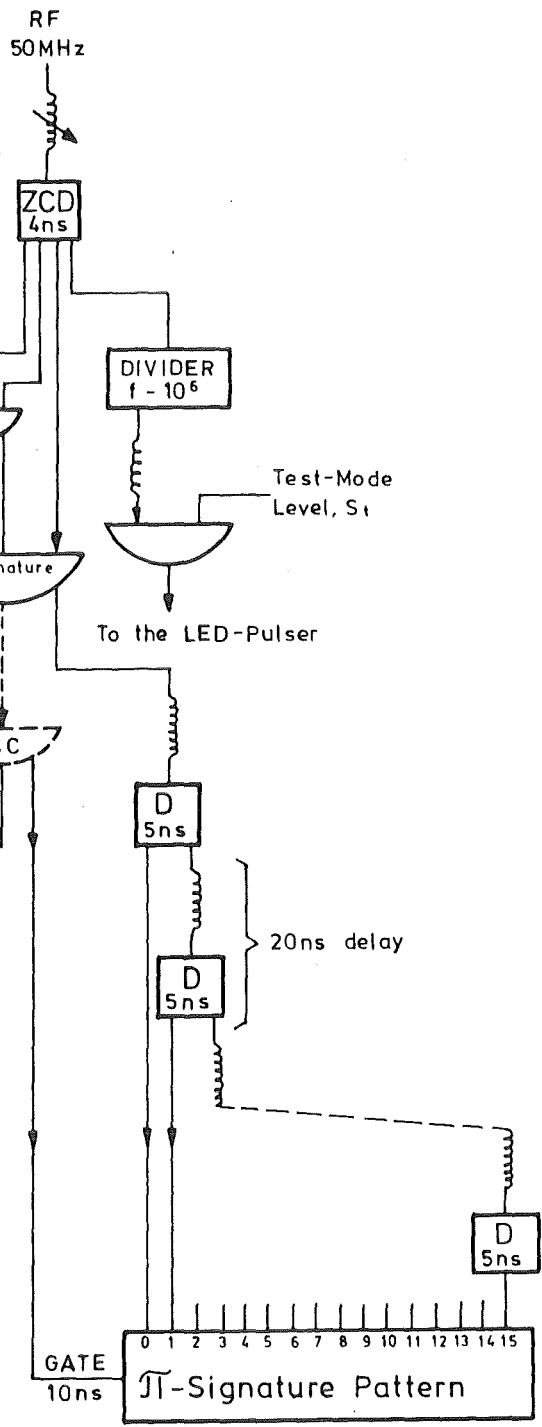


Figure 3.30b.
The telescope logic

3.3.3 THE E-COUNTER ELECTRONICS

- Purpose:**
- To produce a signal, SE, if a charged particle arrives at the E-counter within 50ns after the pion entered the target.
 - To determine pulse height and time-of-flight of this particle in case of a registered event.
 - To determine the counting rates.

A blockdiagram of the electronics for the E-counter is drawn in figure 3.31. A pion reacts in the target with the subsequent emission of a charged particle which is detected in the charge particle detector arm. This particle produces, in turn, a signal in the S-counter and in one of the E-counter modules (E1-E12). These signals together with a short π -signature signal for determining the timing are fed into the SE-coincidence. The width of the signals allow for prompt events ($\beta=1$) as well as the low-energetic events which barely pass the detector threshold. The actual coincidence widths at the input of the SE-coincidence are shown below.

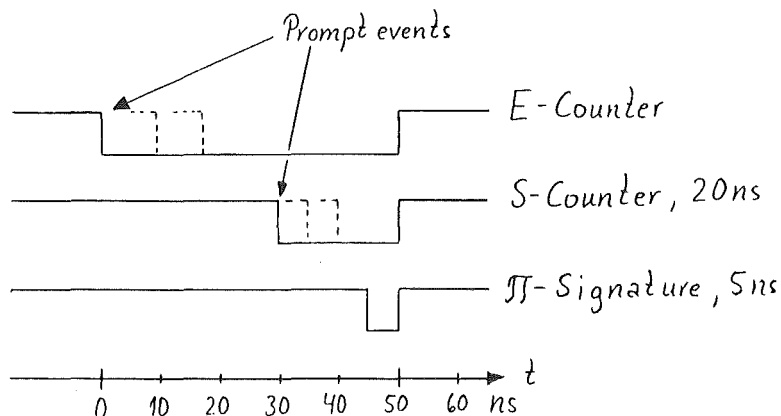


Figure 3.32. Signal widths at input of the SE-coincidence.

The SE-coincidence is also gated by the so called "G-response" assuring that events are only accepted when the computer and the electronics is ready, cf. §3.3.8. Since the SE signal has the timing of the pion it is used as common start of the TDC's. While obtaining the energy from the pulse height spectra, the accuracy of the time-of-flight information of the E-counter has lower priority. The TDC information is merely used to separate different particles by means of the 2-dimensional TOF vs. pulse height spectra (cf. §5.2.1.). We are thus employing usual leading-edge discriminators (cf. appendix A).

Since the discriminators ought to determine the energy threshold, it is essential that no events above threshold be rejected by a too narrow coincidence window. In figure 3.33 the time-of-flight to the E-counter versus the proton energy in the target and that of the proton upon arriving in the E-counter is shown for the set-up of summer 1983 (see figure 3.27).

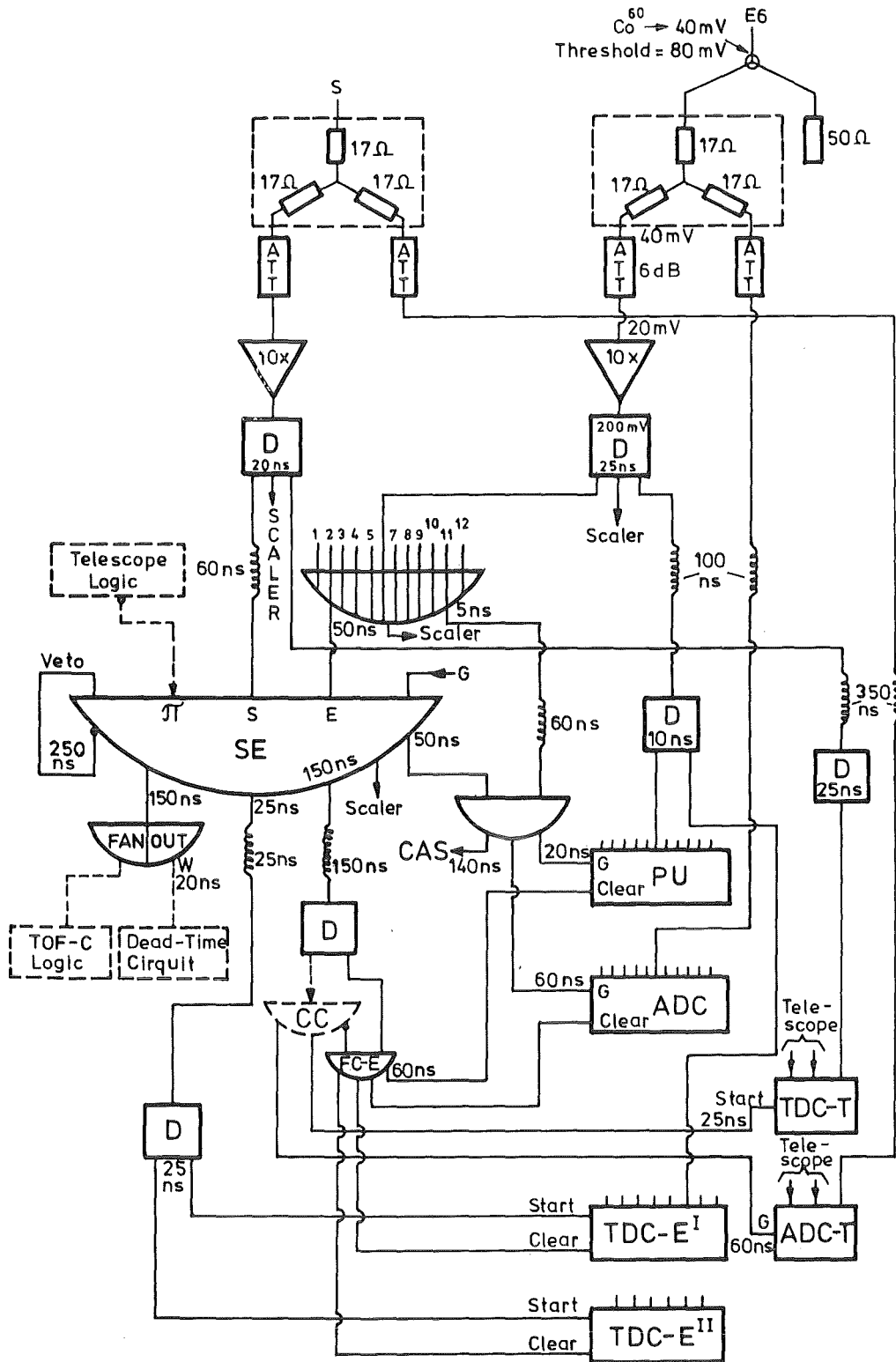


Figure 3.31. The E-counter electronics

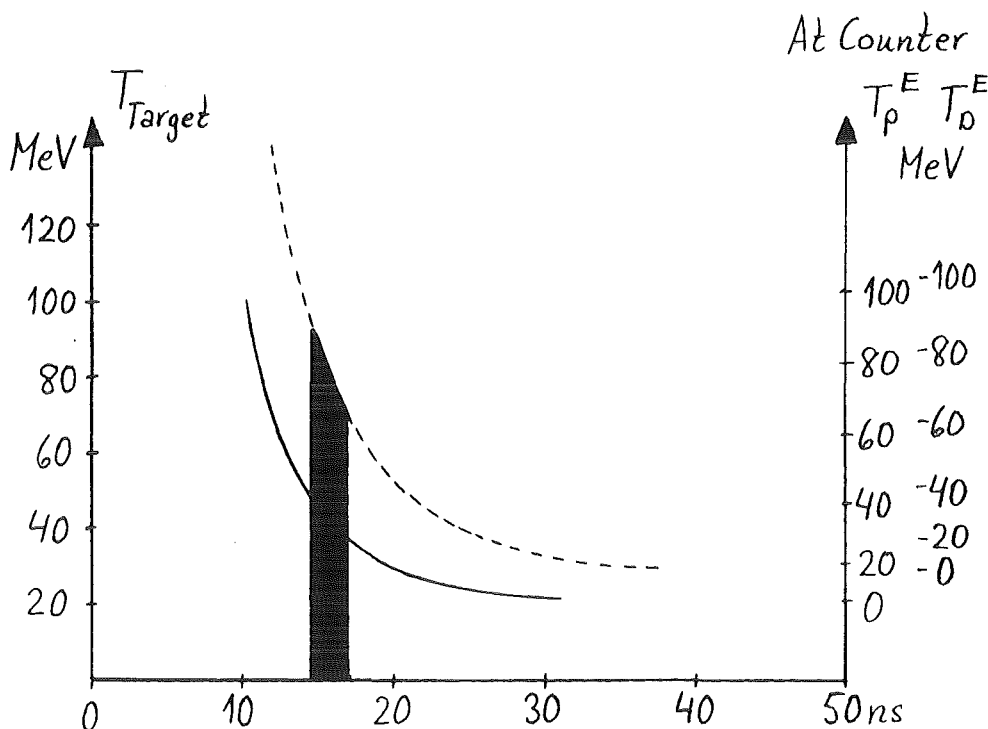


Figure 3.33. Time-of-Flight vs. Energy for the E-counter (distance: 1.3m)

The threshold was adjusted with a Co^{60} source to twice its Compton-edge ($2 \times 0.93 \text{ MeV}_{ee} \approx 5 \text{ MeV}$ proton energy). This corresponds to a time-of-flight to the E-counter of 40ns.

For a special measurement, namely the determination of the neutron detection efficiency of the TOF-counter, particle separation for the E-counter was made by hardware, i.e. via timing in the SE-coincidence. The efficiency was determined with the associated particle method: for one specific angle relative to the beam axis, i.e. for one segment of the E-counter, the deuterons, and hence the associated neutrons hitting the TOF-counter, are monoenergetic. Thus, by determining the number of deuterons and counting coincident neutrons we can determine the efficiency for the corresponding neutron energy -- for different segments of the E-counter the energy is different. In order to minimize the required measuring time it is necessary to separate the protons so as to only record the deuterons. This can be accomplished by setting windows in the pulse height spectra and the time-of-flight spectra. The technique of selecting particles through a coincidence is shown in figure 3.34.

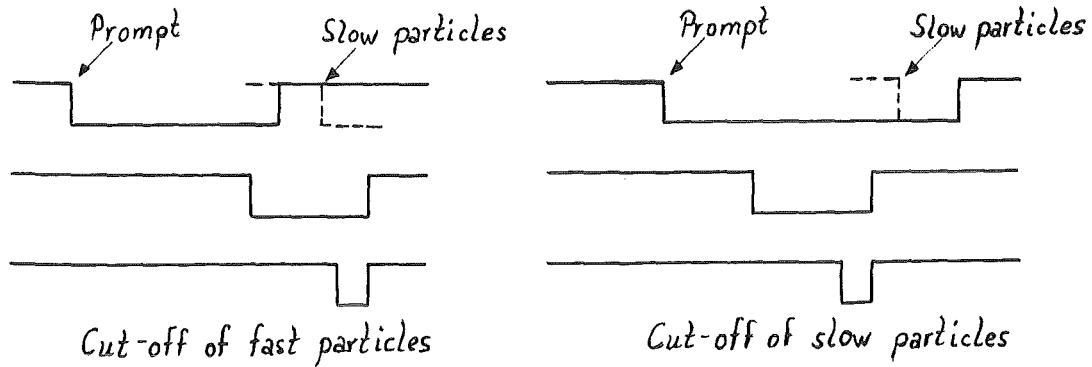


Figure 3.34. Selecting particles via timing

By reducing the width of the E-signal -- without changing the timing -- the fastest particles are eliminated whereas by delaying the E-signal the slowest particles are cut off.

In figure 3.33. the window accepting all possible deuteron energies for position I of the E-counter (see layout figure 3.27.) is shaded.

The output of the SE-coincidence has the timing of the pion. However, to be able to use as narrow gates as possible for the ADC's and PU's, a gate signal with the timing of the event in the counter is needed. This is achieved by means of a delayed SE-coincidence, where the E-counter is determining the timing. The gate for the PU's can thus be made as short as 20ns. Since the selective read-out of the ADC and TDC requires the existence of a bit in the corresponding PU, this gate width is of special importance: if the signal does not match the gate all the E-counter information is lost. The gate for the ADC's is 60ns and the TDC range is 100ns. In case of the non-occurrence of a CC-coincidence the information stored in the ADC's, TDC's and PU's is cleared. See § 3.3.7.

3.3.4. THE CHAMBER-ACQUISITION-SYSTEM, CAS

Purpose: To store information about responding wires in case of a SE-coincidence.

To be able to test the CAS by means of a simple procedure.

In figure 3.35. a blockdiagram of the electronics for the *Chamber-Acquisition-System* and the time chart of the signals are shown. The very small signals from the wires of about $10\mu\text{A}$ and a duration of 200-250ns are fed into a MOS-stage of $5\text{k}\Omega$ input impedance. It includes an amplifier and a discriminator with variable threshold followed by a monoflop used to detain the signal until the electronics in the barrack has decided whether the event shall be registered or not. Normally this takes 650ns.

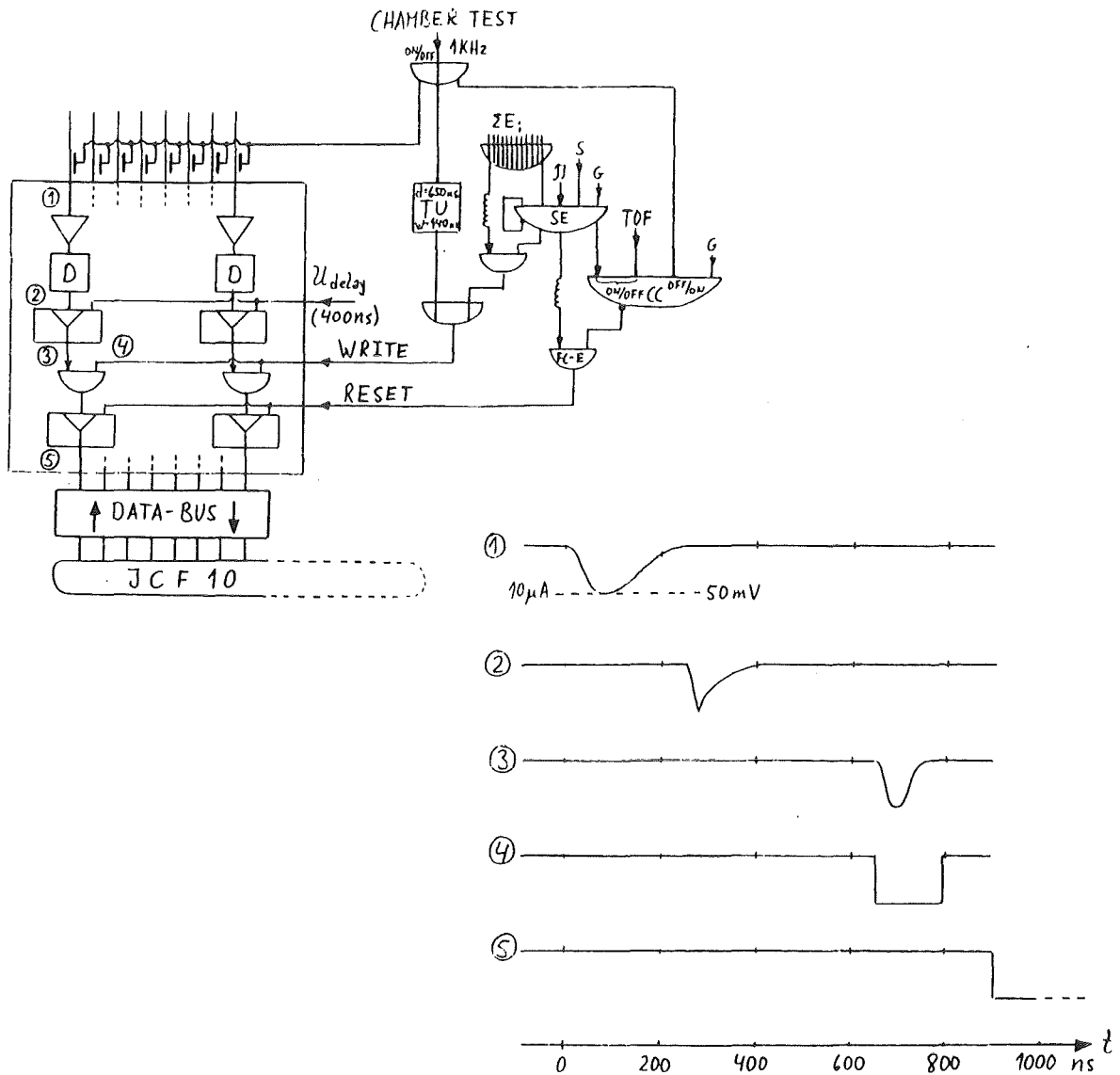


Figure 3.35. The electronics for the CAS and time chart of signals

An output of the delayed-SE coincidence is used as so called write signal and it causes the second monoflop to store the signal. Because of time walk (.cf §5.2.4.) and propagation delay the write signal must have a duration of 140ns. The information is stored in the monoflop till either it is read, i.e. transferred to CAMAC (JCF10, Schlumberger), or a reset signal arrives. The reset signal occurs when subsequent to the SE-signal no CC appears.

A test circuit is capacitively coupled to all wires in order to facilitate a test of the CAS. The test signal which fires the wires is also used as a write signal. To compensate for the delay in the chamber electronics this write signal is delayed 650ns in a timing unit. The test signal is also fed into the CC and a LAM is created. Hence, the only modification necessary to do a chamber test is to switch on the chamber test input of the CC and turn off the inputs of the counters in the CC. Usually a test frequency of 1kHz is used.

3.3.5. THE TOF-COUNTER LOGIC & THE CENTRAL COINCIDENCE

- Purpose:**
- To produce a central coincidence, CC, if a particle arrives at the TOF-counter within 150ns after the pion entered the target and a SE-coincidence has occurred.
 - To determine pulse height and time-of-flight of this particle.
 - To measure the counting rates.

The realization is shown in the block diagram of figure 3.36. The analogue signals of the PM tubes of the TOF-counter are transmitted through low dissipative cables to the electronics in the barrack. The maximal signal amplitude from the active bases of 5V reduces nevertheless in the course of the transmission to 3V. To obtain pulse height and time-of-flight information as well as a signal for the trigger logic we are using a split with three outputs. A corresponding passive device is however not feasible since in that case only 1/3 of the range of the charge-sensitive ADC's (256pC into 50Ω) can be exploited. Therefore we are using an active split, the outputs of which can be attenuated to facilitate a change of threshold or range of ADC. The six analogue signals from the PM tubes on one side of a module are added together by means of linear fan-in. The triggering threshold is determined by the subsequent discriminator and the so obtained logical signals from the left and right side of a module are fed into a so called mean-timer. In this unit the arithmetical mean-time, $(t_L + t_R)/2 = t_L + (t_R - t_L)/2$, is formed from the time of arrival of the two signals. Under the assumption of a constant light propagation velocity throughout the counter and neglecting time walk effects a signal is produced which is independent of position of impact (see figure 3.37).

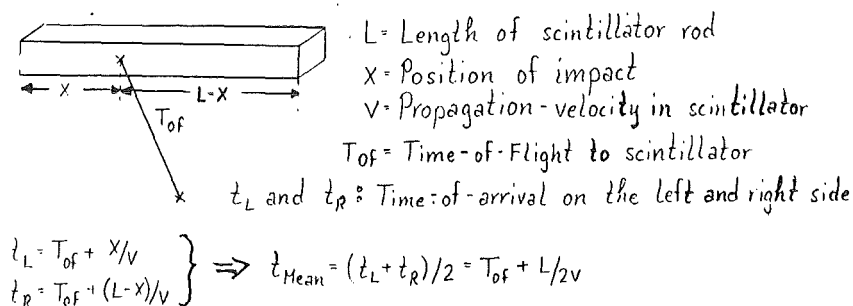


Figure 3.37 The principle of a mean-timer

The range of the mean-timer is 26ns allowing for the lightpropagation from one side of the counter to the other, cf. § 4.2.

The time-of-flight is a direct measure of the particle velocity i.e. for a specific particle the associated momentum. Unfortunately the time walk of the discriminators can not be neglected when determining the time-of-flight. For minimal walk we used constant-fraction discriminators, CFD's, for the TDC's (cf. appendix A). Still however walk corrections have to be applied in the off-line analysis (cf. § 5.2.4.). For the fast-trigger the timing is not crucial and usual leading-edge discriminators are employed giving a walk of 4ns. However, position dependent timedifferences, 14ns, are compensated for in the mean-timer, MT, mentioned earlier.

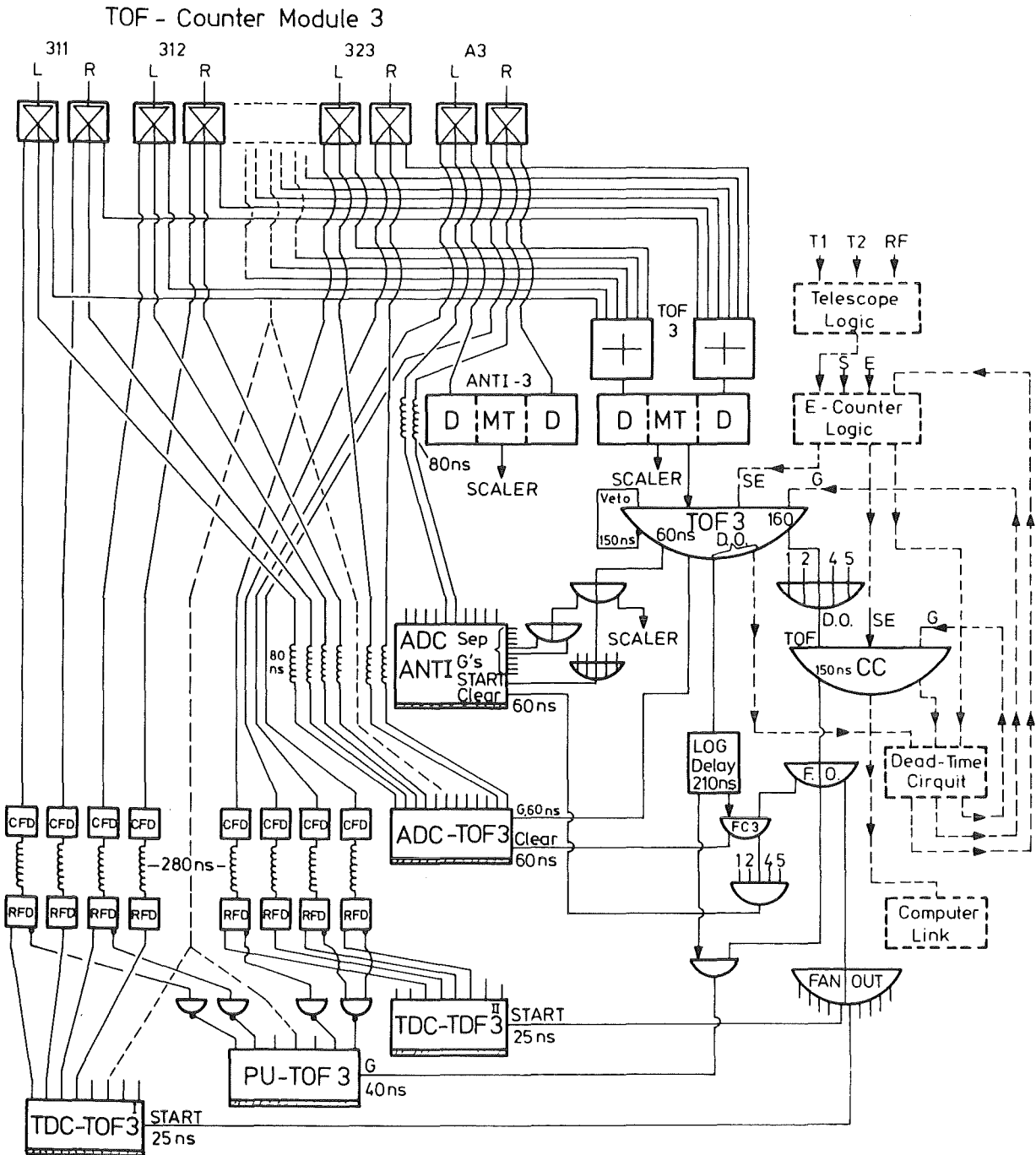


Figure 3.36. The TOF-counter Logic

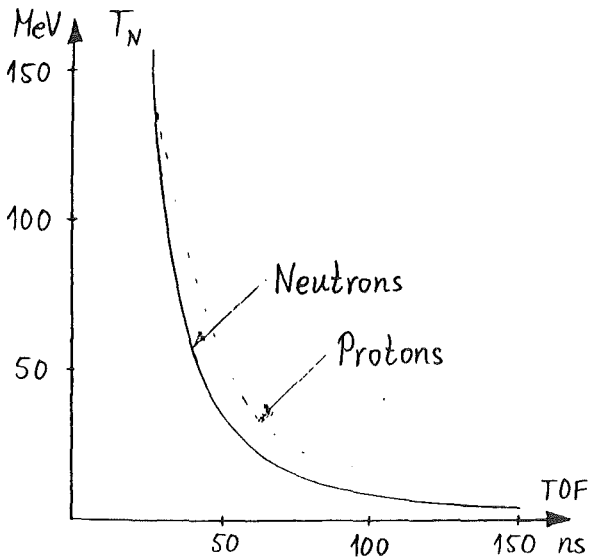


Figure 3.38. Energy vs. Time-of-flight to TOF-counter (distance $\approx 4\text{m}$).

To allow for detection of 10MeV neutrons, and speed-of-light particles, the time window in the TOFi-coincidence must be 150ns. It is determined by the length of the SE-signal. In figure 3.38. the kinetic energy of a neutron vs. the time-of-flight to the TOF-counter is drawn for position I of figure 3.27.

An output of the TOFi-coincidence with 60ns duration is used as gate for the ADC of module i (12-fold). The analogue signals are delayed to compensate for the delay in the fast-trigger electronics. This amounts to 80ns BNC cable delay. The ADC for the ANTI-counter has separate gates for all channels and requires an additional so called start signal to store the analogue information.

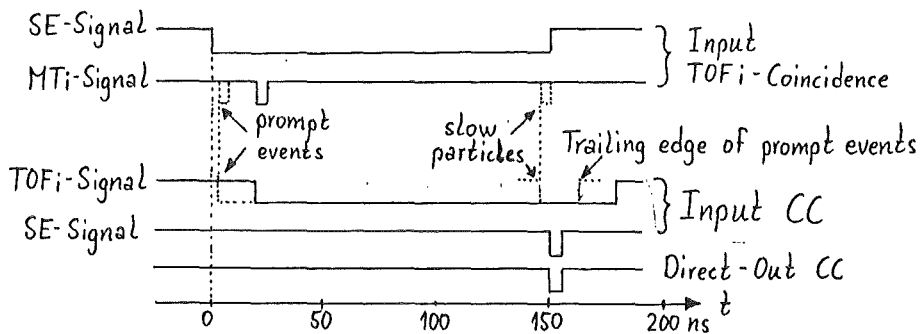


Figure 3.39. The time chart of the signals

In figure 3.39 the time chart of the signals is shown. The outputs of the TOFi-coincidence belonging to different modules are added by means of a fan-in and fed into the CC. Since the SE-coincidence and thus the RF determines the timing of the CC, the SE signal has to be short and the length of the TOF signal determines the coincidence width. In order to avoid rejecting events accepted by a TOFi-coincidence the TOF signal has a duration of 160ns. If an output of the CC occurs a Look-At-Me (LAM) signal for the computer is produced and the main coincidences are inhibited, \bar{G} , till the computer is ready for a new LAM-interrupt (see § 3.3.8.).

The gate for the PU's and the TDC start requires a CC-coincidence in contrast to the ADC's which are gated by the TOFi-coincidences. To be able to use as narrow a gate for the PU's as possible the short direct-out signal of the TOF-coincidence is delayed so that it in coincidence with a 150ns wide CC signal determines the timing. Since the output of the CC has the timing of the RF it TOF-coincidence is delayed so that it in coincidence with a 150ns wide CC signal determines the timing. Since the output of the CC has the timing of the RF it is used as common start for the TDC's.

The threshold of the CFD's has to be slightly lower than the threshold in the trigger producing discriminators. After delaying the logical signals to compensate for the delay in the trigger-logic (280ns Lemo cable) the signals are refreshed by means of a refreshing discriminator, RFD. Since these units have only one non-inverting output we are employing a pulse transformer to invert the signals for the PU. As the fast trigger, i.e. the gate of the PU, requires a signal from both sides of a rod it is sufficient to have the pattern information of the left side on tape.

The information of the ANTI-counter is not considered in the fast trigger but is written on tape and can be taken into consideration in the on-line as well as the off-line evaluation. Since a bit in the PU is required if the corresponding TDC and ADC information shall be conveyed on tape, (see §3.4.1.), a bit for the ANTI-counter is set if at least one side had a signal in coincidence with the TOF-counter.

3.3.6. THE SCALERS

- Purpose:** To write rates on tape (the CAMAC SCALERS).
 To monitor rates during the run (the MULTISCALER).

During the run rates are fed into the 36 CAMAC scalers and the Multiscaler. The contents of the first 6 CAMAC scalers are written on tape event by event whereas the remaining are read after every 128th event. Table 3.4 below shows the On-line print-out of the contents of the CAMAC scalers.

SCALERS											
1PI				2PI	488	454	PISIG		480	568	} 1→3 Permanent 4→6 scaler
S	475	853	787	SE	5	786	CLOCK	13	296	181	
3PI		256	851	4PI		0	E1	13	514	656	
E2	12	891	298	E3	17	171	E4	23	112	191	
E5	10	612	662	E6	12	852	E7	16	746	996	
E8	26	192	649	E9	10	152	E10	10	572	701	
E11	12	969	279	E12	19	938	E	165	147	934	
MTN1	5	769	730	MTN2	9	140	MTN3	14	629	679	
MTN4	5	980	805	MTN5	6	301	MTA1	16	193	922	
MTA2	16	340	077	MTA3	12	591	MTA4	20	885	812	
MTA5	10	518	020	NC1		26	NC2		32	003	
NC3		41	024	NC4		30	NC5		22	754	

Table 3.4. The CAMAC scaler

The Multiscaler is activated for 10s and the number of counts collected are written in the LOG-book. The crew on shift is obliged to every now and then write down the rates displayed on the Multiscaler. This facilitates detection of errors in electronics or changes in beam. Some representative excerpts are shown in table 3.5.

RUN	t(s)	$I_p(\mu A)$	$1\pi \times 10^6$	$2\pi \times 10^6$	π -sign. $\times 10^6$	$S \times 10^6$	$E \times 10^6$	SE	CC
220MeV/c	π^+	10	130	19.75	11.70	11.27	1.14	0.31	22952 111
	π^-	10	120	21.7	13.4	11.9	2.64	0.74	22193 106

Table 3.5. Contents of Multiscaler

3.3.7. THE FAST-CLEAR FACILITY

- Purpose:**
- To provide Fast-Clear signals for the E-counter CAMAC modules if no CC occurs following a SE-coincidence.
 - To provide Fast-Clear signals for the ADC's of a module i (1-5) of the TOF-counter if no CC occurs following a TOFi-coincidence.

Different fast-clear (FC) signals are of interest depending on the measuring configuration. First we treat the normal configuration with the E-counter and one TOF-counter. Second, we discuss the case then two TOF-counters are taken in coincidence with each other.

While the TOF-counter may produce a signal of up to 150ns after the pion entered the target, the E-counter information is fed into the CAMAC prior to the arrival of the TOF-counter signal. If no TOF-counter signal arrives, i.e. no TOFi-coincidence and hence CC occurs, the information stored in the CAMAC-modules is cleared. The FC-E signal used for this purpose is produced by the SE-signal taken in anti-coincidence with the CC i.e. in coincidence with an inverted output of the CC. Since both signals have the timing of the RF the output of CC can be taken short (25ns). The FC-signal, which has a width exceeding 50ns, forces all channels in a module to cease their conversions, to be cleared and to be ready to accept another gate after 1.2 to 1.5 μ s. Figure 3.40 shows the electronics and the time chart for recorded events (no FC).

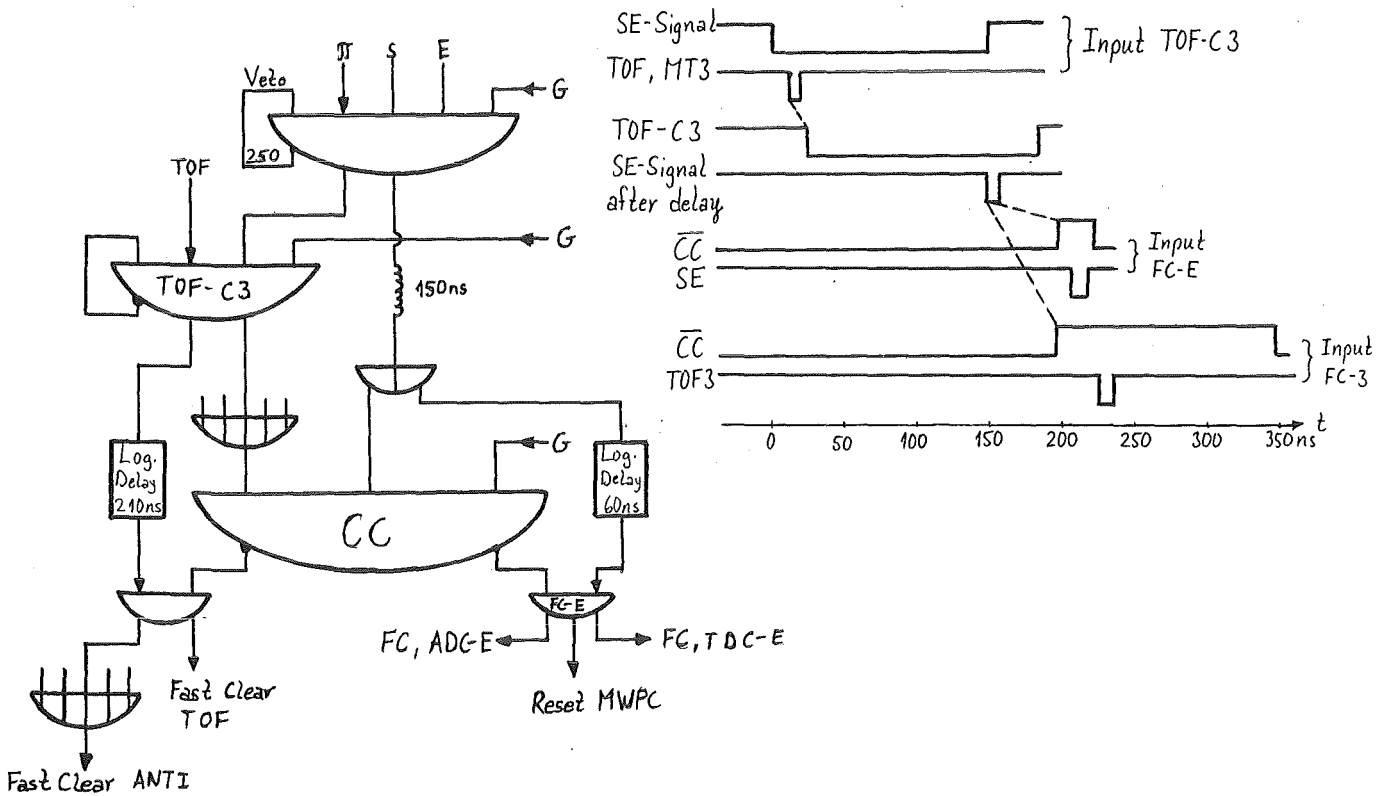


Figure 3.40. Electronics for FC and signals.

In the normal set-up with an E-counter and a TOF-counter a TOFi-coincidence is invariably implying a CC. The output of the TOFi-coincidence can, therefore, without presumption be used as gate for the ADC of module i. However, if a coincidence between two TOF-counters is required it is no longer true. In this case, which will be treated in more details in section 3.3.9., and during a cosmic ray calibration (cf. § 3.3.10.) a TOFi-coincidence is not equivalent to a CC and the information stored in the ADC's has to be cleared by a non-occurrence of a CC. The FC-i signal thereby used for module i of the TOF-counter is produced in the same way as the FC-E signal, i.e. by an anti-coincidence between the TOFi-coincidence and the CC. Since the signals have different timing the CC-output has a duration of 150ns, see figure 3.40. A fast-clear is also applied to the ADC's of the ANTI-counter. Since these are combined in one CAMAC module all ADC's are cleared simultaneously.

3.3.8. THE COMPUTER LINK AND THE DEAD TIME LOGIC

Purpose: *To produce a Look-At-Me (LAM) signal initializing a read-out of the information stored in the CAMAC modules.*

To veto the main coincidences until the computer has read the data or, in the case of a fast-clear (§3.3.7.), until the contents in the CAMAC modules have been cleared.

The LAM signal calls the attention of the computer to the fact that there exists information in the CAMAC modules ready to be read. Since the ADC's and TDC's requires up to $60\mu\text{s}$ and $100\mu\text{s}$ respectively, to convert the information fed into them into a digital form, the LAM signal has to be delayed accordingly. In a timing unit, TU1, the CC signal is delayed $100\mu\text{s}$ after which internally a flip-flop (LATCH) is set, producing the LAM signal, see figure 3.41.

The reset of the LAM signal is made by the computer notifying the start of the read-out task.

Once an event is accepted in the different coincidence levels it must be assured that no second event jeopardizes the information. On the short time scale this is accomplished by vetoing the coincidences with their own outputs. In addition, by letting CC set a flip-flop, TU2, we can produce a veto signal, \bar{G} , inhibiting the coincidences. The computer resets TU2 when it is ready to accept new data.

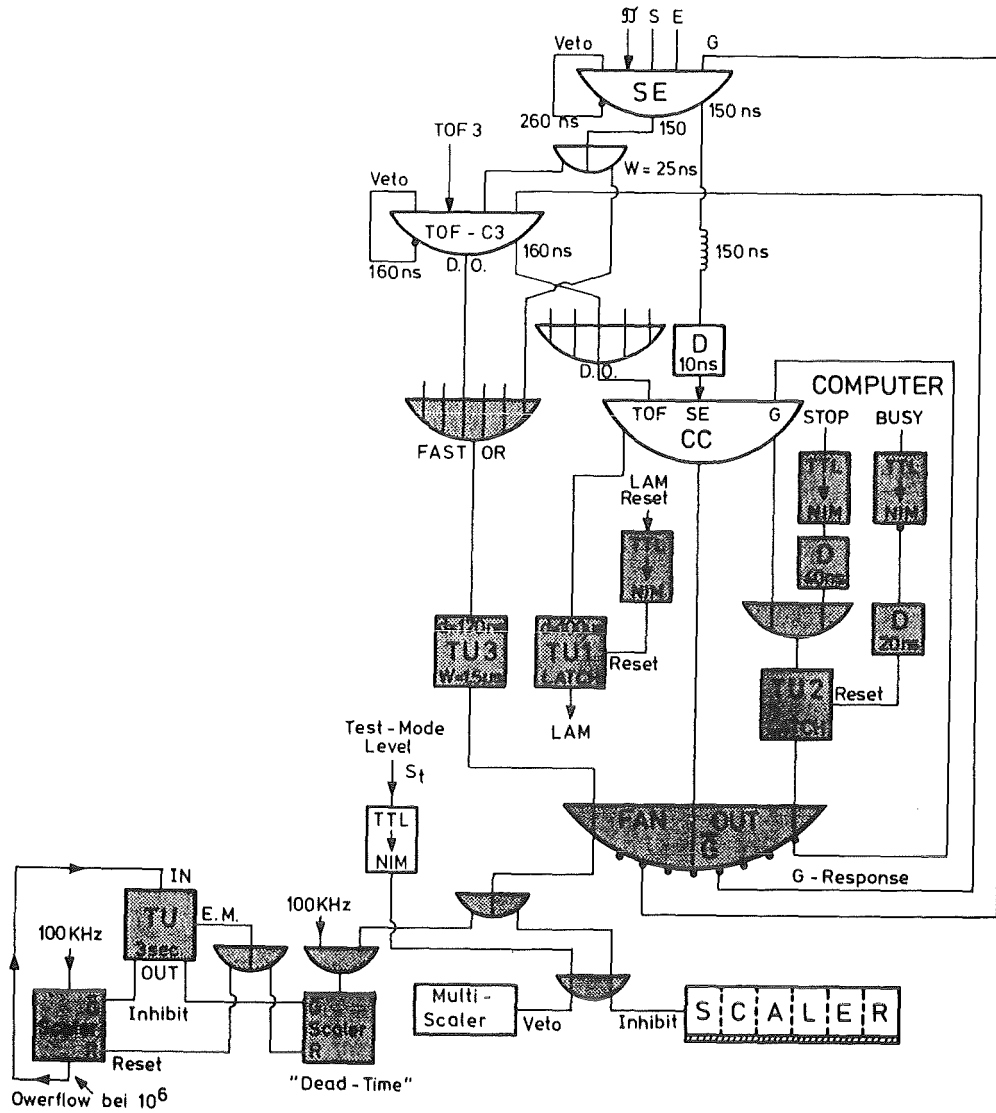


Figure 3.41. The Computer Link And The Dead Time Logic.

The CAMAC delivers two TTL outputs indicating the status of the computer: C'BUSY and C'STOP. The C'BUSY signal says that the computer is busy and can not handle a new LAM-interrupt. The C'STOP signal indicates that the data acquisition is stopped, e.g. a stop command has been entered on the keyboard or the tape is full. If none of these levels are present, the computer is ready to accept data. Like the CC the C'STOP signal sets the flip-flop, TU2, which is reset by the trailing-edge of the C'BUSY-signal.

By feeding an inverted output of a coincidence into the coincidence itself we can inhibit the coincidence for the duration of this output. The SE-coincidence is inhibited for the duration of 260ns whereas the veto signal of a TOFi-coincidence has a width of only 150ns. These widths are limited by the devices used. Obviously, this requires a fast response from the CC, \bar{G} , if the coincidences shall be inhibited -- without a gap -- from the moment of a coincidence until the computer is ready to accept a new event. Figure 3.42 shows the time chart of the signals.

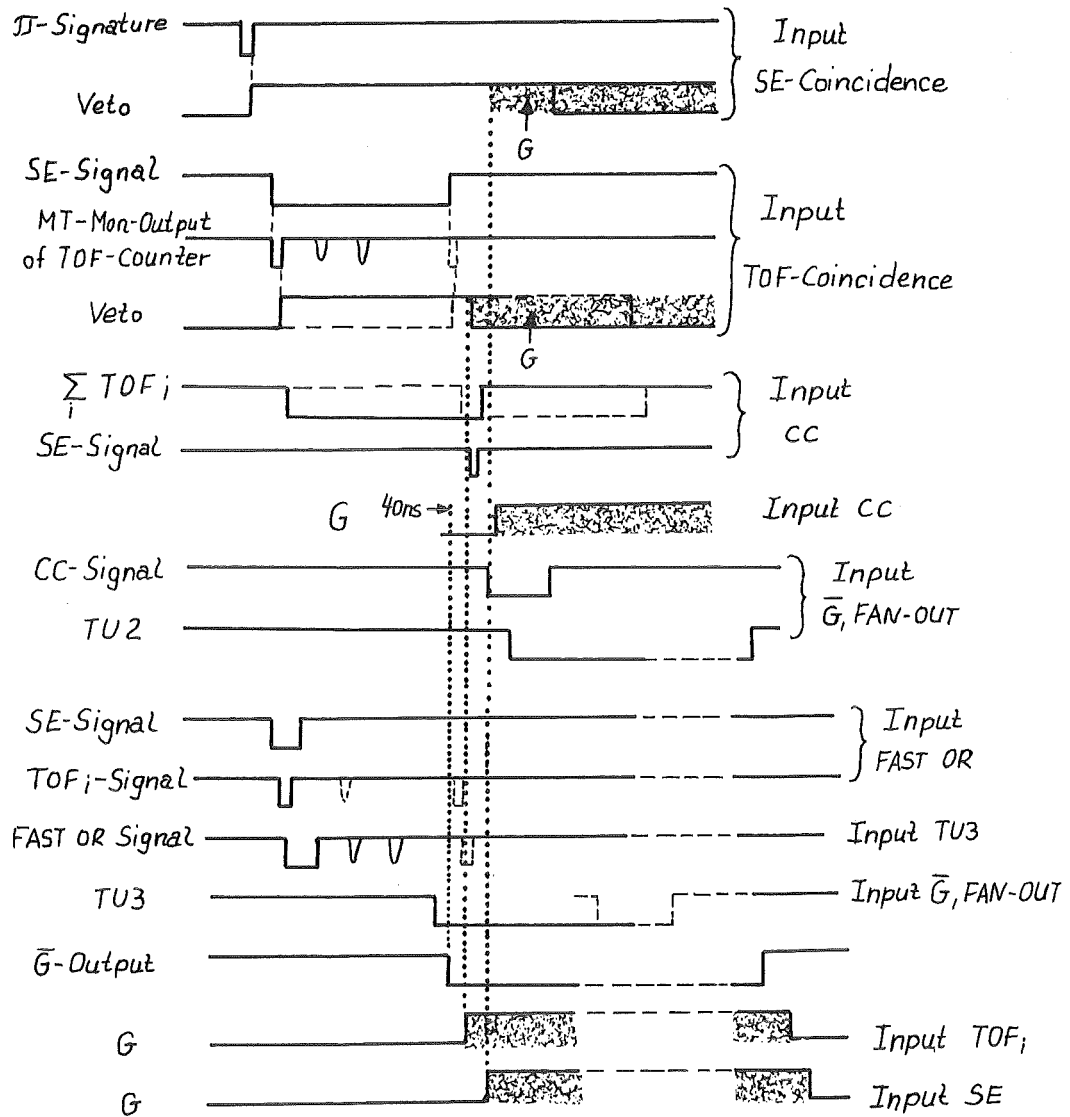


Figure 3.42. Time chart of signals.

As the TU2 has an intrinsic delay of $\approx 15\text{ns}$, we can speed up the arrival of the G-response by bypassing it with a direct-CC signal and adding the two signals in a fan-in. In case of a fast-clear the coincidences have to be inhibited for the duration of the $1.5\mu\text{s}$ it takes to clear the CAMAC modules. This $1.5\mu\text{s}$ dead time is always applied, also in case of a CC occurrence, since in the latter case a longer dead time will be issued. The six main coincidences (SE&TOFi) are therefore always fed into the "fast-OR" succeeded by a timing unit, TU3, delivering a signal of $1.5\mu\text{s}$ duration. In order to avoid that with this additional branch self-blocking shall occur at the CC the first part of TU3 delays the signal by 130ns and in addition the \bar{G} -response to the CC is delayed 40ns . See figure 3.42.

3.3.9. ADAPTATION FOR TOF- VERSUS TOF- COINCIDENCES

Purpose: □ To enable detection of nn -coincidences, e.g. $\pi^-(^3\text{He}) \rightarrow (p)nn$.

A blockdiagram of the realization is shown figure 3.43.

The S- and E- signals are taken out of the SE-coincidence. The SE-coincidence is now equivalent to the π -signature. Since we do not want any unnecessary dead time we put the coincidence unit in an updating mode by eliminating the veto input.

In this case a TOFi-coincidence is a coincidence between the signature of the incoming pion and a particle detected in TOF-counter module i. To obtain a second TOF-counter modules are dismounted from the common counter rack and mounted on a second counter rack (cf. subsection 3.2.4.2.). The two TOF-counters with altogether five modules will be denoted I and II, respectively. Instead of adding all five TOFi signals with a fan-in, we add only those belonging to the same counter. This change is easily accomodated since our fan-in consists of two separate 6-fold fan-ins, A and B, which by means of a switch can be added, A+B, or separated. The output of fan-in A and B are both fed into the CC. The SE-input into the CC is retained and determines the timing.

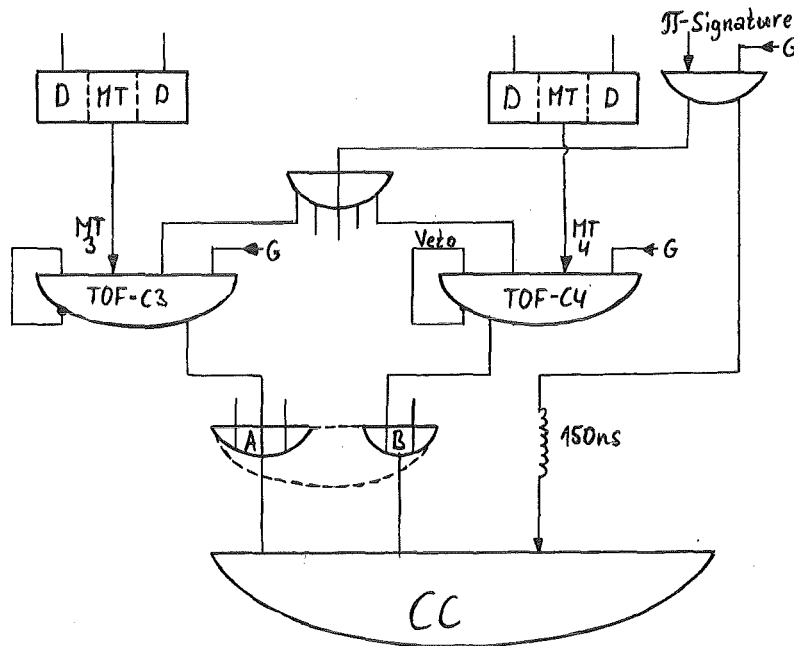


Figure 3.43. Electronics for TOF- vs. TOF- coincidence

In this configuration a TOFi-coincidence is not equivalent to a CC and information stored in the ADC-TOFi has to be cleared by a non-occurrence of a CC, cf. section 3.3.7.

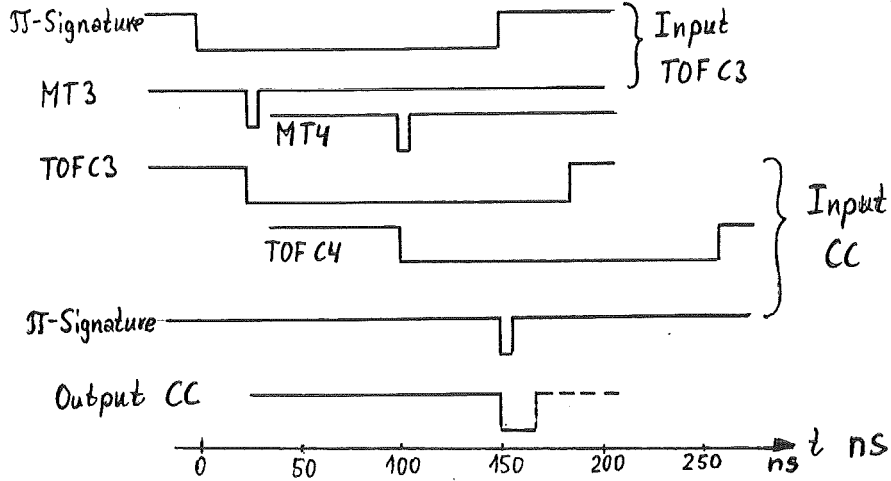


Figure 3.44. Time-chart of signals for TOF- vs. TOF- coincidences

3.3.10. THE COSMIC RAY LOGIC

Purpose: By means of a simple procedure adapt the electronics for a cosmic ray calibration measurement.

The adaptation can be made by one single switch as shown in figure 3.45.

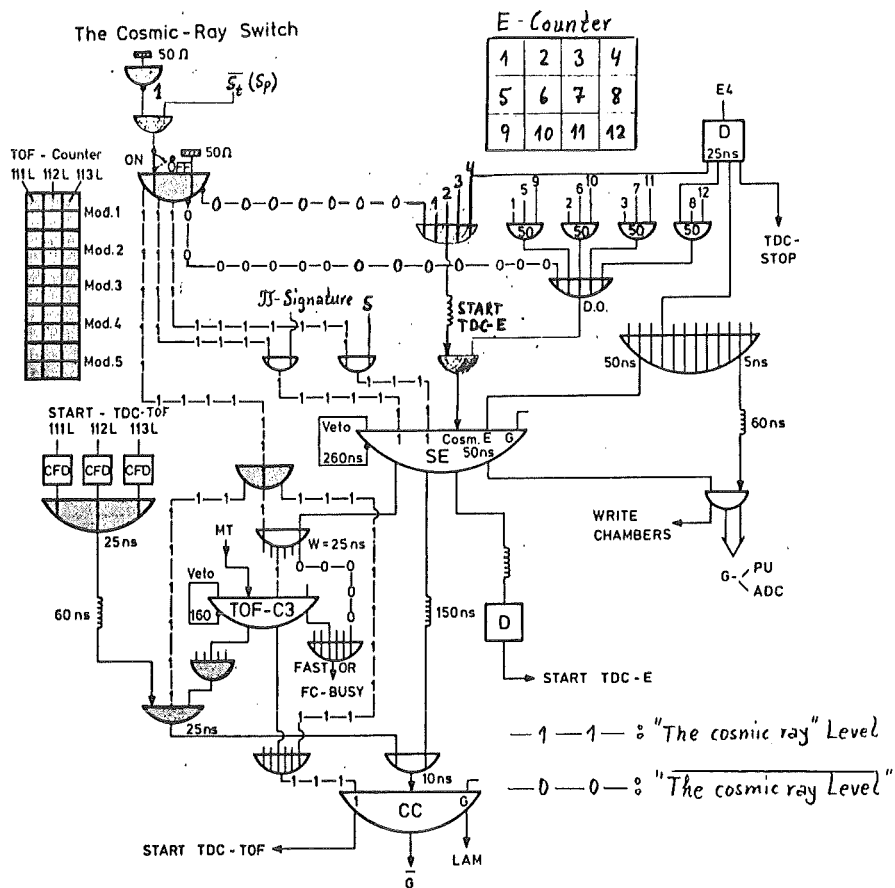


Figure 3.45. Adaptation for Cosmic Ray calibration

When looking for particles vertically incident, we require a coincidence between modules positioned on top of each other. In the E-counter this amounts to taking the three modules in a column in coincidence and ask for events in any of the four columns. Similarly, in the TOF-counter we require a coincidence between the five modules.

Although the primary goal of this measurement is to calibrate the light output of the LED's into MeV for future reference (cf. § 4.3.1.), it would be nice to use the TDC information. This, however, requires a definite start of the TDC's. Since there is a slight difference in cable lengths and response of the PM tubes, we let the uppermost PM tube respond to a cosmic ray event to start the TDC's.

For this purpose an additional circuit is used, see figure 3.45. In the E-counter the one of the 4 uppermost modules detecting the event, is impressing the timing on the obtained cosmic ray trigger signal. In the TOF-counter, similarly, the uppermost PM tubes on the left side determines the timing. The not correlated signals like the π -signature and S-counter in the SE-coincidence and -- since the cosmic ray events are exclusive -- the SE-signal in the TOFi-coincidence are replaced by the cosmic ray level. Through an "OR" both trigger signals are fed into the SE-input of the CC whereas the TOF input is replaced by the level.

By knowing the time-of-passage through the counter ($\beta \simeq 1$) and the conversion factor (channels/ns, cf. § 5.2.5) of the TDC's, we can adjust the TDC-spectra for the PM tubes in one column relative to each other. In order to determine the conversion factor without taking resort to the regular measurement, during test mode the cosmic ray level is eliminated by means of an anti-coincidence with the test-mode level, S_t (cf. section 4.1.).

3.4. THE ON-LINE DATA ACQUISITION SYSTEM

The data acquisition and on-line analysis was performed with a PDP 11/40 computer connected to the counter electronics via the CAMAC-system (cf. §3.3.). The data acquisition system also included two disc stations, two magnetic tape units, a teletype, a line printer with graphics capability and a Tektronix graphic display. The PDP 11 itself had an extended core memory of 128k (16bit) words. Eighty k is reserved for histograms and 24k for the on-line program, OMT, [98], which was especially developed for this experiment.

3.4.1. THE ON-LINE PROGRAM

As far as event-processing is concerned the on-line program is divided into three major parts:

- I *Readout of the CAMAC-modules into the **DATA VECTOR (DV)** (highest priority).*
- II *Writing of the CAMAC data onto the magnetic tape.*
- III *Manipulating the data for the on-line histograms:*
 - Applying gates.*
 - Performing arithmetical/logical expressions.*
 - Storing the data into histograms.*

From the users point of view, part I&II are hard wired, i.e. they can be changed only by an explicit change of the program by editing, assembling and linking. Part III in contrast is defined only as far as it is necessary from the organisational point of view. Tests and histograms etc. are instead defined in a **COMMAND FILE** for added flexibility. A precompiler, **PRECOM**, in a special language translates the source file of the command file into a binary file, [99]. At the start of the on-line program the user is asked for the name of this file and tables and instructions are read into predefined areas of the on-line program.

The data-vector is divided into four parts:

Address	Area
001-311	CAMAC-DATA The on-line program stores the contents of the CAMAC-modules into this area.
312-624	VARIABLES This area contain results of calculations and can be displayed in histograms. The data can be defined and/or modified by instructions defined in the command file, e.g. by invoking constants or indices (see below).

625-945 **CONSTANTS**

Data in this area are used as constants and may be changed during a run by using the 'NCONST' command. Typically they are the gain and offset of the histograms.

946-975 **INDICES**

We have many more quantities to display than we have histograms. With the indices we can select which quantities to display in a certain group of histograms. For example, we can only display the data of one TOF-counter module at a time and with an index we can assign the module. An index can be changed during the run by using the 'NIND' command.

The first part of the data-vector, containing the unmanipulated CAMAC-data, is read-only, i.e. the data is available for making histograms but remains itself unaffected. In this area each tube has a specific location. Only this data is conveyed on tape. This is done in parallel with making histograms. Since at most two modules of a counter have a signal we can compress the data. Thus, it is required that there exists a bit in the corresponding pattern unit. If, for example, in the pattern unit of the E-counter only bit 6 is set, then only the information of E-counter 6 is retained. The condensed data are stored in a data-buffer of 2k words. When the buffer is filled, the content is written as one record on a 800Bpl-magnetic tape. Usually the data of about 20 events fit into one record and one tape contains the information of some 1,500,000 events.

3.4.2. **SAMPLE OF ON-LINE HISTOGRAMS**

A sample of on-line histograms are shown on the next pages.

Figure Captions:

Figure 3.46: Target picture from the Chamber. This picture is used to adjust the beam-line.

Figure 3.47: Adjacency of the chamber planes.

Figure 3.48: Information from the pattern units.

Histogram a) shows the pattern of the rods of TOF-counter module 1,2 and 3. The largest response comes from the rods nearest to the target. Since it was a π^+ run the very highest response comes from the ANTI-counters.

Histogram b) shows the pattern of the E-counter modules (the first 12 bits) and the π -signature pattern.

Figure 3.49: Time-of-flight spectra of the TOF-counter.

Figure 3.50: Pulse height vs. time-of-flight for the E-counter during a π^- run. The deuterons can be identified. However, the different particles are not clearly separable on-line because of the large contamination of electrons. See figure 3.51.

Figure 3.51: TDC-spectra of the S-counter for a π^- and a π^+ run. The spread in time-of-flight is small since this counter is positioned very close to the target. However, about 10ns after the real reaction products we see a bump in the spectra of the π^- run. This is coming from the large contamination of electrons in the π^- beam. The contamination in the π^+ beam is much less. See figure 3.4. The third peak belongs to the next pion burst. The unwanted events are eliminated off-line.

Figure 3.43. Target picture

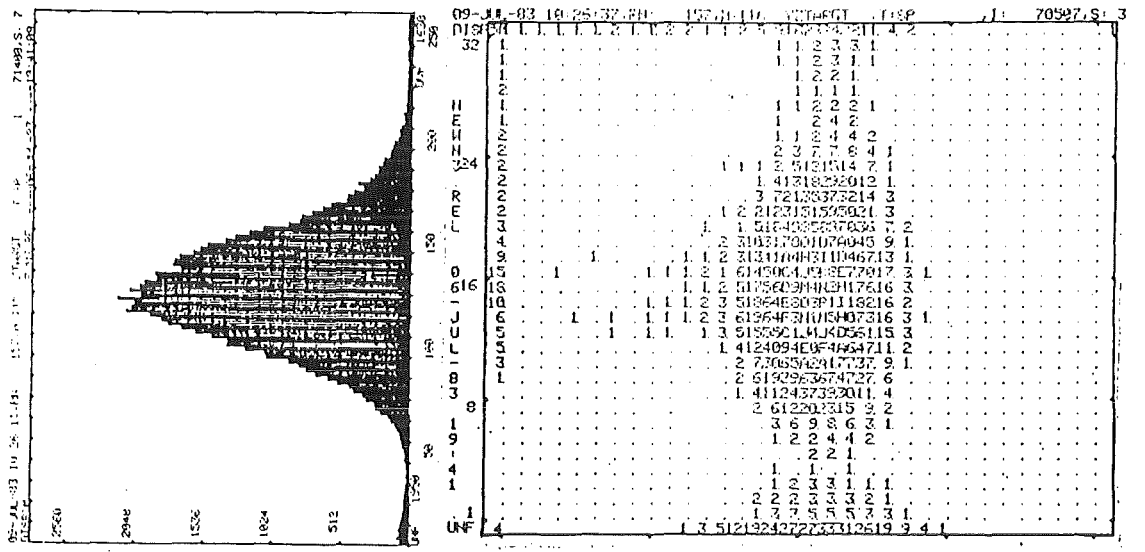
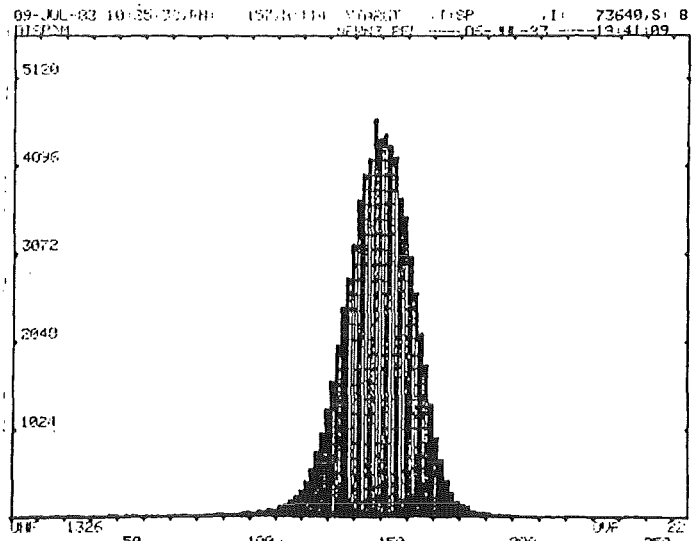


Figure 3.47. Adjacency of Chamber planes

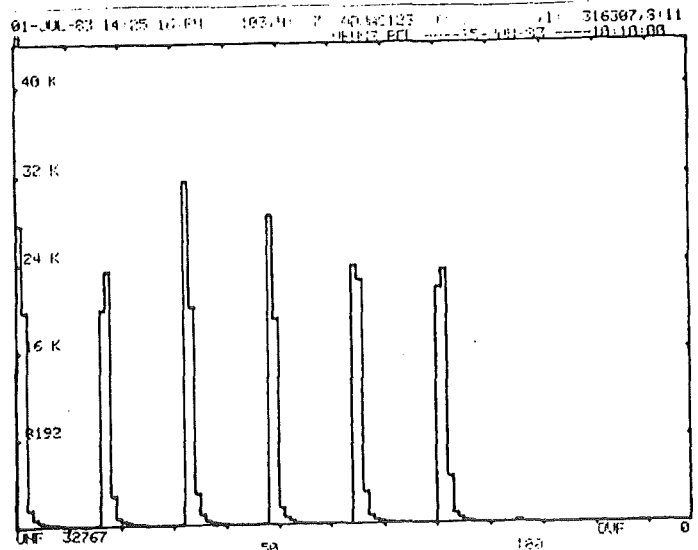


Figure 3.48a.

Pattern units

Figure 3.48b.

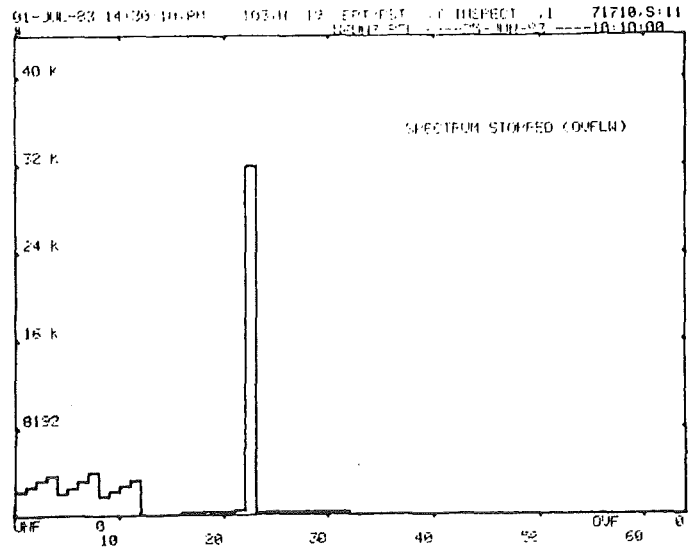
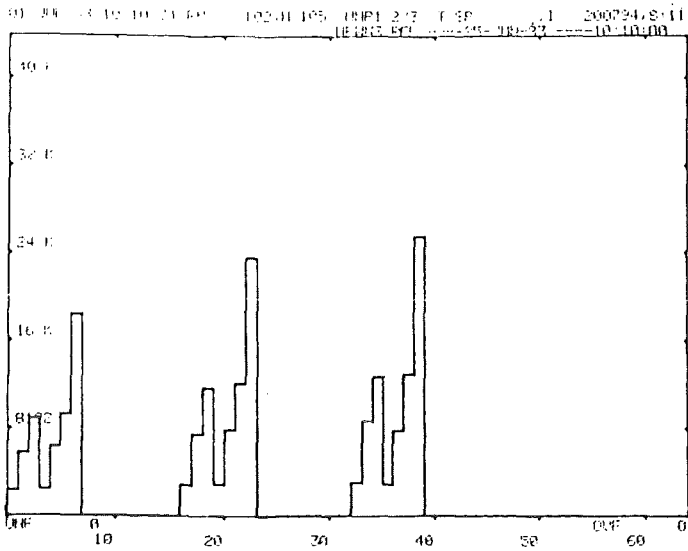
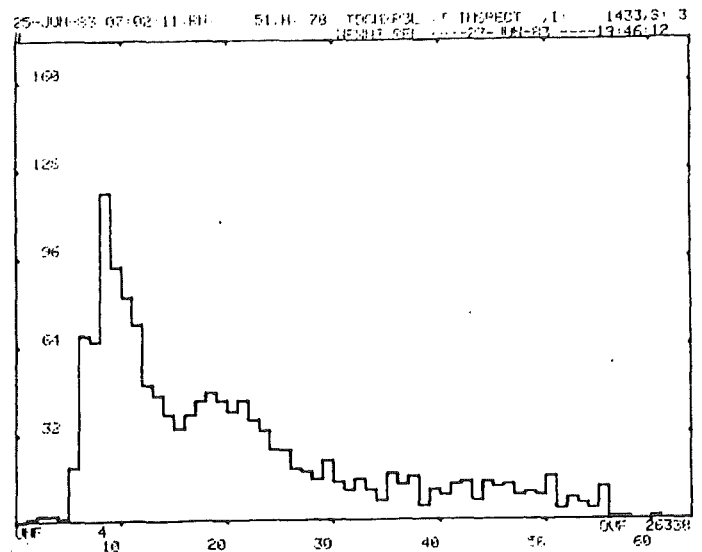


Figure 3.49. TDC-spectra of TOF-counter



CHAPTER 4: ADJUSTMENT & CALIBRATION OF EQUIPMENT

TEST EVENTS

To cancel gain fluctuations of the photomultipliers, which depend on beam intensity and temperature, as well as possible changes in the subsequent electronics, yellow LED's provided with temperature compensation are optically coupled to the lightguides of all counters. The signals which fire the LED's are taken from fast pulsers -- working with avalanche-transistors -- giving +50V pulses with a duration of about 1ns. The pulsers are triggered externally by the pick-up signal of the RF pre-scaled down to 50Hz. By taking this 50Hz in coincidence with a test mode level, S_t , we are able to temporarily activate the pulser after a preselected number of real events.

The pulsers for all counters are triggered by the same RF pulse. We adjust in time the trigger signals of the different pulsers in order to simulate the time-of-arrival of particles in the different counters. For the E- and TOF-counter different delays corresponds to different particle energies. For this purpose additional delay boxes have been installed in the barrack. The cables in the area are thereby adjusted so that the minimal delay corresponds to the prompt peak ($\beta=1$) in the E- and TOF-counter at the given distance.

A simplified diagram of the test electronics is shown in figure 4.1. Only two cable lengths are provided for changes:

- ☞ *By changing cable 2 the π -signature coincidence is adjusted in the test mode.*
- ☞ *Cable 1 does not influence the coincidence. It has however to be adjusted in the normal mode to correct for changes in time-of-arrival of pions relative to RF.*

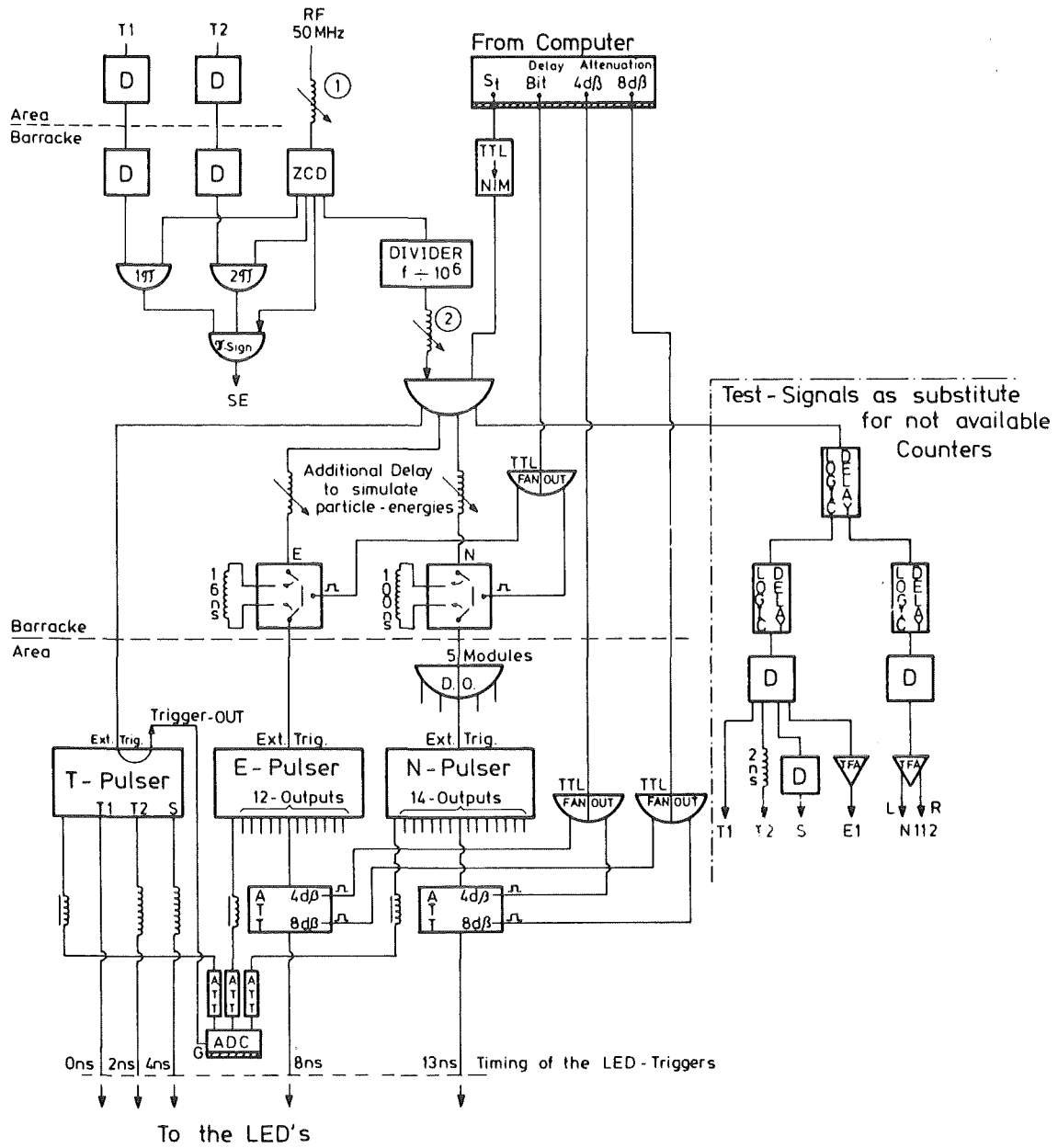


Figure 4.1. Test electronics

When varying the pion momentum from 270, to 220 and 170MeV/c we were required to change the length of cable 1 from 4, to 10 to 17ns which was in good agreement with theoretical estimates of figure 3.6.

Also the SE-coincidence as well as the TOFi-coincidence can be adjusted with pulsers. However, in the TOF-counter the test events differ from the real events since they originate from two light sources. This has the effect that the mean-timer output is produced earlier, by half the total propagation time in the counter ($\approx 7ns$). This was taken into account when adjusting the gates of the ADC and PU, since the meantimer determines the time of the gate.

To be able to separate the pulse height variations, observed in the ADC-spectra, into gain shifts and offset fluctuations, remote controlled attenuators are inserted between the pulser- outputs and the LED's of the E- and TOF-counter. The pulser amplitude can thus be attenuated by 4, 8 and 12dB giving rise to 4 peaks in the pulse height spectra. Since the amplitude from the photomultiplier is proportional to the power delivered to the LED, and hence to the scintillator, the attenuations finally corresponds to 8, 16 and 24dB (amplitude units).

In the E-counter which uses slow photomultipliers, XP2041, the test signals very well resemble the real signals whereas in the TOF-counter, with the fast PM-tubes XP2230B, the rise time of the test signals is about 3ns larger than for the real events.

To calibrate also the TDC's the pulsers for the E-counter and the TOF-counter are delayed an additional $\approx 16\text{ns}$ and $\approx 100\text{ns}$ respectively for half of the test events.

In order to be able to perform tests on the electronics and the on-line program with the counters not connected, special test signals are available in the barrack. These signals are generated by the same RF pulse used to trigger the pulser-units for the LED's. This 50Hz-signal is delayed 750ns -- the time required to receive a LED-signal from a counter in the area -- and fed into timing-filter-amplifiers to obtain analogue signals of about the same shape as the LED-signals. These signals are adjusted-in-time so that they in test mode can replace the signals coming from the counter, one at a time, without changing the coincidences.

4.2 PROPERTIES OF THE TOF-COUNTER

The problem with large area scintillators is that during the propagation in the counter the light pulse gets attenuated and the shape changed. Since the attenuation in the counter is exponential $\sim e^{-x/L}$, there L is the attenuation length, the geometrical mean value, $\sqrt{Ph_L \times Ph_R}$, is a position independent measure of the energy deposited in the counter. The time-of-flight measurement with the TOF-counter is treated in sections 5.2.4 and 5.2.5.

Test measurements of the counter were performed with a ^{60}Co and an Am-Be source. The geometrical mean of the analogue signals from both photomultipliers was calculated off-line. See figure 4.7a. The light attenuation over the whole rod of 200cm amounts to a factor of 2.5 and 8.2 for the TOF- and the ANTI-counter respectively. This corresponds to attenuation lengths of 218cm and 95cm. The effective propagation time difference for light initiated by radiation at the near or the far end of the rod was determined as 24ns, cf. figure 4.7b.

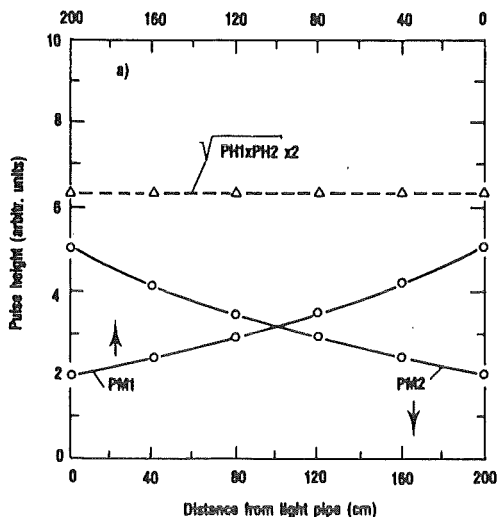


Figure 4.7a. Measured light attenuation and propagation characteristics.

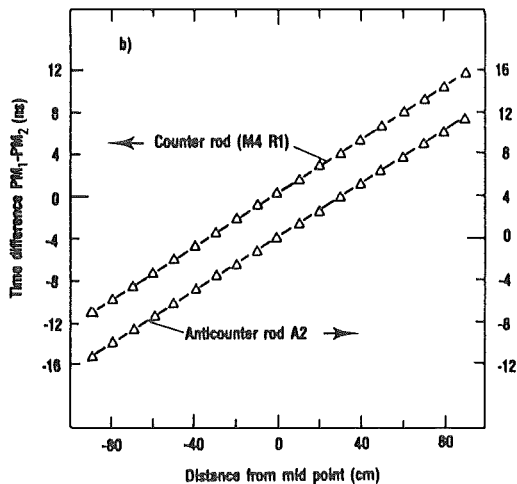


Figure 4.7b.

4.3. CALIBRATIONS WITH COSMIC RAY MUONS

A test of the TOF-counter with cosmic ray muons is treated in appendix B. The muons are minimal ionizing and deposits 2.1MeV_{ee}/cm upon traversing a plastic scintillator. The light output of the LED's is calibrated with the help of the cosmic ray muons in order to have a permanent energy reference which is independent on occasional gain fluctuations of the photomultipliers. The cosmic ray muons can also be used for alignment in time of modules positioned on top of each other. The modifications in the electronics for a cosmic ray calibration measurement is treated in section 3.3.10.

4.3.1 CALIBRATION OF LED'S

The angle of incidence is restricted by requiring that the muon has traversed modules on top of each other. A simple Monte Carlo program has been developed [10] which calculates the pulse height distribution in the different modules. This program takes into account the finite energy resolution of the counters ($\approx 10\%$) as well as the angular distribution of the cosmic ray muons.

We first treat the E-counter where the Energy of the particle is obtained through the pulse height.

THE E-COUNTER: In the E-counter we require that the muon traverse the three modules in one column. This gives a lower limit to the distance of propagation through the middle counter whereas no lower limit exists for the upper and lower module. See figure 4.15.

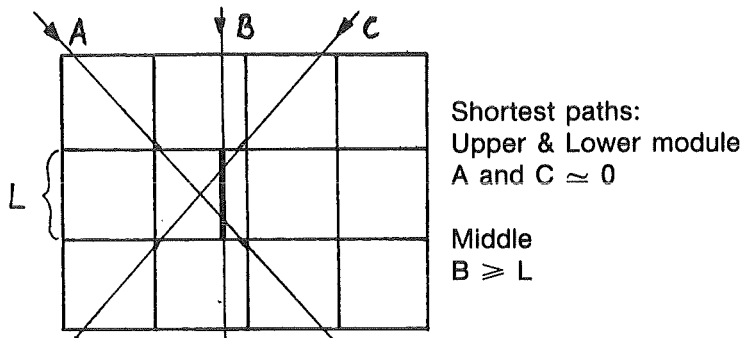
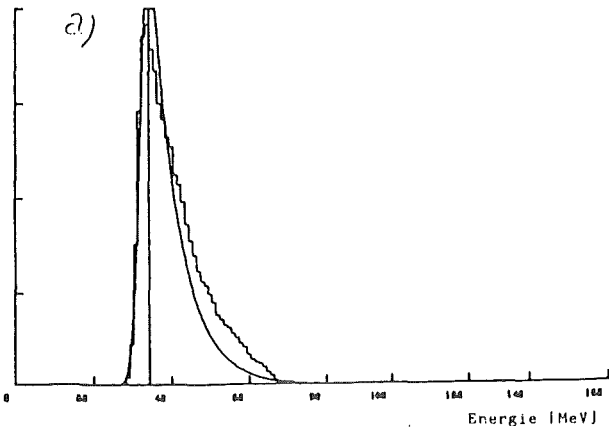
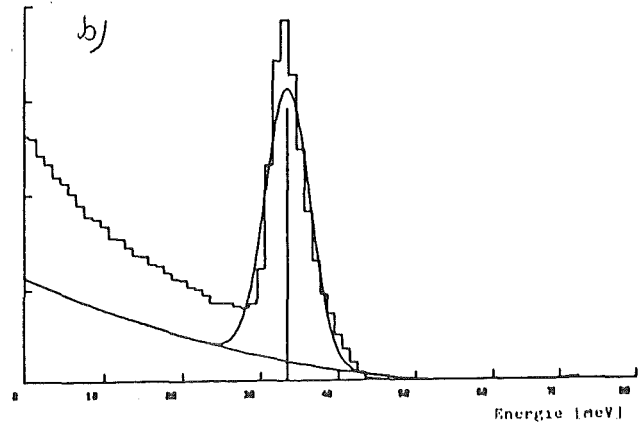


Figure 4.15. Propagation through E-counter

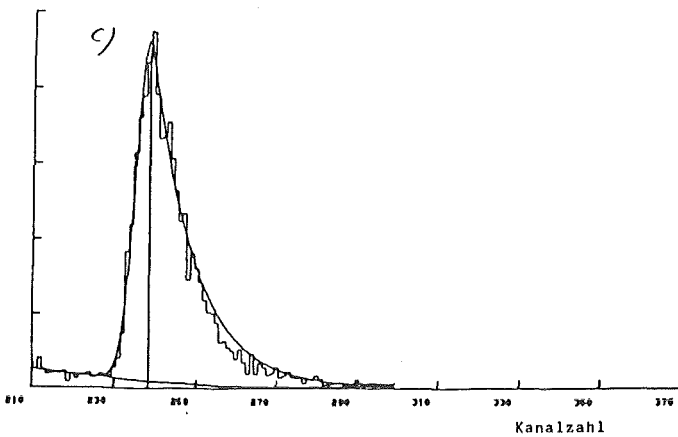
Figure 4.16 shows calculated vs. measured pulse height spectra for a middle and an outer E-counter module. The agreement between the curves is very good.



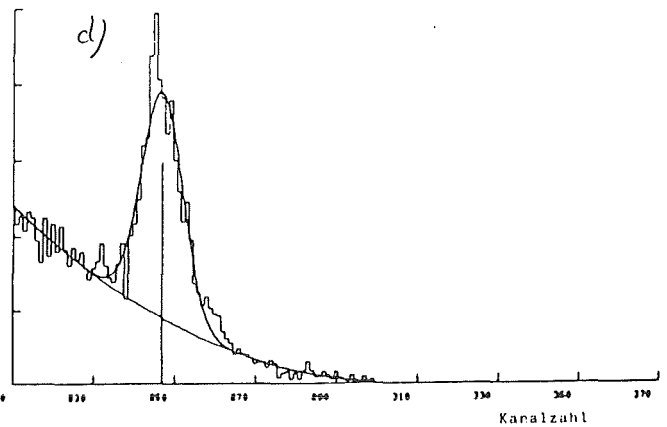
a) Calculation for middle module: 36.4 MeV



b) Calculation for outer module: 35.5 MeV



c) Measurement for middle module



d) Measurement for outer module

Figure 4.16. Calculated and measured pulse height spectra

Test events are intermittently produced during the cosmic ray measurement. The four peaks in the pulse height spectra corresponding to the 0, 4, 8 and 12dB attenuation are used to determine the offset. The LED's are approximately linear in our voltage range (0dB=50V to 12dB=12.5V). Figure 4.17a shows an LED-spectrum for an E-counter module.

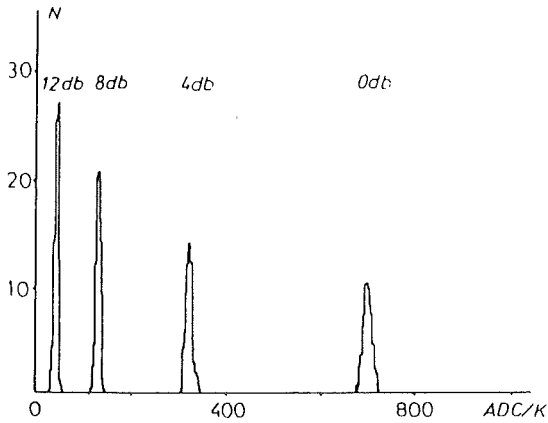


Figure 4.17a.
LED-Spectra

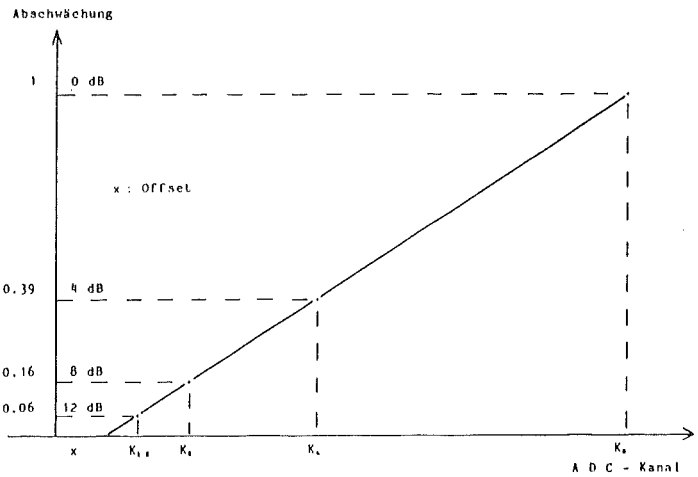


Figure 4.17b.
Offset determination

We consider the response of the LED's to be linear. Hence, we determine the offset of the system by plotting the position of the peaks in channels versus the attenuation. After correcting the cosmic ray spectra for this offset, the conversion factor f [MeV_{ee}/channel] can be calculated:

$$f_i = \frac{36.4 - \lambda \cdot 0.9}{k_i^{Cosmic}}, \quad \lambda = 1 \text{ for } i \in [4,6] \text{ (module in the middle)}$$

The position of the four LED-peaks and the conversion factors are stored in a calibration file. This file will later be used in the off-line data evaluation. See section 5.2.3.

THE TOF-COUNTER: A similar procedure is undertaken for the TOF-counter. In this case a coincidence between all five modules is required. The light attenuation over the whole rod length of 200cm amounts to a factor of 2.5. Hence, depending on position of impact the pulse height gets more or less attenuated. This is taken into account in the Monte Carlo program for the TOF-counter. Figure 4.18 shows a calculated and a measured pulse height spectrum.

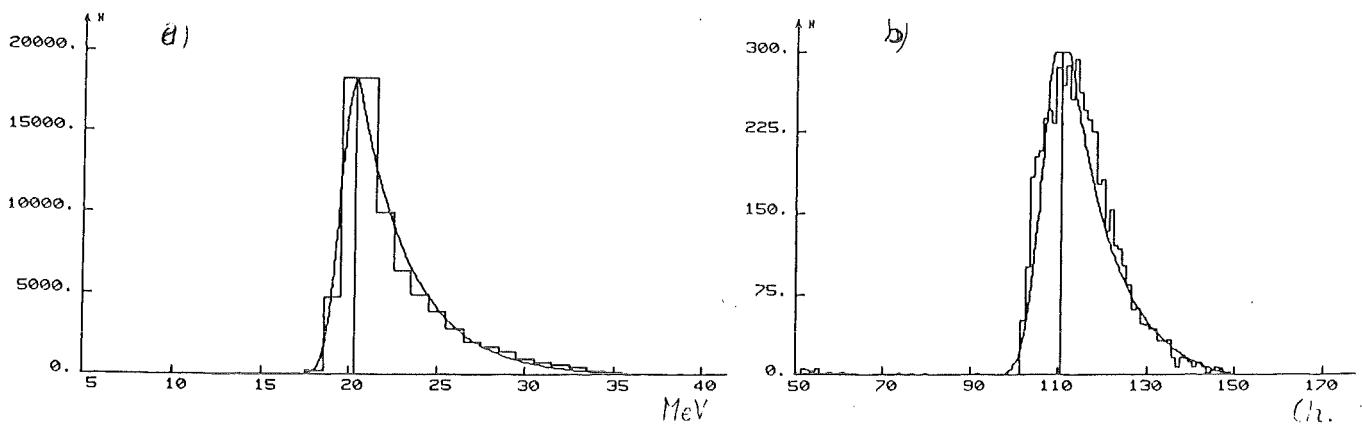


Figure 4.18. Calculated and measured pulse height spectra

a) Calculation for TOF-counter rod

b) Measurement for TOF-counter rod

The offsets of the pulse height spectra are obtained by means of the four peaks in the LED spectra. After correcting for the offsets, calibration constants are determined by means of which the peaks in the cosmic ray spectra is shifted to channel 150. Thus, offline we are giving all the photomultipliers the same gain and all the pulse height spectra the same conversion factor. We now calculate the geometrical mean value which is an independent measure of the energy deposited in the counter (§ 4.2.). Since the cosmic ray muons deposits 20.3MeV_{ee} the common conversion factor is $f=20.3/150=135\text{keV}_{ee}/\text{channel}$. The position of the four LED-peaks and the calibration constants of all 60 spectra are stored in a calibration file for later use in the off-line data evaluation. See section 5.2.3.

4.3.2. ALIGNEMENT IN TIME OF A COUNTER COLLUMN

The TDC information obtained during a cosmic ray calibration measurement is used to align counter modules positioned on top of each other.

During such a measurement we use the signal from the PM-tube of the uppermost module, responding to a cosmic ray event, to start the TDC's. Different angular distributions leads to different time distributions. Thus, since the angular acceptance for all rods are different the TDC-spectra for the PM-tubes in one collumn has all of them specific features. The Monte Carlo program mentioned in § 4.3.1. was extended to calculate the TDC-spectra of the different PM-tubes in one collumn of a counter. Figure 4.19 shows measured TDC-spectra for the middle collumn of the TOF-counter. In this counter we use the signal from the left PM-tube of the uppermost rod to start the TDC's. The agreement between the Monte Carlo calculation and the measurement is good.

Test events are intermittently produced during the cosmic ray measurement. In the test mode the "cosmic ray level" (cf. § 3.3.10) which otherwise adapt the electronics for a cosmic ray measurement is eliminated and the start of the TDC's is produced by the same 50MHz pulse which triggers the pulsers. Thus, also in this case we will have the two calibration peaks in the TDC-spectra for determination of the conversion factors c_i [ns/channel]. The conversion factors being determined we compare the measured spectra with the calculated and adjust all rods to the uppermost.

Unfortunately this facility did not exist at the time of the measurement presented in this work.

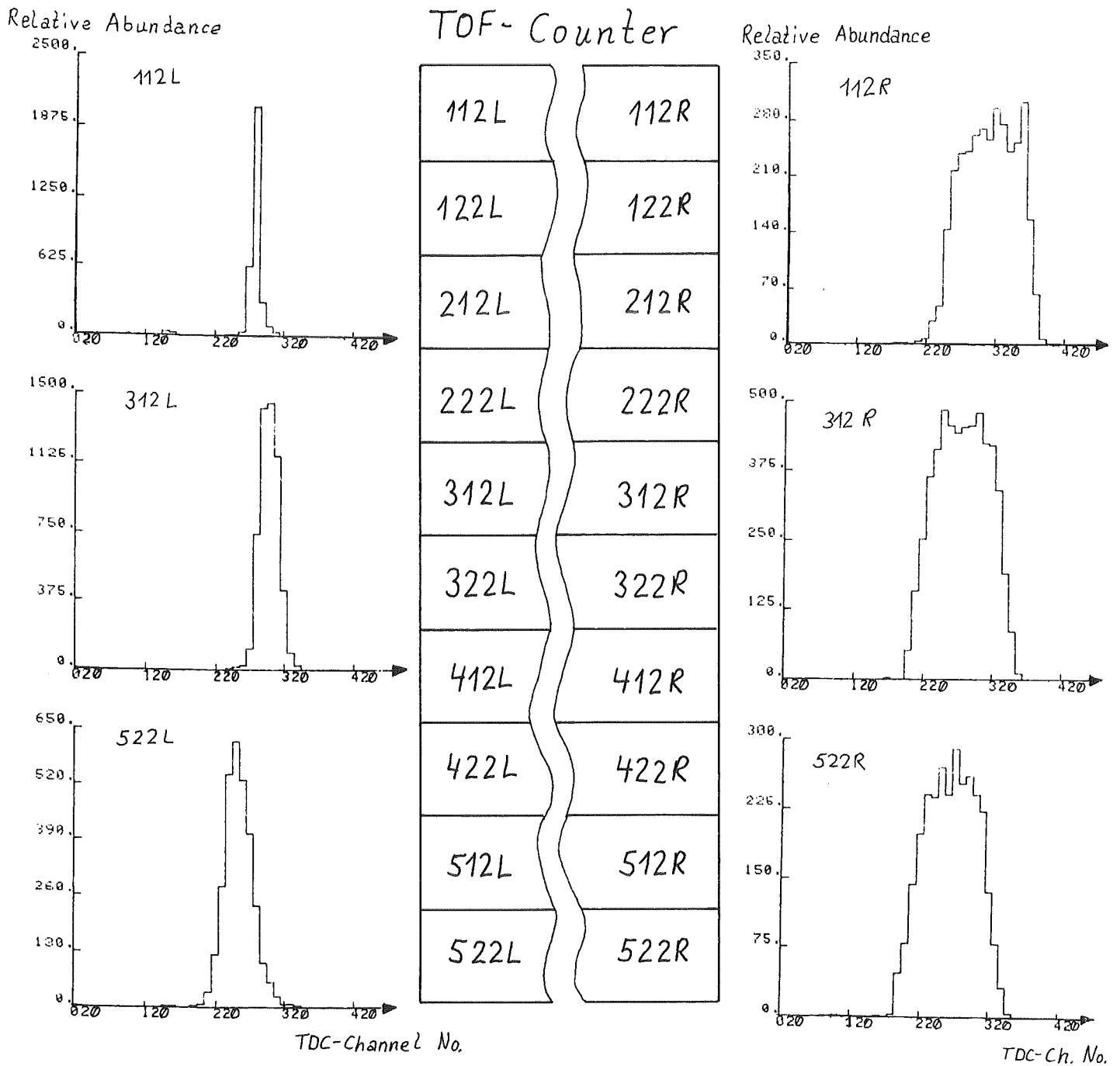
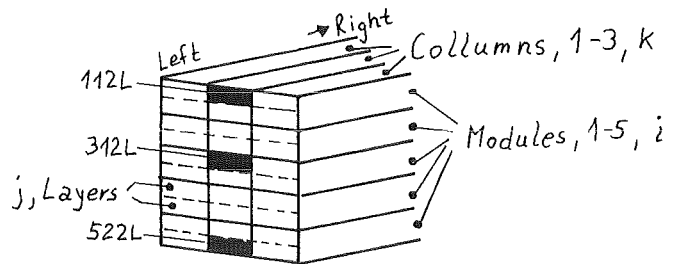


Figure 4.19. TDC-spectra during a cosmic ray measurement.

Notation: ijk i=number of the module
 j=number of the layer in a module
 k=number of the collumn



CHAPTER 5: OFF-LINE DATA EVALUATION

5.1. SURVEY OF ANALYZED DATA

The data presented here are the first results from the measurements of π^+ and π^- absorption in flight on ^3He . Position I of the E-counter was used from the run of October 1982 as was set-up 3 of June/July 1983. See figures 3.25 and 3.27. The statistics of the first experiment of October 1982 were quite poor. We, therefore, integrated over all 12 modules of the E-counter. In the second run of June/July 1983 the statistics were much better and data from a single E-counter module was sufficient for one data point. Only data from module 6 have been evaluated and only for two different pion energies, 120 and 165 MeV. Altogether this gives three data points of the isospin ratio R.

The evaluation of data from other E-counter modules and for different positions are in progress. The evaluation is only described for the measurements with the new TOF-counter. The evaluation for the old TOF-counter was similar and only the results are presented.

5.2 GENERAL LAYOUT OF THE EVALUATION

The data evaluation was performed on VAX II/780 computers at SIN and at the University of Basel. The main evaluation program, TAUS, reads primary data from tape, computes secondary quantities and stores the results in the form of binary files.

By using a program KASP we can display the binary data. This program creates two-dimensional scatterplots of any two entities and their one-dimensional projections. KASP also offers the possibility to reduce the data further by setting gates on any chosen entity. The results are stored in scatterplot files.

The scatterplot files are used as input to a program FLIRT. This routine offers different alternative shapes of cuts to be applied. These cuts can be introduced either in TAUS or in KASP.

5.2.1. PARTICLE SEPARATION IN THE E-COUNTER

Figures 5.1 and 5.2 show the pulse height versus time-of-flight for E6 during a π^- and a π^+ run. One can see clearly in both spectra the proton hyperbola. The deuterons can be easily identified in the π^- -spectra.

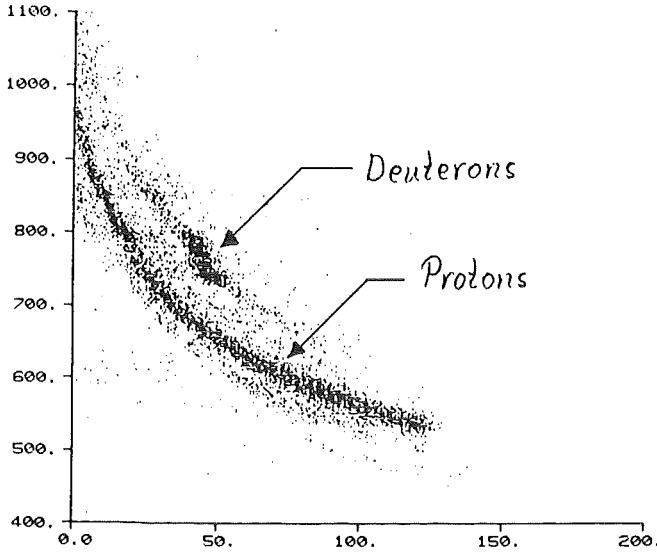


Figure 5.1. π^- run

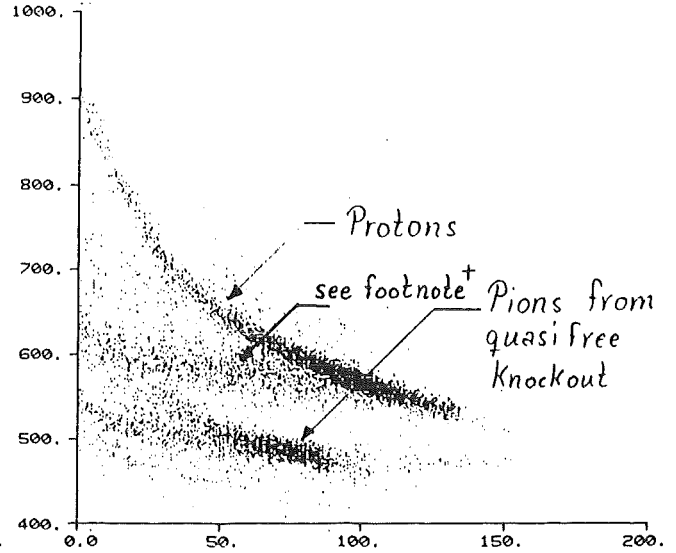


Figure 5.2. π^+ run

Pulse height versus time-of-flight for E6

5.2.2. CALCULATION OF THE ENERGY IN THE TARGET

The kinetic energy in the target, T_t , is easy to calculate for neutrons: from the time-of-flight, t_{of} , and the flight path, s , we have

$$T_t = m_n c^2 \left\{ \frac{1}{\sqrt{1 - (s/ct)^2}} - 1 \right\}, \quad m_n = \text{neutron mass}$$

Charged particles, however, lose energy due to ionization processes. The amount of energy lost by a particle per unit length of path, the stopping power $p(T)$, can be computed with the well known Bethe-Bloch formula. This theoretical expression of $p(T)$, however, depends on the average ionisation potential, I , of the substance, a quantity to be determined empirically. In view of this and of the less accurate results at low energies, i.e. below 8MeV for protons, we are using experimental data on the stopping power. Williams et al. [100] have made an extensive compilation for pure elements with an estimated accuracy of 2%.

Our program uses different semi-empirical formule depending on energy range to compute the stopping power in the gas mixtures and compounds used in our experiment. The energy in the target as well as the time-of-flight to the counter are calculated as a function of final energy. The input parameters are: density and thickness of the materials traversed in the right sequence.

†This branch is due to high energetic protons which traverses the side face of the module and thus does not deposit their entire energy in the module

5.2.3. CALIBRATION OF THE PULSE HEIGHT SPECTRA

We calibrate the pulse height spectra with the help of the test events (see § 4.1). The position of the four peaks in the pulse height spectrum, corresponding to the attenuation 0, 4, 8 and 12dB are plotted versus the actual attenuations, as determined in the cosmic ray measurement. See figure 5.3.

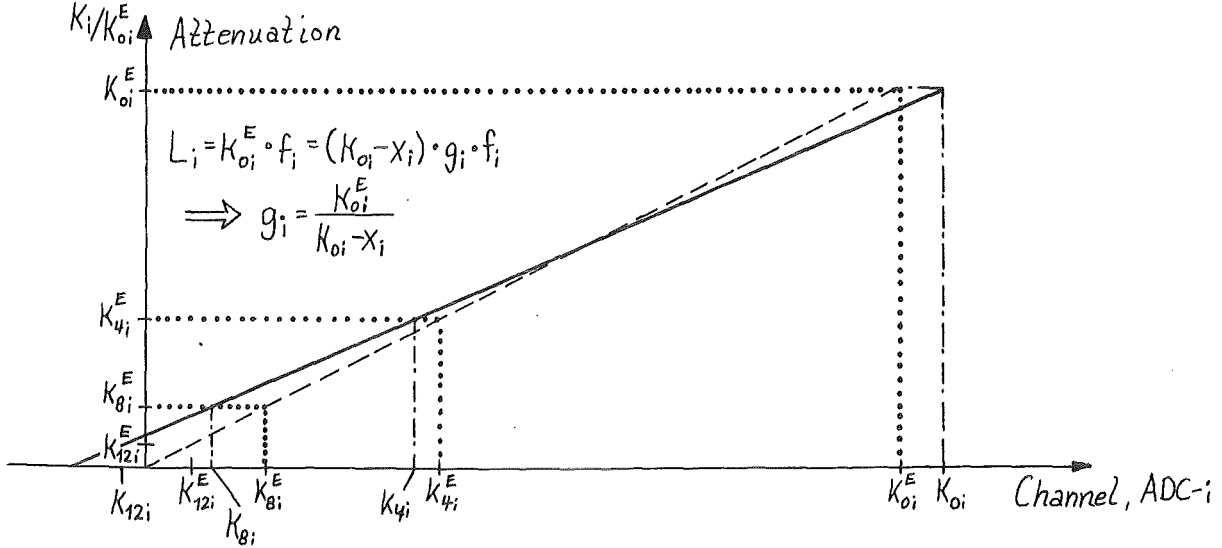


Figure 5.3. Calibration of an ADC.

Following eq.(3.10) we express the light output in electron equivalent units

$$L_i = (k_i - x_i) \cdot g_i \cdot f_i, \quad [L_i] = \text{MeV}_{ee}, \quad k_i = \text{ADC-Channel}$$

where f_i , the conversion factor ($[f_i] = \text{MeV}_{ee}/\text{channel}$), is determined in section 4.3.1. The offset, x_i , and the gainshift, g_i , can now be obtained. See figure 5.3.

For every run we need special pulse height correction files for E- and TOF-counter which relate the specific run to the conditions existing during the calibration measurement. A pulse height correction file contains the values of offset and gainshift for all photomultipliers in a counter. Due to the many photomultipliers this procedure is to a large extent done by special programs. By means of TAUS we read the ADC information of the test events, i.e. the four LED peaks. In a second step spectra for all photomultipliers are created. A program called LED finally creates the correction file. It determines the position of the peaks and relates these to the positions during the calibration run. The offsets and gainshifts are determined by linear regression. These values are written into the correction file.

The proton and the deuteron energies corresponding to a specific channel can now be obtained through eq.(3.11):

$$T_k(L_k) = \hat{a}_k L_k + \hat{b}_k \cdot \{1.0 - \exp(-\hat{c}_k L_k^{\hat{d}_k})\}, \quad k = \text{particle}$$

with coefficients given in table 3.3.

5.2.4. TIME-WALK CORRECTIONS

Pulses of different amplitudes but the same rise time cross a fix discrimina- tor threshold at different times -- small ones later, large ones earlier -- causing the triggering time to shift or "walk". This is the so called *time walk*.

The rise time of the light pulse increases during the propagation in the TOF-counter. Thus, since the time walk, t_{walk} , depends on the rise time, which is a function of the impact point on the counter, t_w is a function of pulse height and position: $t_w = t_w(Ph, x)$. By using a constant-fraction discriminator, CFD, to determine the timing for the TOF-counter, we are able to considerably reduce the time walk. The principle of operation of such a device is explained in appen- dix A.

The CFD's used in the experiment have been tested with pulses of 5.5ns rise time. This corresponds to the rise time of the pulses encountered in a real measurement. The total range of scattering from all the 70 CFD's is below 200ps over a range of 30dB, [103]. The correspondence between the time walk for the physical events and the test events (9ns rise time) is a factor of 1.3 over the same range. Figure 5.4 shows the result of the measurement. The solid line is the time walk correction to be applied for a given pulse height. Figure 5.5 shows the uncertainty in energy vs. the energy for a given uncertainty in time-of-flight. The curves are calculated for neutrons and a distance of 4m to the TOF-counter.

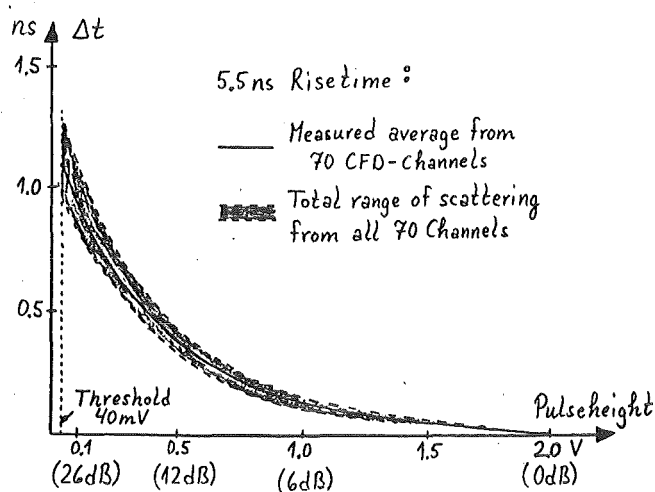


Figure 5.4.

Time walk of constant fraction discriminators [103].

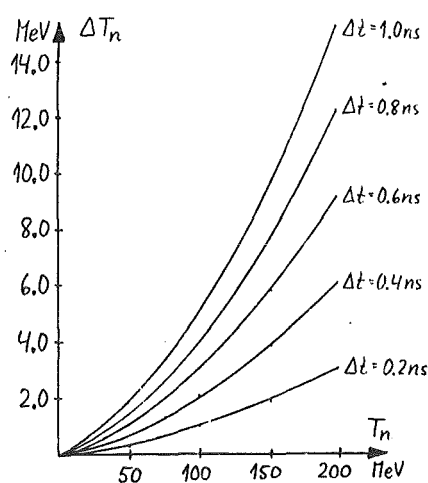


Figure 5.5.

Uncertainty in energy vs. the energy for given uncertainty in time-of-flight.

5.2.5. CALIBRATION OF THE TOF SPECTRA

We calibrate the TDC-spectra by delaying the trigger signals for the pulser of the E- and TOF-counters in one half of the test events. These additional delays are 16ns and 100ns, respectively. The number of channels between two peaks with the same attenuation gives immediately the conversion factor c_i [channels/ns]. We also determine the position (channel number) of the 0dB LED peak, k_i^{LED} . See figure 5.6. These parameters are stored in TOF correction files, separately one for the E-counter and one for the TOF-counter.

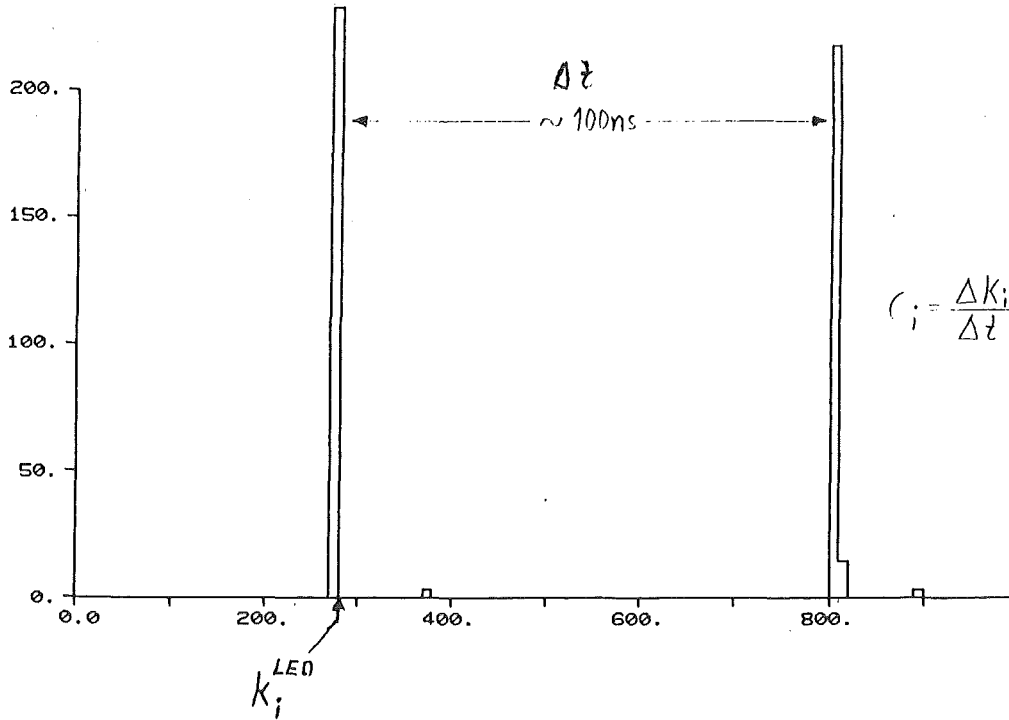


Figure 5.6. Calibration of a TDC-spectra

The most tedious part of the calibration is to obtain the absolute time-zero. Since all time fluctuations manifest themselves in shifts of the 0dB LED peak we make the calibration relative to the position of this peak. This facilitates the cancellation of occasional time fluctuations.

We now concentrate on the TOF-counter. In this counter we have TDC information from the photomultiplier on the left and right side of a rod. At this point in the calibration, we use the position of the 0dB peak (TDC-channel) as a time-zero for all photomultipliers. We now form the meantime between the left and right photomultiplier:

$$t_{Mean} = \frac{(k_L - k_L^{LED}) \cdot c_L + (k_R - k_R^{LED}) \cdot c_R}{2} \quad \begin{cases} k = \text{TDC-Channel} \\ c = \text{Conversion factor [ns/ch.]} \end{cases}$$

The meantime is a position independent measure of the time-of-flight to the counter, t_{of} , and is related to it by

$$t_{of} = t_{Mean} + \text{delay}$$

The TDC information from the TOF-counter is taken from the first layer which responds to the particle. Therefore, for a π^+ -run the second and third layer are not necessary, since all protons are detected in the first layer. However, neutrons from π^- -absorption may pass through the counter either without being detected at all or being detected in only one of the three subsequent layers. Therefore, for a π^- -run it is necessary to calibrate all the three layers.

For a π^- -run we use the monoenergetic neutrons from the reaction ${}^3\text{He} \rightarrow n\text{d}$ to determine the *delay*, i.e. the absolute time-zero. Figure 5.7. shows the time-of-flight of the neutrons as a function of the angle between the deuterons and the beam axis. During a π^+ -run the monoenergetic protons emitted after quasi-free absorption are used to calibrate the TDC-spectra. Figure 5.8 shows the time-of-flight of the proton detected in the TOF-counter versus the angle of the E-counter module to detect the other proton.

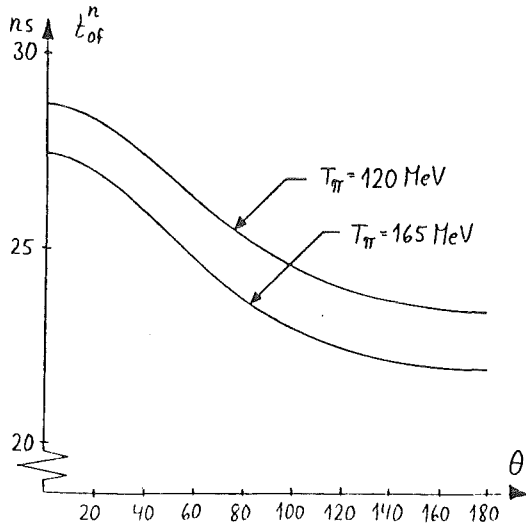


Figure 5.7. $\pi^-{}^3\text{He} \rightarrow n\text{d}$ kinematics

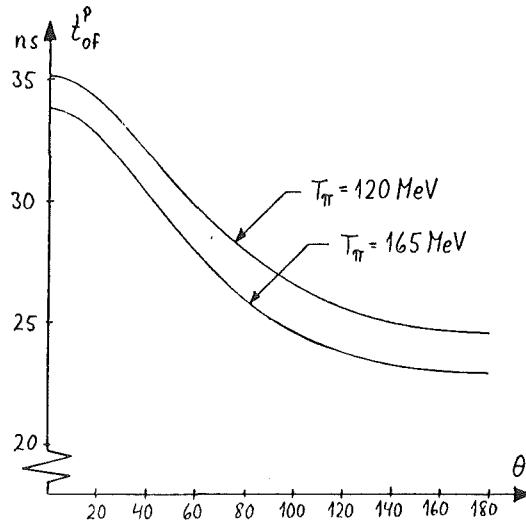


Figure 5.8. QFA kinematics

The deuterons and the protons respectively are selected in the two-dimensional pulse height versus time-of-flight spectra of the E-counter. See figures 5.1 & 5.2. Figure 5.9 & 5.10 show two-dimensional scatterplots, pulse height of selected particle in E-counter versus time-of-flight of the related particle to TOF-counter.

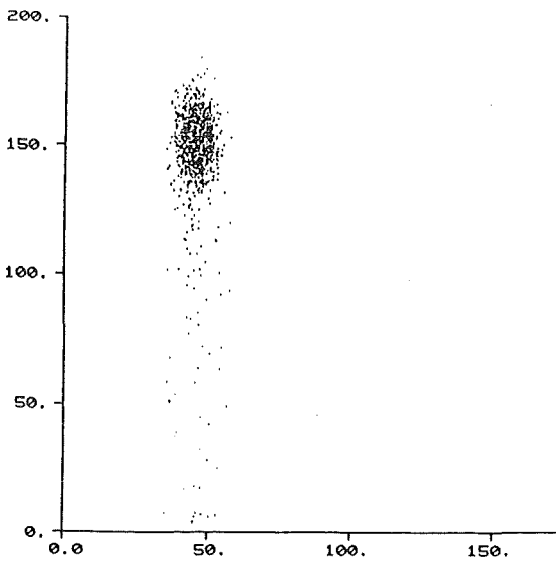


Figure 5.9

π^- run: Pulse height of deuterons vs. time-of-flight of neutrons.

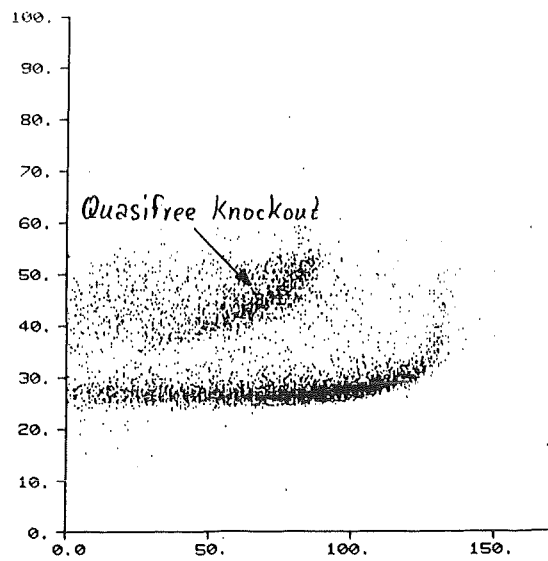


Figure 5.10.

π^+ run: Pulse height of protons vs. time-of-flight of protons.

The difference $t_{of} - t_{Mean}$, the *delay*, is composed of two contributions, one from the left and one from the right side:

$$delay_L + delay_R = 2 \times delay$$

and

$$t_{of} = \frac{t_{of}^L + t_{of}^R}{2}$$

where

$$t_{of}^L = (k_L - k_L^{LED}) \cdot c_L + delay_L, \quad t_{of}^R = (k_R - k_R^{LED}) \cdot c_R + delay_R$$

We shift the t_{of} -spectra of the left and the right side relative to each other by varying the repartition between the two contributions, keeping the sum constant. The left-right time difference is confined to an interval corresponding to the effective propagation time difference in the counter ($\simeq 24$ ns, see figure 4.7b). Thus, we are able to centralize this interval around a zero time difference by changing the repartition. Figure 5.11 shows the left-right distributions for the first layer of the TOF-counter.

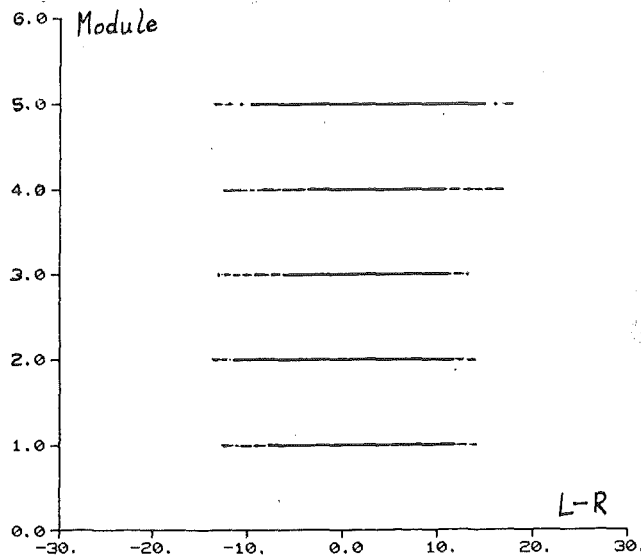


Figure 5.11 Time difference left-right ($delay_L = delay_R$)

5.2.6. ACCEPTANCE

We calculate the acceptance of our experiment by a Monte Carlo Method assuming three-body phase space only [106]. The procedure is facilitated by the fact that the density of states in the Dalitz plot [m_{12} vs. m_{23} invariant masses] is constant. Figure 5.12 show the result for $T_\pi=120$ MeV and $\theta=54^\circ$.

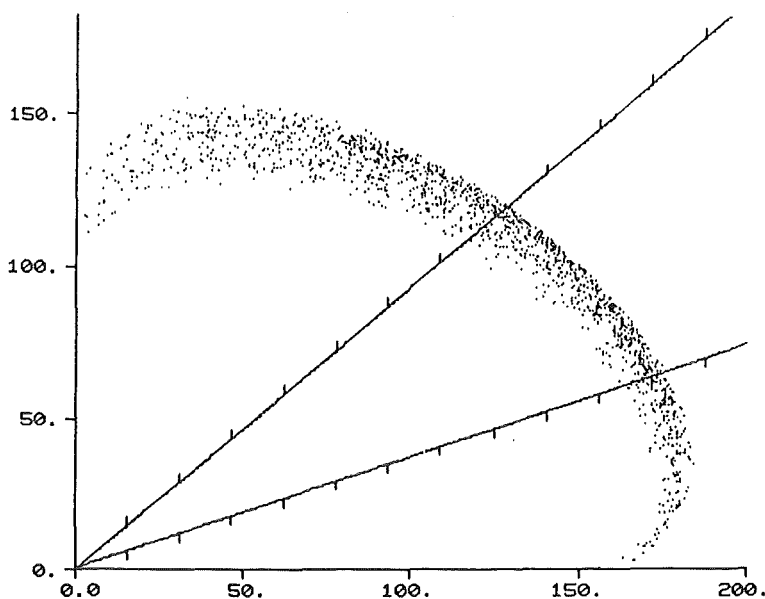


Figure 5.12.

An acceptance scatterplot with cut corresponding to QFA events.

The acceptance weight of the coincidence experiment is given by the total number of *events* distributed over 4π solid angle, $N(4\pi)$, divided by the number of points in the scatterplot, $N(d\Omega)$. In order to obtain the acceptance weight per steradian, G , we divide it all by 4π :

$$G = \frac{1}{4\pi} \times \frac{N(4\pi)}{N(d\Omega)}$$

If events in a specific kinematical region are looked for, e.g. QFA events, we apply the same cut on the acceptance scatterplot as on the scatterplot of the real events.

CHAPTER 6: RESULTS & CONCLUSIONS

6.1. THE ISOSPIN RATIO, R

We present the energy of the particle detected in the E-counter module versus the energy of the correlated particle detected in the TOF-counter. The energy of the latter is obtained through the time-of-flight. Results from the measurement at $T_\pi=120\text{MeV}$ with the old TOF-counter are shown in figures 6.1 and 6.2 below. Figure 6.1 shows only data from E5 whereas figure 6.2 contains the data from all 12 modules.

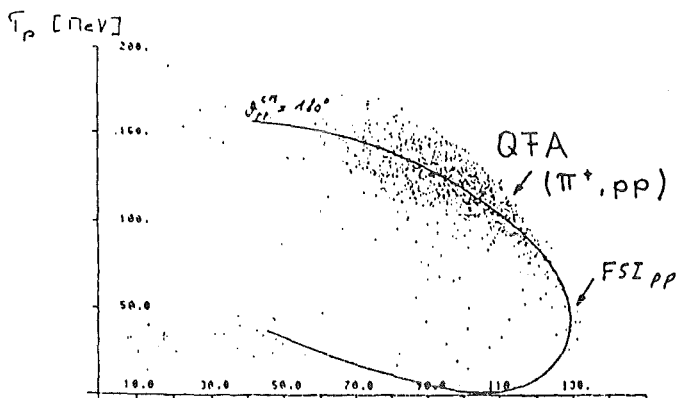


Figure 6.1.

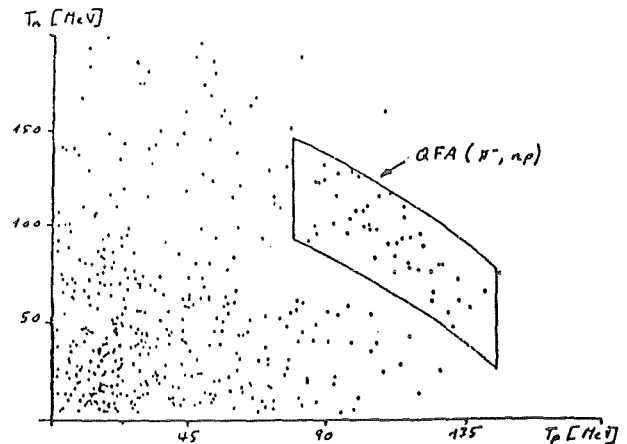


Figure 6.2.

Two-dimensional plot T_p vs. T_p (lab. system).

Two-dimensional plot T_p vs. T_n (lab. system).

The data from the reaction ${}^3\text{He} \rightarrow \text{ppp}$ exhibit a very pronounced enhancement in the region of quasifree absorption. This corresponds to the absorption on a $T=0$ nucleon pair. Because of the suppression of the $T=1$ absorption and the lower detection efficiency for neutrons compared to protons (π^-, np)-measurements generally involve much more experimental difficulties. Nevertheless, our data in figure 6.2 show significant $T=1$ quasifree absorption. Figures 6.3 and 6.4, on the next pages, show the corresponding data from the measurement at $T_\pi=165\text{MeV}$ of June/July 1983. The quasifree region was determined in the π^+ -run and a cut applied. The same cut was applied in the π^- -run and the number of events in the selected region was determined for both runs.

T_π MeV	θ^{LAB}	Neutron Detection Efficiency	Beam	Activation ϵ	Full Target		Empty Target	
					Beam Monitor rate/ 10^9	QFA Events	Beam Monitor rate/ 10^9	QFA Events
120	75°	7.0 ± 0.5%	π^+ /Main	-	16.9	5576	13.1	21
			π^- /Main	-	19.3	11	23.7	1
			π^- /Para.	-	78.4	27	92.0	0
	54°	15 ± 1%	π^+ /Main	0.86	3.52	2240		
			π^- /Main	0.96	74.0	185		
			π^+ /Main	1.11	3.8	2100		
π^- /Main			0.995	129	235			
165								

Table 6.1. The final data from experiment.

Table 6.1 show the data from the full and the empty target measurements. During the first measurements the activation method was not developed and we used the π -signature as a measure of the pion flux. This rate has later been found to agree within 8% with the activation measurement at 120MeV.

During the first period of October 1982 we had to resort to a parasitic run in order to get enough π^- data. We normally use the parasitic beamtime only for adjusting the equipment since the beam is less well focused on the target and in relation to the telescope rate less pions are absorbed in the target. We normalized the parasitic run to the main user run by counting deuterons from the reaction $\pi^-^3\text{He} \rightarrow \text{nd}$. The number of deuterons found in E6 and E7 were 64 for the parasitic and 29 for the main user run, i.e. during the parasitic run we measured $2.21 \pm .5$ times as much as during the main user run.

Two kinds of background have to be considered in the region of interest:

- (a) *events not originating in ^3He .*
- (b) *events from ^3He which are not due to quasifree two-nucleon absorption.*

Background of type (a) as determined by empty target measurements have proven to be negligible, even for (π^-, np) -data. Therefore, the results of the empty target measurements have not been quantitatively evaluated for all data and thus, are not always included in the tables.

Concerning the background of type (b) three-body absorption has been considered by Ashery et al.[40]. We have simulated our experiment with respect to three-body phase space by means of the Monte Carlo program of last section, taking the acceptance into account. In this simulation we find a variation in the event density of less than a factor of 1.4 between the kinematical region of the

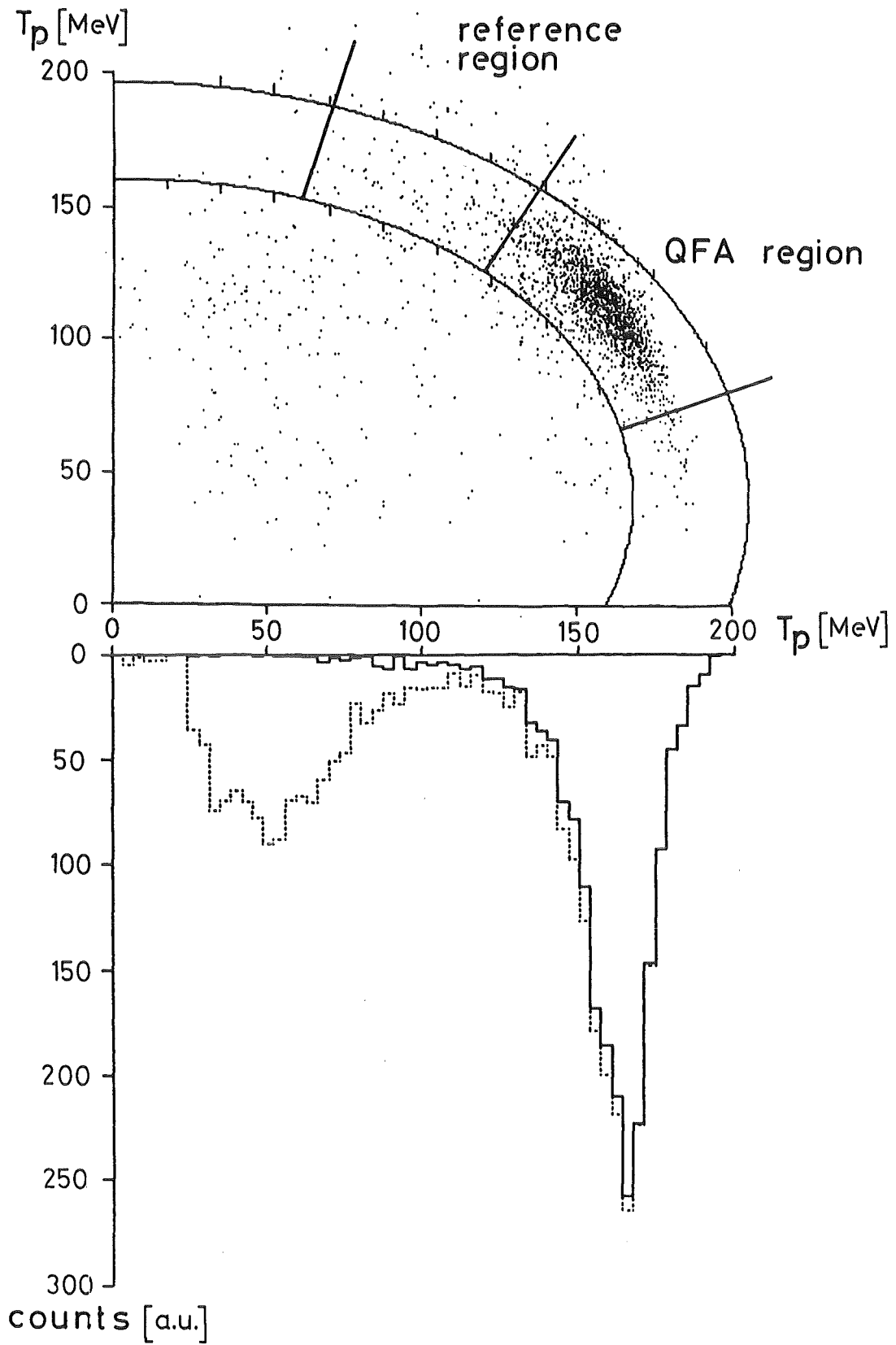


Figure 6.3. Two-dimensional plot T_p vs. T_p (LAB-system) for $T_{\pi^+}=165\text{MeV}$

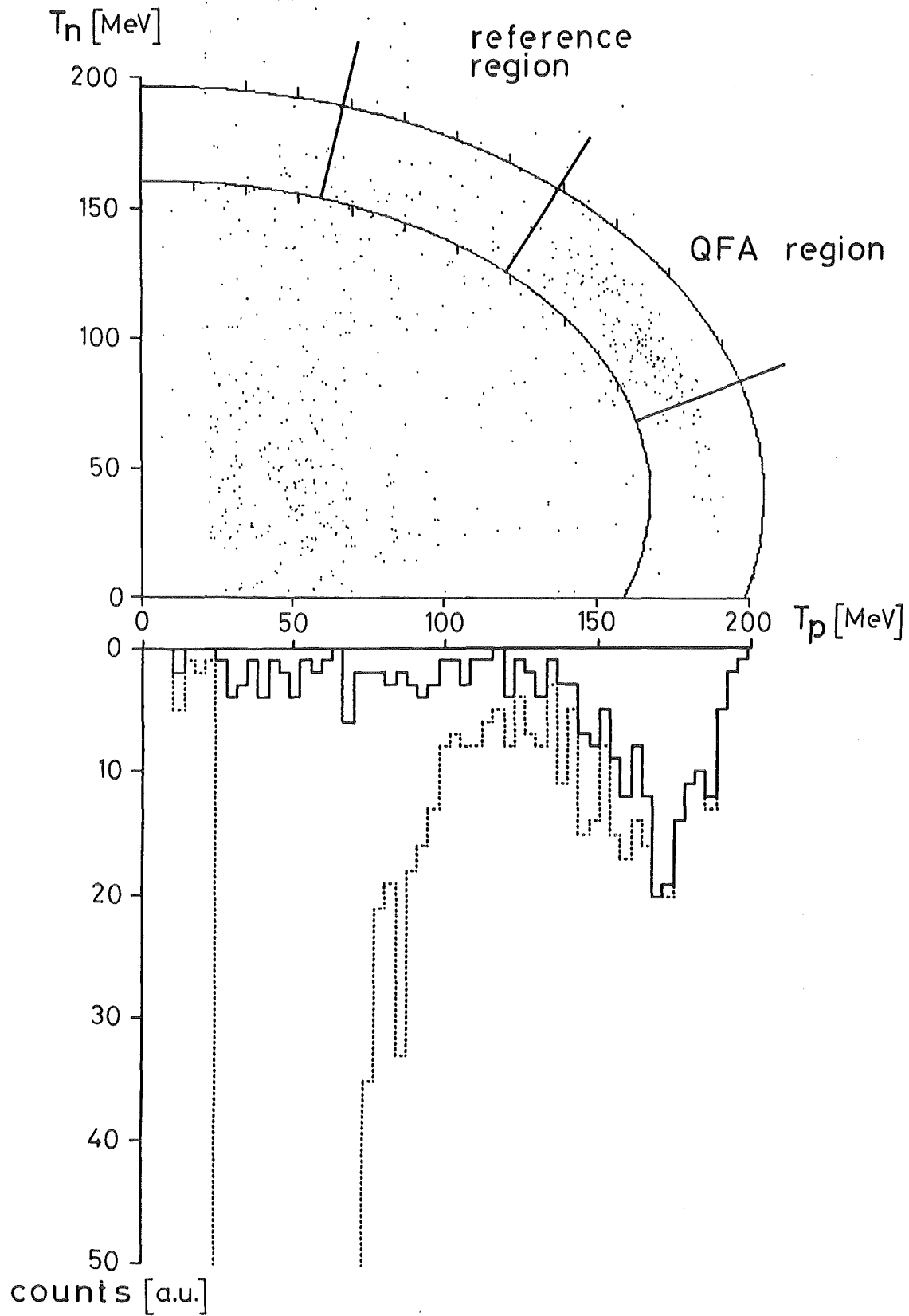


Figure 6.4. Two-dimensional plot T_n vs. T_p (LAB-system) for $T_{\pi^-} = 165$ MeV

quasifree peak and a reference region. The reference region is marked in figures 6.3 and 6.4. It covers relative CM-angles near 180° and proton energies between 70MeV and the lower edge of the quasifree region. The number of events obtained in the measurement in the reference region can be judged from figures 6.3 and 6.4. These numbers are, however, an upper limit, because of the possible existence of events due to final state interaction (two nucleons with small relative momenta as observed by Gotta et al. [44]).

The neutron detection efficiency can be taken to be constant over the whole quasifree region. In the measurement using the old TOF-counters the efficiency was 7% which improved to 15% for the later experiments using the new TOF-counter.

In the case of (π^-, np) the detected nucleons are of different charge state and can not be interchanged. We are determining the cross section for detecting a proton in the E-counter and a neutron in the TOF-counter and not vice versa. In the case of (π^+, pp) the emitted particles are indistinguishable and the cross section if we could label the protons would be one half of the actual measured cross section. In order to treat these two processes on the same footing we will reserve the term "cross section" for the value we would get if the emitted particles were distinguishable. Therefore we introduce the term "yield", Y , which corresponds to the measured quantities.

We have

$$\sigma(\pi^-, np) = Y(\pi^-, np)$$

whereas

$$\sigma(\pi^+, pp) = \frac{1}{2} \cdot Y(\pi^+, pp)$$

Upon considering this aspect we calculate the ratio R

$$R = \frac{\sigma(\pi^+, pp)}{\sigma(\pi^-, np)} = \frac{1}{2} \cdot \frac{Y(\pi^+, pp)}{Y(\pi^-, np)} = \frac{\eta}{2} \cdot \frac{(\pi^+, pp)}{(\pi^-, np)}$$

where η is the neutron detection efficiency

and $(\pi, NN) = \frac{\text{QFA-Events}}{\text{Pion-Rate}}$

The resulting values are listed in table 6.2.

T_{π} MeV	θ^{LAB}	π^+/π^-	Pion Rate $\times 10^9$	Number	Normalized to the π^-_{Full} -rate	Pion Rate $\times 10^9$	Number	Normalized to the π^-_{Full} -rate	QFA-Events Full - Empty	$\frac{(\pi^+, pp)}{(\pi^-, np)}$	R
120	75°	π^+	17.7	5576	20440 ± 3184	13.1	21	99.3 ± 15.5	20340 ± 3200	635 ± 237	22.2 ± 8.3
		π^-	62.0 ± 9.7	38	38 ± 5	23.7	1	3.0 ± 3.0	35 ± 8		
	54°	π^+	4.09	2240	42200					228 ± 70	17.1 ± 5.3
		π^-	77.1	185							
165		π^+	3.42	2100	79800					340 ± 100	25.5 ± 7.5
		π^-	130	235							

Table 6.2 Results

6.2. DIFFERENTIAL CROSS SECTIONS

The number of particles dN emitted in a solid angle $d\Omega$ can be written as:

$$dN = n \cdot \frac{\rho}{m} \cdot \frac{d\sigma}{d\Omega} \cdot d\Omega \quad (6.1)$$

where n = the flux of incident particles, [s^{-1}]

ρ = the surface density [g/cm^2]

m = the mass of a 3He atom [g]: $m = A(^3He)/N_A$ with

A = the molar weight of a 3He atom, 3.00g/Mol

N_A = Avogadro's number, $6.022 \cdot 10^{23}$ /Mol

According to eq.(3.4) $n = \frac{n_s}{\epsilon}$ where n_s is the beam monitor rate and ϵ is the proportionality-constant determined in the activation measurement, section 3.2.3.

The CM differential cross section is given by

$$\left(\frac{d\sigma}{d\Omega} \right)_{CM} = \frac{\epsilon \cdot dn}{n_s} \cdot \frac{A}{N_A \cdot \rho} \cdot \frac{f(p_{\pi}, \theta^{LAB})}{d\Omega^{LAB}} = \frac{\epsilon \cdot dN}{n_s} \cdot \frac{A \cdot G}{N_A \cdot \rho} \quad (6.2)$$

where $f(p_{\pi}, \theta^{LAB})$ is the Jacobian and G the acceptance weight.

G is obtained by means of the procedure of section 5.2.6.: We apply the same cut on the acceptance scatterplot as was used to select the QFA events. Table 6.3 shows the acceptance weight.

T_π	θ^{LAB}	$N(4\pi)$	$N(d\Omega)$	$N(QFA)$	$G = \frac{1}{4\pi} \cdot \frac{N(4\pi)}{N(QFA)}$
120MeV	54°	2·10 ⁶	1413	492	323.5
165MeV	54°	2·10 ⁶	1396	541	294.2

Table 6.3. The acceptance weight G.

The density δ of the liquid ³He is temperature dependent. Taking the uncertainty of the target temperature into account the density at our temperature of about 2.8K is known with a 2% accuracy [96]:

$$\delta = 0.069g/cm^3 \pm 2\% = (0.069 \pm 0.0015)g/cm^3$$

For the data considered in this section, the incident pion beam had a horizontal width of about 3cm with a standard deviation of 0.5cm. Figure 3.7b shows the target cell. It is 18cm long, 2.0cm thick at the ends and 2.9cm in the middle and was turned 58° relative to the beam axis.

The average target thickness can be determined with 3% accuracy

$$d = 5.3cm \pm 3\% = 5.3 \pm 0.2cm$$

This yields the surface density

$$\rho = .366g/cm^2 \pm 6\% = (0.366 \pm 0.022)g/cm^2$$

The differential cross section can now be written

$$\left(\frac{d\sigma}{d\Omega} \right)_{CM} = \frac{N(QFA)}{n_s/\epsilon} \cdot G \cdot \sigma_0 \quad \text{where} \quad \sigma_0 = \frac{A}{N_A \cdot \rho} = (13.66 \pm .82)barn \quad (6.3)$$

The quantities necessary to determine the differential cross sections and the results are summarized in table 6.4.

T_π MeV	π^+/π^-	Pion Rate $\frac{n_s}{\epsilon}, \times 10^9$	QFA-Events N(QFA)	G /Steradian	Average Efficiency η	$\left(\frac{d\sigma}{d\Omega} \right)_{CM}^{\theta^{LAB}=\theta^*}$ mb/sr	θ^{CM}
120	π^+	4.09	2240	323.5	100%	1.2 ± 0.4	64.4°
	π^-	77.1	185	323.5	15%	(71 ± 22)·10 ⁻³	
165	π^+	3.42	2100	294.2	100%	1.2 ± 0.4	65.9
	π^-	130	235	294.2	15%	(48 ± 15)·10 ⁻³	

Table 6.4. The differential cross sections.

Due to the great variety of cuts which are necessary to clean the raw data, we have to be very careful not to lose good events. We have checked this to a certain degree but this work is still in progress. Therefore, *the calculated differential cross sections of table 6.4 are only of preliminary character. The major results of this work are the isospin ratios.*

The differential cross section for just one angle is not very informative. Also, the comparison between the data for the different energies is aggravated by the fact that the CM angles vary with the pion energy. The goal of the measurements described here is to determine the angular dependence of the differential cross section and thereby the total cross section. Since the data analysis has not yet been completed the values for only one LAB angle of the run of June/July 1983 are presented here. These data points can be compared with very recently published corresponding data at a different energy, $T_\pi=65\text{MeV}$, [50]. Also preliminary unpublished data at 85 and 165MeV are available for comparison, [104]. These data have been fitted with Legendre polynomials:

$$\left(\frac{d\sigma}{d\Omega} \right)_{\theta^{CM}} = A_0 \cdot P_0(\cos\theta^{CM}) + A_1 \cdot P_1(\cos\theta^{CM}) + A_2 \cdot P_2(\cos\theta^{CM}) \quad (6.4)$$

where $P_0(x)=1$, $P_1(x)=x$ and $P_2(x)=(3x^2-1)$ and

$$\sigma = 2\pi \int_{-1}^1 \left(\frac{d\sigma}{d\Omega} \right) d(\cos\theta) = 4\pi \cdot A_0 \quad (6.5)$$

T_π MeV	Process	Yield			$\frac{\sigma_{Total}}{4\pi \times A_0}$ mb	R
		A_0 $\mu b/sr$	A_1 $\mu b/sr$	A_2 $\mu b/sr$		
65	(π^+, pp)	2064 ± 76	-	2078 ± 210	12.9 ± 0.6	15.5 ± 1.6
	[50] (π^-, np)	67 ± 4	-48 ± 9	99 ± 9	0.84 ± 0.05	
85	(π^+, pp)	2158 ± 100	-	2356 ± 170	13.6 ± 0.6	16.1 ± 1.7
	[103] (π^-, np)	68 ± 4	-54 ± 4	111 ± 5	0.85 ± 0.05	
165	(π^+, pp)	2600 ± 200	-	3200 ± 500	16.3 ± 1.3	34.6 ± 8.3
	[103] (π^-, np)	39 ± 6	-	60 ± 50	0.49 ± 0.08	

Table 6.5. Legendre polynomial fits of differential crosssection from [50,104].

Table 6.5 and figure 6.5 show their respective results together with our data points. The coefficients of table 6.5 are given for the yield and has to be divided by two in case of (π^+, pp) in order to obtain the cross section.

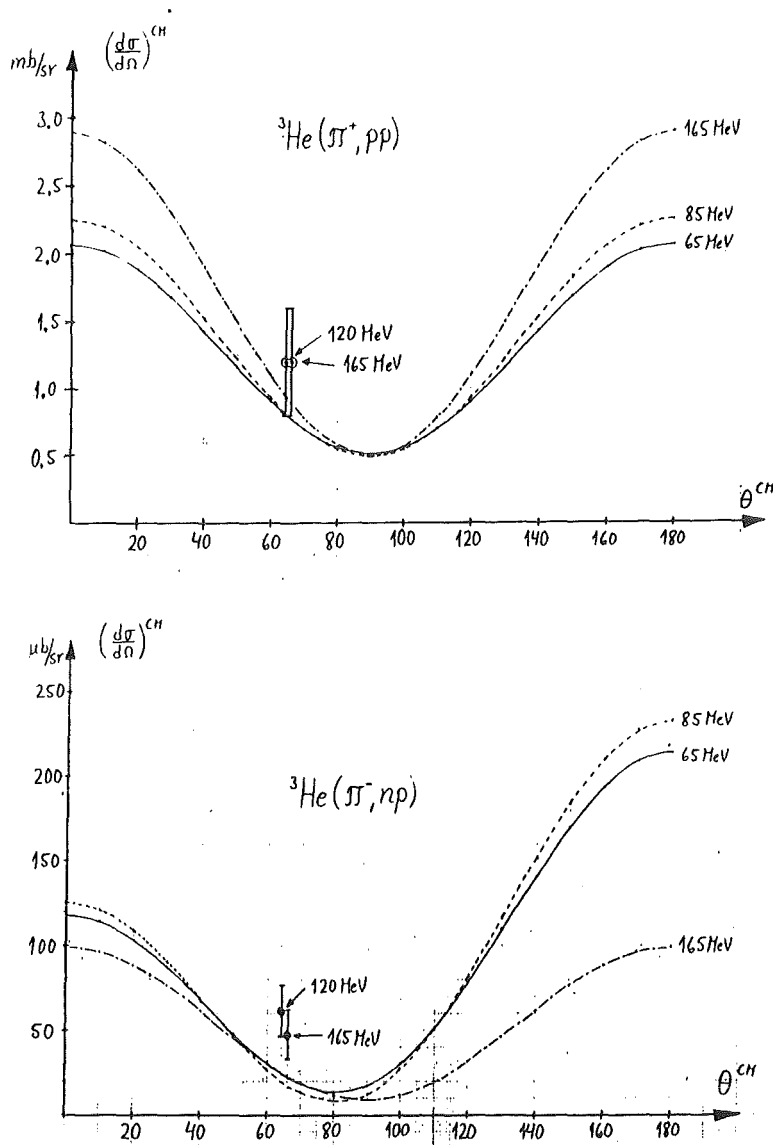


Figure 6.5. Differential cross sections from [50,104] compared with our data

For both polarities the agreement between our data points and the polynomial fits of references [50,104] is satisfactory, our results being somewhat higher.

For ${}^3\text{He}(\pi^-, pn)$ at $T_\pi=65$ and 85 MeV the angular distribution shows significant asymmetry around 90° . This is a signature of interference of even and odd partial waves. As mentioned in section 2.3. this cross section is composed of contributions from the transition from an initial nucleon pair with isospin $T=1$ to a final nucleon pair with either $T=1$ or 0, respectively σ_{11} or σ_{10} . This asymmetry can not, however, be caused by an interference between these two contributions, since σ_{10} first emerges at energies above $\simeq 250$ MeV (cf. figure 2.2). Also, for the σ_{11} contribution any interference is hard to explain because the final 2N systems all have the same parity.

In order to be able to calculate the integrated cross section for our data points we need to know the angular distribution, i.e. the relation between the coefficients A_0 , A_1 and A_2 of eq. 6.4. Following the argument given above we assume A_1 to be zero also for the π^- data. In table 6.5 the ratio $A_0:A_2$ is about 1 for π^+ . Within the errors this is also compatible with the π^- data at 165MeV. From this the A_0 and thereby the integrated cross section can be calculated, cf. table 6.6.

T_π MeV	θ^{CM}	π^+/π^-	$\left(\frac{d\sigma}{d\Omega}\right)$ mb/sr	$A_0 = \frac{2 \cdot (d\sigma/d\Omega)}{1 + 3\cos^2\theta}$	$\sigma = 4\pi A_0$	R
120	64.4°	π^+	1.2 ± 0.4	1.5 ± 0.5	18.8 ± 6.3	20.1 ± 11.7
		π^-	$(71 \pm 22) \times 10^{-3}$	$(91 \pm 28) \times 10^{-3}$	1.14 ± 0.35	
165	65.9°	π^+	1.2 ± 0.4	1.6 ± 0.5	20.1 ± 6.3	30.6 ± 17.4
		π^-	$(48 \pm 15) \times 10^{-3}$	$(64 \pm 20) \times 10^{-3}$	0.80 ± 0.25	

Table 6.6. Estimated integrated cross sections from our data.

Figure 6.6 shows the absorption on $T=0$ nucleon pairs in ^3He . The data points are taken from table 6.5 ([50,104]) and table 6.6. The cross section for absorption on the only free $T=0$ pair, the deuteron [16], is shown as comparison. Taking the number of np-pairs with $T=0$ in a ^3He nucleus into account we have multiplied the deuteron cross section by 1.5 (cf. eq.(2.2)). We see that the ^3He -data is compatible with the cross section for a deuteron although the average nucleon distance in a ^3He nucleus is much smaller than in deuteron, i.e. no dependence on the nuclear density can be found.

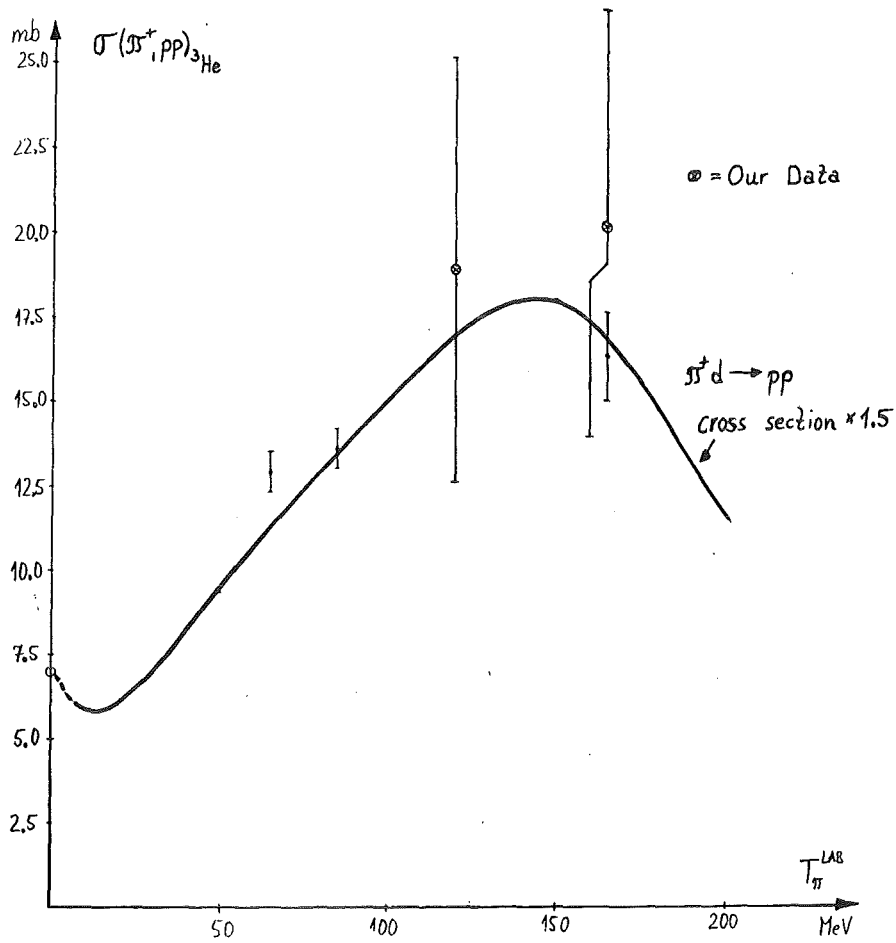


Figure 6.6. Total cross sections for absorption on $T=0$ NN-pairs in ^3He .

Figure 6.7 shows for the first time the energy dependence of the cross section for absorption on a $T=1$ nucleon pair. We know the isospin ratio for absorption at rest ($R=8$, [44]). Since a $T=0$ nucleon pair behaves like a deuteron we use the deuteron cross section together with the isospin ratio at rest to obtain the cross section for absorption on a $T=1$ nucleon pair at rest. Hence, in addition to the values of references [50,104] and our two points we also have a value for stopped pions.

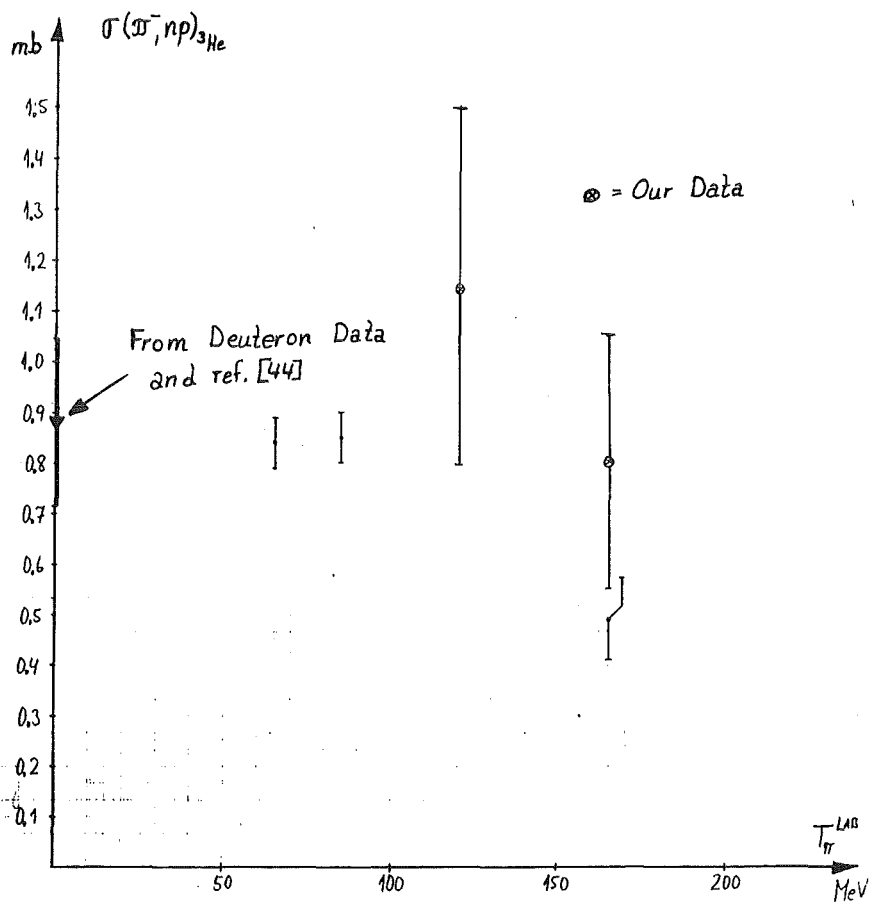


Figure 6.7. Total cross section for absorption on $T=1$ NN-pairs in ^3He .

The cross section for absorption on a $T=1$ nucleon pair shows no significant energy dependence over the investigated energy region.

6.3 DISCUSSION AND CONCLUSIONS

Figure 6.7 shows theoretical predictions and experimental data of the isospin ratio available at the end of 1983. It also contains the three data points of this work.

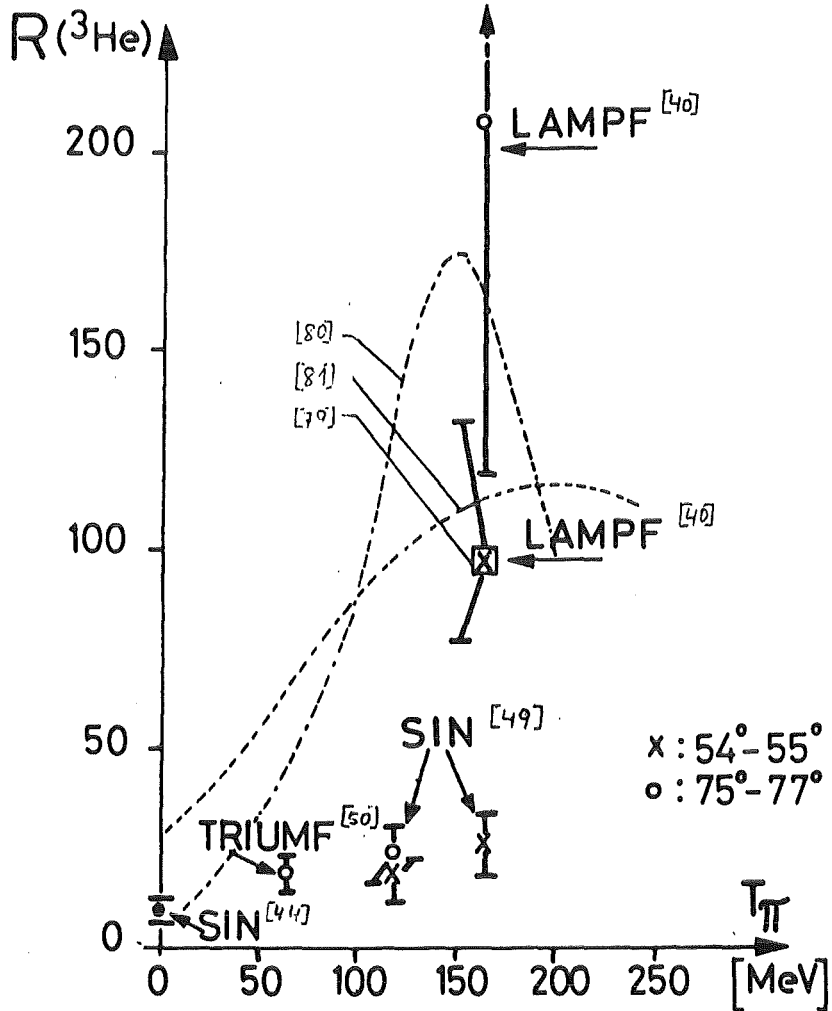


Figure 6.7. The isospin ratio R.

Our ratios were far lower than the LAMPF data and the theoretical predictions, the predictions being issued shortly after the LAMPF data. However, recently new data has been published [50], old data corrected [104] and theoretical predictions upgraded [105], yielding to a more coherent picture of the isospin ratio. See figure 6.8.

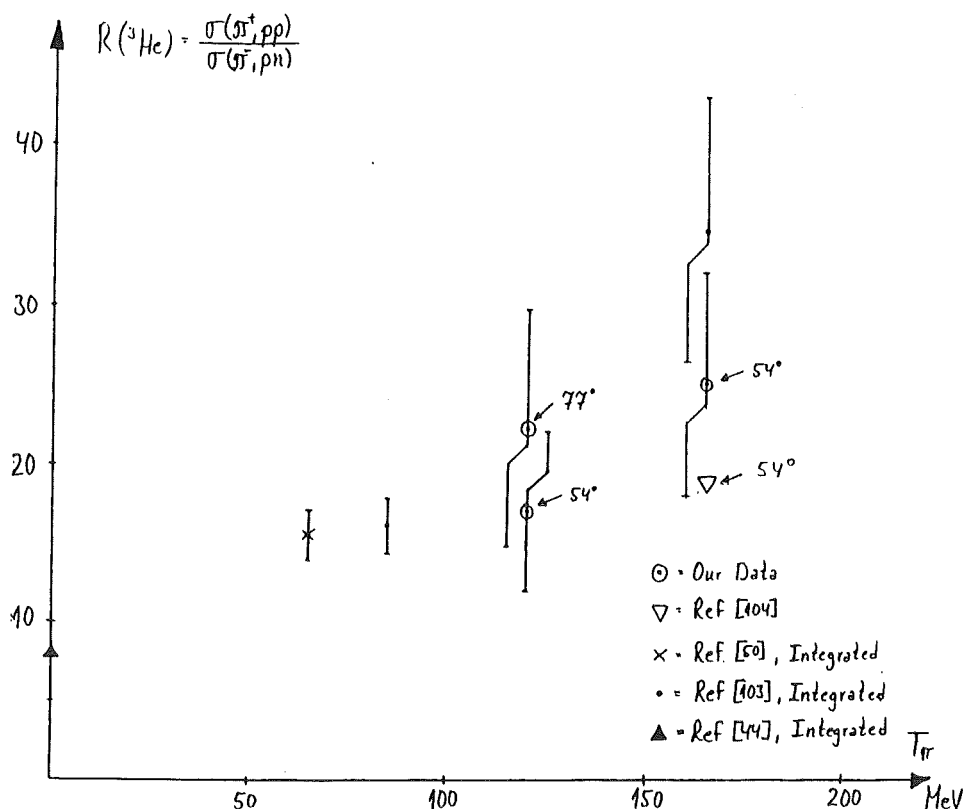


Figure 6.8. The latest data on the isospin ratio.

The general trend shows an isospin ratio of about 20 in the resonance region. This ratio is much larger than the $\frac{13}{2}$ predicted under the assumption of isospin symmetry and dominance of a Δ formation in the intermediate state (cf. section 2.3.). This prediction is made without considering the angular momentum of the pion and the dominance of p-wave pions in the resonance region. Indeed, considering a ΔN configuration in the intermediate state, absorption of p-wave pions is only allowed on a $T=0$ nucleon pair. In addition such an absorption is the only one leading to an intermediate ΔN state with angular momentum $L_{\Delta N}=0$. A NN pair in a $T=1$ 1S_0 state can absorb $J=0$ and 2 pions, leading to a formation of ΔN intermediate states with $L \geq 1$, which means much smaller amplitudes [81]. Thus, assuming a large fraction of p-wave pions and dominance of a Δ formation the measured size of the ratio can be explained. The suppression of the otherwise dominant Δ -isobar formation increases the sensitivity for other processes that are normally masked. Silbar et al. [81] have included a non-resonant P11 interaction in their calculation of the isospin ratio and found it to be important. The cross section for absorption on a $T=0$ nucleon pair seems to be understood by comparison with the deuteron cross section. However, the ratio of 1.5 between the cross sections points at no dependence on the average nucleon distance, since this is much smaller in ^3He than in deuteron.

The energy dependence of the cross section for absorption on a $T=1$ nucleon pair is presented for the first time. At the present time the mechanism for absorption on a $T=1$ nucleon pair is not understood.

APPENDIX A

DESCRIPTION OF ELECTRONIC UNITS

Symbols used in section 3.3 are listed in table A.1.

All units are updating, i.e. the output is extended if the requirement of the unit (e.g. signal above threshold, coincidence etc.) is fulfilled a second time before the first output returns to zero. Thus, subsequent pulses will be seen by the front end even though an output pulse is still present from the first signals, and these subsequent signals may cause a new output to be generated and added (in time) to the portion of the original output already occurred.

One of the main difficulties in determining the energy through the time-of-flight is to eliminate the so called time walk, t_w . By this we mean the effect that pulses of different amplitudes -- but the same rise time -- cross a discriminator threshold at different times -- small ones later, large ones earlier -- causing the triggering time to shift or *walk*. We are able to considerably reduce the time walk by using so called *constant fraction discriminators*, *CFD's*. The principle of operation of such a device is shown in figure A.1.

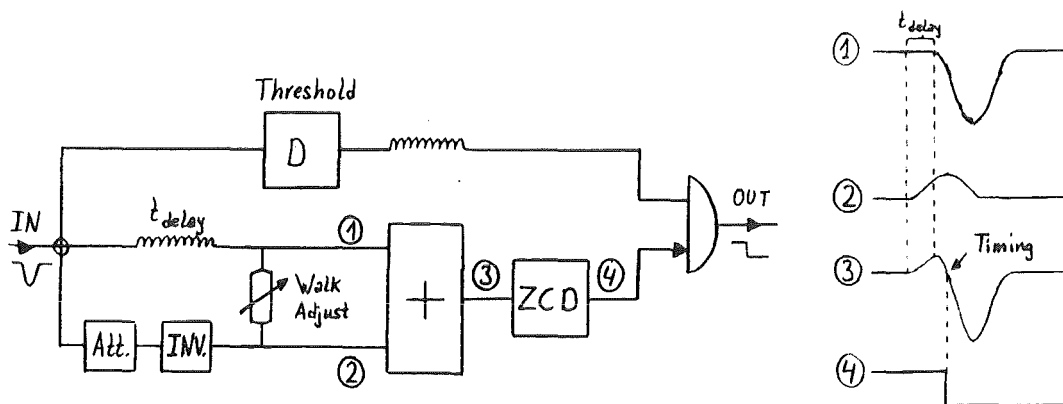


Figure A.1. Principle of operation of a CFD.

The input pulse is split into three parts. One part is attenuated and inverted and one part is delayed a time t_{delay} . These two signals are added and fed into a zero-crossing discriminator, ZCD. The timing of this unit is determined by the time the leading-edge passes zero, cf. table A.1. The last part is fed into a usual leading-edge discriminator determining the threshold. These signals are taken in a coincidence where the timing of the ZCD prevails.

In order to derive the timing information from a fraction of the amplitude of the input pulse, the maximum of the attenuated has to cross the delayed pulse at the particular selected fraction. This condition leads immediately to the relation

$$t_{delay} = t_{rise} \times (1.0 - fraction)$$

using the idealized pulse shapes of figure A.2.

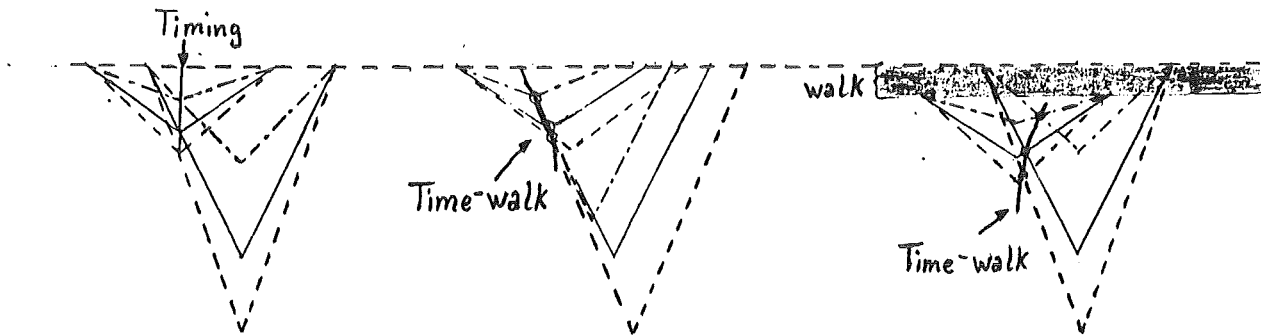


Figure A.2a.
Principle

Figure A.2b.
Different risetime

Figure A.2c.
Zero Offset

Zero offset in the ZCD is very important for proper operation of the CFD. If it is not well adjusted, time walk will result as can be seen in figure A.2c.

Still, however, even properly adjusted CFD's have a small time walk, t_{walk} . If we determine this time walk, $t_{walk} = t_{walk}(Ph)$, for each CFD separately we can later use pulse height information to reduce the time walk further. This has been done for all 70 CFD's. The results are shown in figure 5.4.





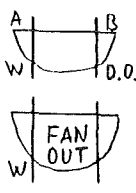
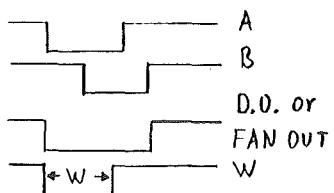

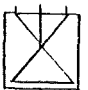



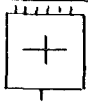
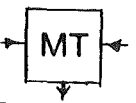
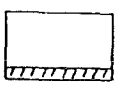
Symbol	w and d stands for width and delay respectively
	Leading Edge Discriminator; the leading edge determines the timing.
	Refreshing Discriminator; to refresh logical signals.
	Zero Crossing Discriminator; the zero-crossing determines the timing.
	Constant Fraction Discriminator; See description opposite.
 	<p>The direct Out (D.O.) and FAN OUT (F.O.) outputs are the direct equivalence to the logical "OR". The width-output is the same signal after passing an additional pul-seshaper stage.</p>
	AND; D.O. and w have the same meaning as by OR.
	Active Split
	Inverter (not logical); Impulse transformer
	Timing Unit ("DELAY trigger")
	TTL → NIM Converter or vice versa
	Linear FAN-IN (ADDER)
	Mean Timer, cf. page 53
	CAMAC-Units; ADC's, TDC's, PU's, Coincidence Buffer etc.

Table A.1. Symbols of Electronic Units

APPENDIX B

PREPARATORY TEST OF THE TOF-COUNTER WITH COSMIC RAY MUONS

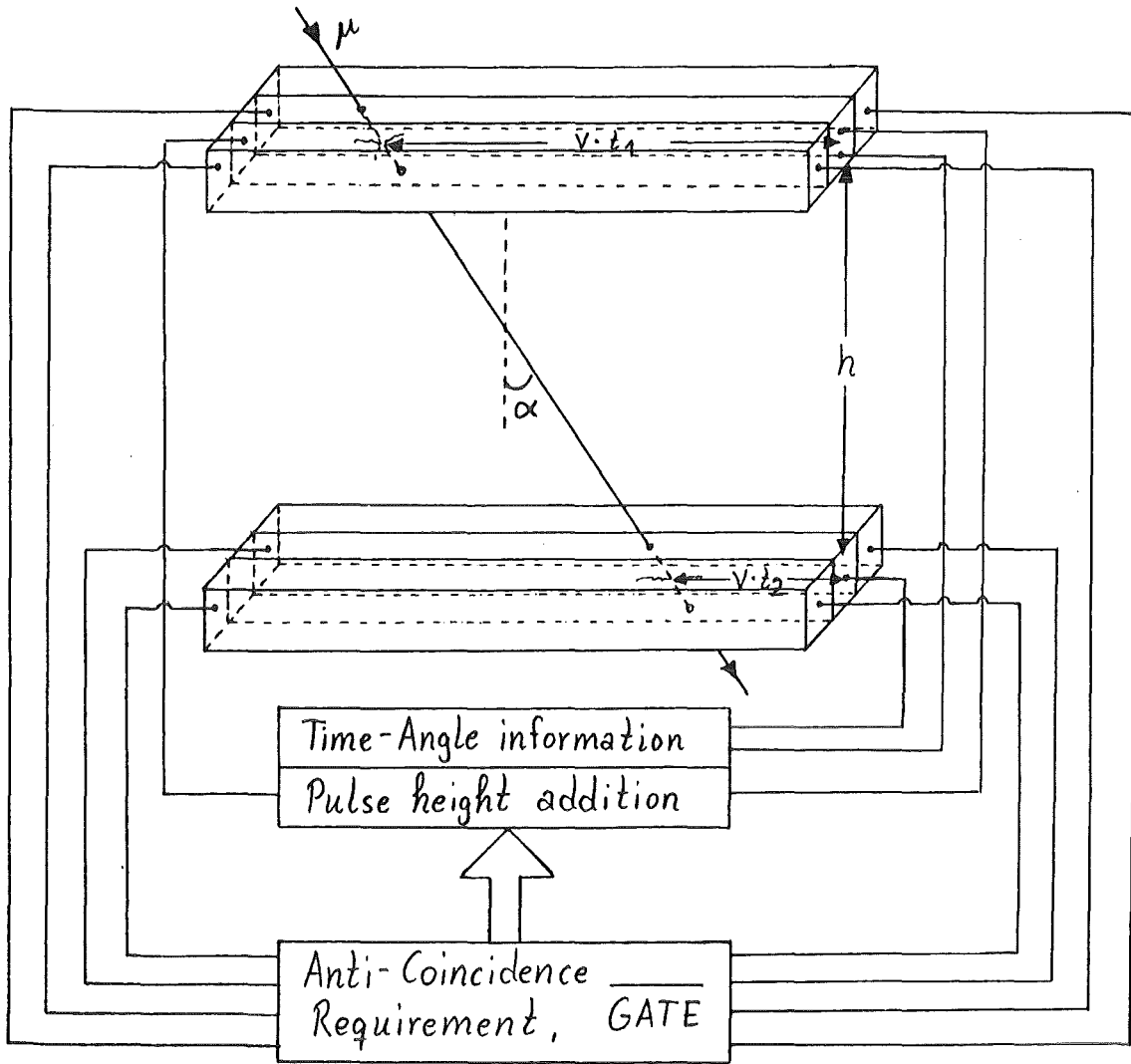
Previous measurements of the angular distribution of the muons at sea level have been found to satisfy the relation

$$I(\alpha) = I_0 \cdot \cos^n \alpha, \quad \alpha = \text{angle of incidence}$$

With increasing angle the distance through the atmosphere increases and the probability for muon decay rises. However, the probability that the strongly interacting particles, notably the pions, decays increases with the angle since the density gradient decreases. Since the whole energy is transferred onto the decay-products ($\pi \rightarrow \mu\nu$) the exponent n decreases with the energy.

In the course of a semester work [9] the new TOF-counter was tested with cosmic ray muons and the directional distribution of the muons was measured. The counter was aligned with the east-west direction. It was demanded a coincidence between the signals of two rods in the middle layer, situated a vertical distance h from each other. We can eliminate the other important component of the radiation, the electrons, by requiring that none of the neighboring outer rods detect a signal (anti-coincidence). These are interacting with the scintillator molecules producing shower electrons some of which will certainly be detected by the neighbouring rods and therefore produce a veto-signal. The muons, in contrast, have too small a reaction cross section with matter to cause anything but ionization.

The angle of incidence can be calculated out of the time difference between the signals from the photomultipliers on the right side. See figure B.1.



$$\Delta t = t_1 - t_2, \quad \tan \alpha = \frac{v(\Delta t - t_{flight})}{h}$$

$$t_{flight} = \frac{h}{c} \sqrt{1 + \tan^2 \alpha}$$

Figure B.1. Set-up

The position of 0° is determined by assuming that the same number of events are coming from the east as from the west branch. After correcting for absorption in the counter and in the ceiling, the data-points (cf. figure B.2) can be fitted by

$$I(\alpha) = 0.084 \cdot \cos^{2.15} \alpha \quad [s^{-1} sr^{-1} cm^{-2}]$$

The statistical errors for 0° , 40° and 60° are indicated.

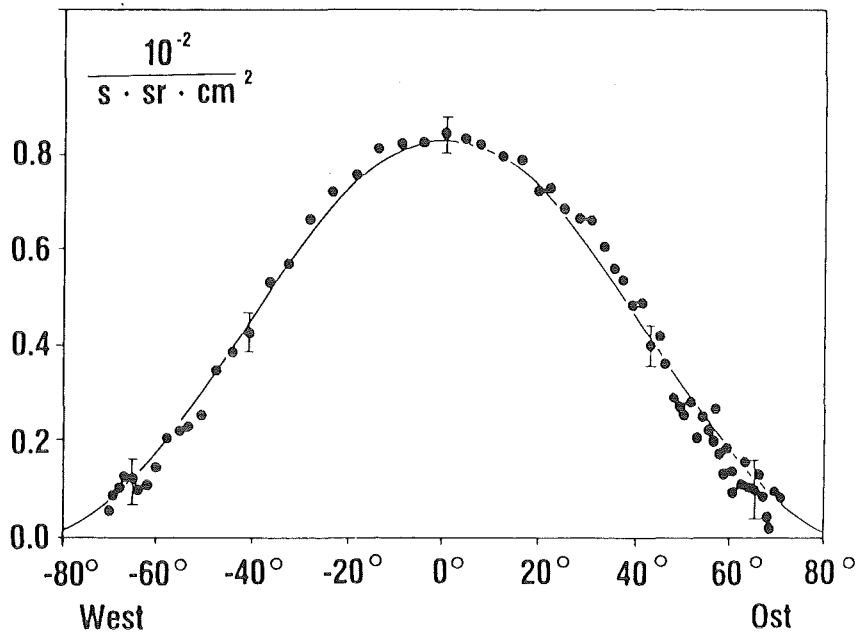


Figure B.2. Angular distribution of cosmic ray muons

The shape of this distribution as well as the absolute value of the measured intensity is in excellent agreement with the data of Alkhofer et al. [102].

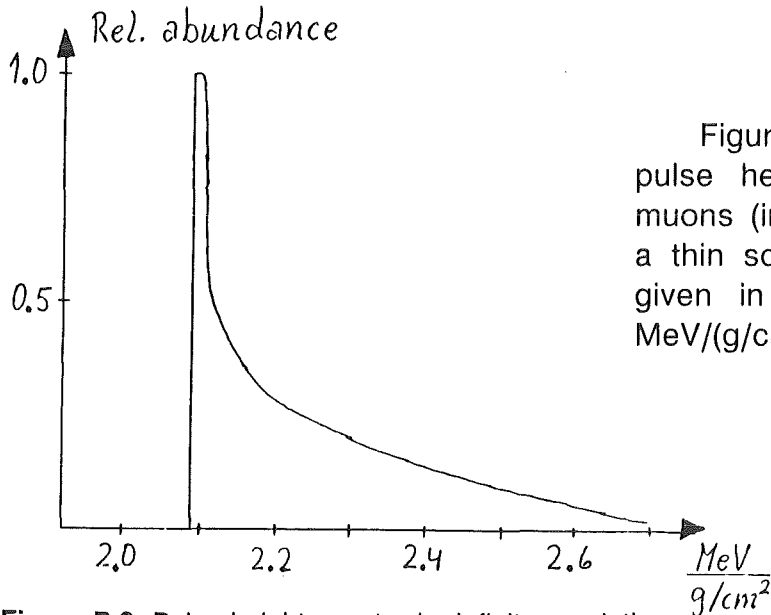


Figure B.3 shows the theoretical pulse height spectra of cosmic ray muons (infinite resolution) produced in a thin scintillator. The pulse height is given in units of ionization density, $\text{MeV}/(\text{g}/\text{cm}^2)$.

Figure B.3. Pulse height spectra by infinite resolution

There is a strong enhancement at the minimal ionisation of $2.1 \text{ MeV}/\text{gcm}^{-2}$. In our scintillators which has a density of about $1.0 \text{ g}/\text{cm}^3$ (see table 3.2.) this amounts to an energy deposit of $2.1 \text{ MeV}/\text{cm}$. In figure B.4 the measured energy spectrum of particles incident at 0° is compared with the theoretical spectrum for a finite resolution of 8%.

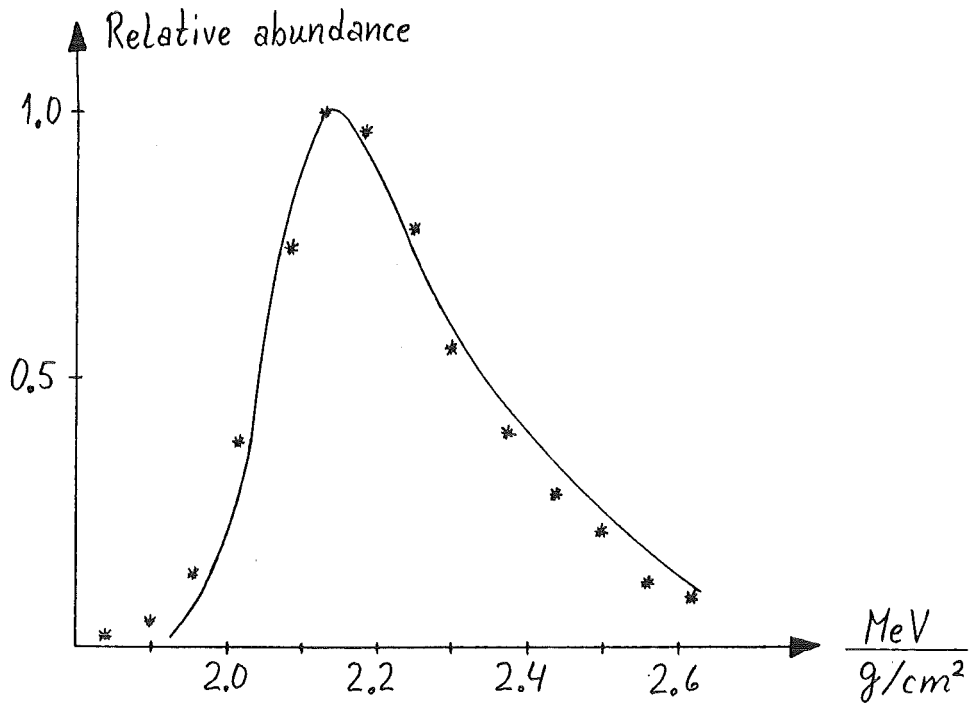


Figure B.4. Cosmic ray spectrum:

Solid line: theoretical prediction with 8% resolution
* : Measured pulse height spectrum

The agreement is very good. We are therefore using the cosmic ray muons to calibrate the light output of the LED's in electron equivalent units, MeV_{ee}. This is treated in section 4.3.

REFERENCES

MAJOR WORKS IN THE GROUP

- [1]: B. Bassallek, "A study of the $(\pi^-, 2n)$ -reaction on nuclei of the 1p-shell", PhD-thesis, University of Karlsruhe, 1977. KFK-report No. 2485.
- [2]: I. Schwanner, "Untersuchung von pionischen röntgenspektren leichter isotopenpaare", PhD-thesis, University of Basel, 1981.
- [3]: D. Gotta, "Untersuchung der Reaktion $\pi^-^3\text{He} \rightarrow \text{pnn}$ mit gestoppten Pionen in einem kinematisch vollständigen Experiment", PhD-thesis, University of Karlsruhe, 1981. KFK-report No. 3226.
- [4]: W. Kowald, "Absorption negativer Pionen aus s- und p-zuständen in ^3He ", PhD-thesis, University of Basel, 1981.
- [5]: M. Dörr, "Pionabsorption an ^7Li ", PhD-thesis, University of Karlsruhe, 1982. KFK-report No. 3429.
- [6]: B. Kober, "Entwicklung und Konstruktion von hochauflösenden, ortsempfindlichen und grossflächigen Neutronenzählern", Diplom-thesis, University of Karlsruhe, 1972. Unpublished.
- [7]: A. Klein, "Teilchentrennung", Diplom-thesis, University of Basel, 1981. Unpublished.
- [8]: P. Weber, "Die relative Häufigkeiten der Reaktionen $\pi^-^3\text{He} \rightarrow \text{dn}$, $\pi^-^3\text{He} \rightarrow \text{t}\pi^0$ ", Diplom-thesis, University of Basel, 1982. Unpublished.
- [9]: K. Sambale, "Messung der Richtungsverteilung der kosmischen Höhenstrahlung", Staatsexamensarbeit, University of Karlsruhe, 1982. Unpublished.
- [10]: M. Steinacher, "Eichung eines Energiezählers mit Hilfe kosmischer Strahlung", Semesterarbeit, University of Basel, 1983. Unpublished.
- [11]: A. Huck, "Untersuchungen an der Reaktion $\pi^-^3\text{He} \rightarrow \text{dn}$ für einen Pionimpuls von 220 MeV/c", Diplom-thesis, University of Basel, 1983. Unpublished.
- [12]: K. von Weimarn, "Pion-absorption an ^3He im Fluge:
Isospinverhältnis: $\frac{d\sigma(\pi^+ \text{np} \rightarrow \text{pp})}{d\sigma(\pi^- \text{pp} \rightarrow \text{np})}$
Diplom-thesis, University of Basel, 1983. Unpublished.
- [13]: Th. Maier, "Nachweis von Neutronen aus pioninduzierten Kernreaktionen", Diplom-thesis, University of Karlsruhe, 1983. Unpublished.

- [14]: U. Mankin , "Bestimmung der Intensität von Pionen-strahlen", Diplom-thesis, University of Karlsruhe, 1983. Unpublished.
- [15]: J. Reich , "Untersuchung der Pionabsorption an ^7Li ", Diplom-thesis, University of Karlsruhe, 1983. Unpublished.

BOOKS and REVIEW ARTICLES

- [16]: D. Ashery, *Experimental Studies of the ΔN Interaction*, Proceedings of the Symposium on Delta-Nucleus Dynamics, Argonne, Illinois (USA), 1983 (to be published).
- [17]: J.D. Bjorken and S.D. Drell, *Relativistic Quantum Mechanics*, McGraw-Hill, 1964.
- [18]: J.D. Bjorken and S.D. Drell, *Relativistic Quantum Fields*, McGraw-Hill, 1965.
- [19]: B.H. Bransden and R.G. Moorhouse, *The Pion-Nucleon System*, Princeton University Press, 1973.
- [20]: E. Byckling and K. Kajantie, *Particle Kinematics*, Wiley, 1973.
- [21]: E.D. Commins and P.H. Bucksbaum, *Weak Interactions of Leptons and Quarks*, Cambridge University Press 1983.
- [22]: A.S. Davydov, *Quantum Mechanics*, Pergamon Press 1976.
- [23]: J.M. Eisenberg and D.S. Koltun, *Theory of Meson Interactions with Nuclei*, Wiley 1979.
- [24]: J. Hüfner, *Pions Interact with Nuclei*, Physics Report 21, No.1(1975)p.1-79.
- [25]: G. Källén, *Elementary Particle Physics*, Addison-Wesley 1964.
- [26]: D.B. Lichtenberg, *Unitary Symmetry and Elementary Particles*, Academic Press 1978.
- [27]: A. Messiah, *Quantum Mechanics I+II*, North-Holland 1961.
- [28]: E.J. Moniz, *Pion-Nucleus Scattering in the Isobar Formalism*, Proceedings of the NATO Advanced Studies Institute on Theoretical Nuclear Physics held at the University of Wisconsin, Madison, Wisconsin, June 12-23, 1978, Plenum Press, New York, 1978, p.603.
- [29]: H.M. Pilkuhn, *Relativistic Particle Physics*, Springer-Verlag 1979.
- [30]: J.J. Sakurai, *Advanced Quantum Mechanics*, Addison Wesley 1967.
- [31]: M.D. Scadron, *Advanced Quantum Theory*, Springer-Verlag 1979.

MEASUREMENT OF PION-ABSORPTION ON ^3He

- [32]: O.A. Zaimidoroga et al., "Study of pion capture by ^3He :
I. Charge exchange and radiative capture, *Soviet Phys. JETP* **21**(1965)848;
II. Reactions involving nuclear disintegration", *Soviet Phys. JETP* **24**(1967)1111.
- [33]: P.Truöl, H.Baer, J.Bistirlich, K.Crowe, N.de Botton and J.Helland, "Measurement of the Panofsky-ratio in ^3He ", *Phys.Rev.Lett.* **32**(1974)1268
- [34]: R.Abela, G.Backenstoss, A.Brandao d'Oliveira, M.Izycki, H.O.Meyer, I.Schwanner, L.Tauscher, P.Bluem, W.Fetscher, D.Gotta, H.Koch, H.Poth and L.M.Simons, "Pionic x-ray transitions in ^3He ", *Phys.Lett.* **68B**(1977)429.
- [35]: J.Källne, H.A.Thiessen, C.L.Morris, S.L.Verbeck, G.R.Burleson, M.J.Devereaux, J.S.McCarthy, J.E.Bolger, C.F.Moore, C.A.Goulding, "Reactions $^3\text{He}(\pi^-,n)^2\text{H}$ and $^4\text{He}(\pi^-,n)^3\text{H}$ at pion energies of 100, 200 and 290MeV", *Phys.Rev.Lett.* **40**(1978)378.
- [36]: G.R.Mason, G.A.Beer, M.S.Dixit, S.K.Kim, J.A.McDonald, A.Olin, R.M.Pearce, W.C.Sperry and J.S.Vincent, "Pionic K x-rays in liquid ^3He ", *Nucl.Phys.* **A340**(1980)240.
- [37]: J.Källne, J.Davis, R.C.Minehart, R.R.Whitney, R.L.Boudrie, J.McClelland and A.W.Stetz, "Two-nucleon pion absorption in $^3,^4\text{He}$ ", *Phys.Lett.* **97B**(1980)205.
- [38]: L.Orphanos, J.Källne, R.Altamus, P.C.Gugelot, J.S.McCarthy, R.C.Minehart, P.A.M.Gram, B.Hoistad, C.L.Morris, E.A.Wadlinger and C.Perdrisat, "Pion absorption in $^3,^4\text{He}$ and πN resonances", *Phys.Rev.Lett.* **46**(1981)1562.
- [39]: J.Källne, J.E.Bolger, M.J.Devereaux and S.L.Verbeck, " $^3\text{He}(\pi^-,n)^2\text{H}$ and $^4\text{He}(\pi^-,n)^3\text{H}$ at 50-295MeV", *Phys.Rev.* **C24**(1981)1102.
- [40]: D.Ashery, R.J.Holt, H.E.Jackson, J.P.Schiffer, J.R.Specht, K.E.Stephenson, R.D.McKeown, J.Ungar, R.E.Segel and P.Zupranski, "Isospin dependence of pion absorption on a pair of nucleons", *Phys.Rev.Lett.* **47**(1981)895.
- [41]: J.Källne, J.Davis, R.C.Minehart, R.R.Whitney, R.L.Boudrie, J.B.McClelland and A.W.Stetz, "The (π^\pm, p) reaction and nuclear pp and pn correlations", *J.Phys.* **G7**(1981)L287.
- [42]: C.M.Hoffman, N.S.P.King, J.Piffaretti, J.Alster, A.Doron, S.Gilad, M.A.Moinester, P.R.Bevington and E.Winklemann, " $^3\text{He}(\pi^-, \pi^0)$ reaction at $T_\pi=200\text{MeV}$ ", *Phys.Rev.* **C25**(1982)438.
- [43]: J.Källne, R.Altamus, P.C.Gugelot, J.S.McCarthy, R.C.Minehart, L.Orphanos, P.A.M.Gram, B.Hoistad, C.L.Morris, E.A.Wadlinger and C.F.Perdrisat, "Pion single charge exchange scattering from ^3He at 285, 428, and 525MeV", *Phys.Rev.* **C25**(1982)1098
- [44]: D.Gotta, M.Dörr, W.Fetscher, G.Schmidt, H.Ullrich, G.Backenstoss, W.Kowald, I.Schwanner and H.-J.Weyer, "Kinematically complete measurement of the absorption of stopped pions in ^3He ", *Phys.Lett.* **112B**(1982)129.
- [45]: G.Backenstoss, W.Kowald, I.Schwanner, H.-J.Weyer, M.Dörr, D.Gotta, G.Schmidt, L.M.Simons and H.Ullrich, "Measurement of the total and partial K-x-ray yields for the pnn- and dn- reaction channels of the π^- -absorption in ^3He ", *Phys.Lett.* **115B**(1982)445.

- [46]: L.Orphanos, J.S.McCarthy, R.C.Minehart, P.A.M.Gram, B.Hoistad, C.F.Perdrisat and J.Källne, " ${}^{3,4}\text{He}(\pi^-,n){}^2,{}^3\text{H}$ and ${}^3\text{He}(\pi^-,\pi^0){}^3\text{H}$ at 285-575MeV", *Phys.Rev.* **C26**(1982)2111.
- [47]: J.Källne, R.C.Minehart, R.R.Whitney, R.L.Boudrie, J.B.McClelland and A.W.Stetz, "Pion scattering and absorption contributions to proton emission from pion-nucleus collisions at $T_\pi=50\text{-}295\text{MeV}$ ", *Phys.Rev.* **C28**(1983)304
- [48]: A.V.Bannikov, B.Le'vay, V.I.Petrukhin, V.A.Vasilyev, L.M.Kochenda, A.A.Markov, V.I.Medvedev, G.L.Sokolov, I.I.Strakovsky and D.Horva'th, "Studies on the atomic capture of stopped negative pions in binary mixtures of ${}^3\text{He}$ with other gases", *Nucl.Phys.* **A403**(1983)515.
- [49]: G.Backenstoss, M.Izycki, M.Steinacher, P.Weber, H.-J.Weyer, K.von Weymarn, S.Cierjacks, S.Ljungfelt, U.Mankin, T.Petkovic', G.Schmidt, H.Ullrich and M.Furic', "Isospin dependence of pion absorption on nucleon pairs in ${}^3\text{He}$ ", *Phys.Lett.* **137B**(1984)329.
- [50]: M.A.Moinester, D.R.Gill, J.Vincent, D.Ashery, S.Levenson, J.Alster, A.Altman, J.Lichtenstadt, E.Piasetzky, K.A.Aniol, R.R.Johnson, H.W.Roser, R.Tacik, W.Gyles, B.Barnett, R.J.Sobie and H.P.Gubler, "Isospin dependence of pion absorption on nucleon pairs at $T_\pi=65\text{MeV}$ ", *Phys.Rev.Lett.* **52**(1984)1203.
- [51]: G.Backenstoss, M.Izycki, W.Kowald, P.Weber, H.-J.Weyer, S.Ljungfelt, U.Mankin, G.Schmidt, H.Ullrich, "Measurement of the ratio $(\pi^-{}^3\text{He}\rightarrow{}^2\text{H})/(\pi^-{}^3\text{He}\rightarrow\text{dn})$ and the partial K-X-ray yields of both reaction channels with stopped pions", To be submitted to *Physics Letters B*.

THEORY: PION-ABSORPTION IN GENERAL

- [52]: M.Brack, D.O.Riska and W.Weise, "Pionic disintegration of the deuteron", *Nucl.Phys.* **A287**(1977)425.
- [53]: G.F.Bertsch and D.O.Riska, "Threshold pion absorption in nuclei", *Phys.Rev.* **C18**(1978)317.
- [54]: C.M.KO and D.O.Riska, "The absorptive p-wave pion-nucleus optical potential", *Nucl.Phys.* **A312**(1978)217.
- [55]: J.Chai and D.O.Riska, "The reactive two-body part of the pion-nucleus optical potential", *Nucl.Phys.* **A329**(1979)429.
- [56]: J.Chai and D.O.Riska, "On the reaction $\bar{p}p\leftrightarrow d\pi^+$ ", *Nucl.Phys.* **A338**(1980)349.
- [57]: O.V.Maxwell, W.Weise and M.Brack, "Meson-baryon dynamics and the $pp\leftrightarrow d\pi^+$ reaction:
- (I). Total and differential cross sections
 - (II). Polarization parameters"
- Nucl.Phys.* **A348**(1980)388 & 429.
- [58]: F.Hachenberg, "Einfluss der Absorption auf die Pion-Kern Wechselwirkung an der Schwelle", PhD Thesis, University of Heidelberg, Fed. Rep. of Germany, 1977; F.Hachenberg and H.J.Pirner, "Off-shell effects in s-wave pion absorption, *Ann. of Phys.* **112**(1978)401.

- [59]: K.Shimizu, A.Faessler and H.Muther, "The pionic disintegration of the deuteron and the absorptive pion-nucleus optical potential", *Nucl.Phys.* **A343**(1980)468.
- [60]: A.M.Green and J.A.Niskanen, "P-wave meson production in $p+p \rightarrow d+\pi^+$ ", *Nucl.Phys.* **A271**(1976)503.
- [61]: J.A.Niskanen, "The differential cross section and polarization in $p+p \rightarrow d+\pi^+$ ", *Nucl.Phys.* **A298**(1978)417.
- [62]: A.M.Green, J.A.Niskanen and M.E.Sainio, "The effect of the $\Delta(1236)$ on the imaginary component of nucleon-nucleon phase-shifts", *J.Phys.* **G4**(1978)1055.
- [63]: W.M.Kloet and R.R.Silbar, "Nucleon-nucleon dynamics at medium energies
(I). Unitary model for elastic and inelastic scattering
(II). Results for NN phase parameters", *Nucl.Phys.* **A338**(1980)281,317.
- [64]: B.Blankleider and I.R.Afnan, "Unified theory of $NN \rightarrow \pi d$, $\pi d \rightarrow \pi d$, and $NN \rightarrow NN$ reactions", *Phys.Rev.* **C24**(1981)1572.
- [65]: A.S.Rinat, Y.Starkand and E.Hammel, "Calculation of $\pi d \rightleftharpoons NN$ observables", *Nucl.Phys.* **A364**(1981)486.
- [66]: Y.Avishai and T.Mizutani, "New approach to the theory of coupled πNN -NN systems:
I. Practical equations and unitarity", *Nucl.Phys.* **A326**(1979)352;
II. Further elaborations and relativistic extensions", *Nucl.Phys.* **A338**(1980)377;
III. A three-body limit", *Nucl.Phys.* **A352**(1981)399;
- [67]: Y.Avishai and T.Mizutani, "Coupled πNN -NN systems in a Hamiltonian approach and in a relativistic off-mass-shell formalism", *Phys.Rev.* **C27**(1983)312.
- [68]: Y.Avishai and T.Mizutani, "Theory of coupled πA -A systems", *Phys.Rev.* **C22**(1980)2492; "Connected Kernel equations for the coupled πNNN -NNN systems", *Nucl.Phys.* **A393**(1983)429
- [69]: M.Betz and F.Coester, "Phenomenological relativistic quantum mechanics of the $NN\pi$ system", *Phys.Rev.* **C21**(1980)2505.
- [70]: M.Betz and T.-S.Lee, "Phenomenological hamiltonian for pions, nucleons, and Δ isobars: applications to the pion-deuteron system", *Phys.Rev.* **C23**(1981)375.
- [71]: T.-S.H.Lee, K.Ohta, M.Thies, "Study of the two-nucleon mechanism of pion absorption in light nuclei", Preliminary draft-January 1984.

THEORY: PION-ABSORPTION IN ${}^3\text{He}$

- [72]: P.P.Divakaran, " π^- capture by ${}^3\text{He}$ and the two-nucleon capture model", *Phys.Rev.* **139**(1965)B387.
- [73]: A.Figureau and M.Ericson, "Absorption of π -mesons by ${}^3\text{He}$ ", *Nucl.Phys.* **B10**(1969)349.
- [74]: A.C.Phillips and F.Roig, "The absorption of pions in ${}^3\text{He}$ ", *Nucl.Phys.* **B60**(1973)93.
- [75]: B.K.Jain, "Pion absorption in ${}^3\text{He}$ ", *Nucl.Phys.* **A296**(1977)479.
- [76]: B.Goulard, A.Laverne and J.D.Vergados, "Panofsky ratio, threshold pion photoproduction, and axial-vector form factor in the $A=3$ system", *Phys.Rev.* **C18**(1978)944.
- [77]: W.R.Gibbs, B.F.Gibson and G.J.Stephenson, Jr., "Threshold pion photoproduction and radiative pion capture. III. ${}^3\text{He} \leftrightarrow {}^3\text{H}$ ", *Phys.Rev.* **C18**(1978)1761.

- [78]: H.Nägeli, "Pion-absorption am ^3He ", PhD Thesis, University of Basel, Switzerland, 1980.
- [79]: T.-S.Lee and K.Ohta, "Isospin dependence of pion absorption on ^3He ", *Phys.Rev.Lett.* **49**(1982)1079.
- [80]: H.Toki and H.Sarafian, "Isospin dependence of pion absorption by nucleon pairs in the He isotopes", *Phys.Lett.* **119B**(1982)285.
- [81]: R.R.Silbar and E.Piasetzky, "Isospin dependence of pion absorption on nucleon pairs", *Phys.Rev.* **C29**(1984)1116.

PARTICLE DETECTORS

- [82]: G.T.Wright, "Scintillation response of organic phosphors", *Phys.Rev.* **91**(1953)1282.
- [83]: T.J.Gooding and H.G.Pugh, "The response of plastic scintillators to high-energy particles", *Nucl.Instr.Meth.* **7**(1960) 189.
- [84]: R.J.Kurz, "A 709/7090 Fortran II program to compute the neutron detection efficiency of plastic scintillator for neutron energies from 1 to 300MeV", Preprint UCRL-11339 (Lawrence Radiation Laboratory, March 1964).
- [85]: N.R.Stanton, "A Monte Carlo program for calculating neutron detection efficiencies in plastic scintillator", Preprint COO-1545-92 (Ohio State University, Feb. 1971); R.M.Edelstein, J.S.Russ, R.C.Thatcher, M.Elfield, E.L.Miller, N.W.Reay, M.A.Abolins, M.T.Lin, K.W.Edwards and D.R.Gill, "Calibration of the neutron detection efficiency of a plastic scintillator, 1 to 200MeV", *Nucl.Instr.Meth.* **100**(1972) 355.
- [86]: M.W.McNaughton, N.S.P.King, F.P.Brady and J.L.Ullmann, "Improved predictions of neutron detection efficiency resulting from new measurements of $^{12}\text{C}(n,p)$ and $^{12}\text{C}(n,d)$ reactions at 56MeV", *Nucl.Instr.Meth.* **129**(1975) 241.
- [87]: A.Del.Guerra, "A compilation of n-p and n-C cross-sections and their use in a Monte Carlo program to calculate the neutron detection efficiency in plastic scintillator in the energy range 1-300MeV", *Nucl.Instr.Meth.* **135**(1976) 337.
- [88]: R.Madey, F.M.Waterman, A.R.Baldwin, J.N.Knudson, J.D.Carson and J.Rapaport, "The response of NE-228A, NE-228, NE-224, and NE-102 scintillators", *Nucl.Instr.Meth.* **151**(1978) 445.
- [89]: R.A.Cecil, B.D.Anderson and R.Madey, "Improved predictions of neutron detection efficiency for hydrocarbon scintillators from 1MeV to about 300MeV", *Nucl.Instr.Meth.* **161**(1979) 439.
- [90]: S.Cierjacks, M.T.Swinhoe, L.Buth, S.D.Howe, F.Raupp, H.Schmitt and L.Lehmann, "The absolute detection efficiency of an NE 213 liquid scintillator for neutrons in the energy range 50-450MeV", *Nucl.Instr.Meth.* **192**(1982) 407.
- [91]: S.Cierjacks et al., to be published.

MISCELLANEOUS TOPICS

- [92]: Particle data group, "Review of particle properties", April 1980 edition, CERN, Geneva.
- [93]: D.F.Measday, M.R.Menard, J.E.Spuller, "Triumf Kinematics Handbook", 1974, University of British Columbia, Vancouver, CANADA.
- [94]: B.J.Verwest and R.A.Arndt, "NN single pion production cross sections below 1500MeV", *Phys.Rev.* **C25**(1982)1979.
- [95]: B.J.Dropesky, G.W.Butler, C.J.Orth, R.A.Williams, M.A.Yates-Williams, G.Friedlander and S.B.Kaufman, "Absolute cross sections for the $^{12}\text{C}(\pi^{\pm},\pi\text{N})^{11}\text{C}$ reactions between 40 and 600MeV, *Phys.Rev.* **C20**(1979)1844.
- [96]: E.C.Kerr, "Orthobaric densities of ^3He 1.3K to 3.2K", *Phys.Rev.* **96**(1954)511.
- [97]: Ch.Hajduk, A.M.Green and M.E.Sainio, "A convenient analytical form for the Triton wave function", *Nucl.Phys.* **A337**(1980)13.
- [98]: H.-J.Weyer, Program "OMT", 1983, Unpublished.
- [99]: H.-J.Weyer, PRECOM description, 1983, Unpublished.
- [100]: C.Williams, J.P.Boujot, CEA-(R)-3042 Saclay 1962.
- [101]: H.-J.Weyer, PhD Thesis, University of Bonn 1977, IR-77-5.
- [102]: O.C.Alkhofer, *Fortschritte der Physik* **15**(1967) 113.
- [103]: T.Petkovic', Private communication.
- [104]: D.Ashery, Private communication.
- [105]: T.-S.H.Lee, Private communication.
- [106]: M.Izycki, Private communication.